The Dissertation Committee for Aaron Jon Kerkhoff
certifies that this is the approved version of the following dissertation:

Multi-Objective Optimization of Antennas for Ultra-Wideband Applications

Committee:

Hao Ling, Supervisor

Ross Baldick

John Davis

Mircea Driga

Dean Neikirk

Robert Rogers

Multi-Objective Optimization of Antennas for Ultra-Wideband Applications

by

Aaron Jon Kerkhoff, B.S.E.E., B.S.Co.E., M.S.E.E.

Dissertation

Presented to the Faculty of the Graduate School of

The University of Texas at Austin

in Partial Fulfillment

of the Requirements

for the Degree of

Doctor of Philosophy

The University of Texas at Austin

May 2008

To my wife Shireen.

Acknowledgments

There are many people who deserve recognition for their contribution to this dissertation. I am especially indebted to my advisor, Professor Hao Ling, whose deep insight, enthusiasm, and patient encouragement have inspired me throughout my graduate studies. I would also like to thank Professor Ross Baldick, Professor John Davis, Professor Mircea Driga, Professor Dean Neikirk, and Dr. Robert Rogers for taking the time to be on my committee, and for their helpful suggestions. I am grateful to Clark Hughes, Dr. Tom Gaussiran, Dr. David Munton, and Brent Renfro of the Applied Research Laboratories, University of Texas at Austin for their support of my Ph.D. work throughout my employment there. I also appreciate the many interesting and helpful discussions concerning radio astronomy that I have had with my colleague Johnathan York, also of the Applied Research Laboratories. Most of all, I want to thank my wife Shireen, parents Jon and Judith, brother Andrew, uncle Jim, and other family and friends for all of the love and support they have given me over the years.

Aaron Jon Kerkhoff

The University of Texas at Austin

May 2008

Multi-Objective Optimization of Antennas for Ultra-Wideband Applications

Publication No. ____________

Aaron Jon Kerkhoff, Ph.D.
The University of Texas at Austin, 2008

Supervisor: Hao Ling

There are a growing number of ultra-wideband applications, which involve the radiation or reception of electromagnetic signals over frequency bandwidths ranging from 1.3:1 to over 10:1. In the design of antennas for ultra-wideband systems, many design objectives must be considered, including impedance matching, radiation efficiency, radiation pattern stability, size, and possibly impulse response. Given the very wide bandwidths considered, it can be challenging to meet all objectives simultaneously, and optimization techniques are useful to achieve a reasonable compromise between objectives. In this dissertation, multi-objective Genetic Algorithm (GA) optimization is used to design ultra-wideband antennas for use in wireless communications and low frequency radio astronomy.

GA optimization is first applied to the design of ultra-wide bandwidth planar monopole antennas, which exhibit a narrow-band frequency notch in order to mitigate interference with co-located radio systems. The GA optimizer uses a weighted sum cost function related to impedance matching and radiation patterns at frequencies within both the wide operating band and the narrow notch band to improve antenna performance. A two-dimensional matrix chromosome is used in the GA to represent a wide-range on planar element shapes. It is shown that the GA generates antenna designs which exhibit wideband performance equal to traditional band-notched designs, but have improved azimuth plane radiation pattern symmetry, which widens the effective notch bandwidth.

Pareto GA optimization is then applied to the design of planar dipole antenna elements operating over a ground plane for use in a low frequency radio telescope array. The objectives considered include Galactic background or "sky" noise reception level, and radiation patterns over the operating band of 20 to 80 MHz. It is demonstrated that the Pareto GA approach generates a set of designs, which exhibit a wide range of trade-offs between the two design objectives, and satisfy all applied geometrical constraints. Multiple GA executions are performed to determine how antenna performance trade-offs are affected by different geometrical constraint values, feed impedance values, radiating element shapes and orientations, and ground conditions.

In a follow-up to the previous study, the effects of mutual coupling in a low frequency radio telescope array are considered. It is first shown that a simple receive-based definition of coupling between two antennas can be used to design antenna elements which exhibit reduced mutual coupling effects when operated in a large phased array. This result is utilized in order to perform Pareto GA optimization of wire frame bow-tie dipole elements in terms of mutual coupling, as well as sky noise response and radiation patterns over the 20 to 80 MHz band. The GA generates a set of designs that span a wide range of objective values. The results are analyzed to understand the trade-offs that may be made between the three objectives.

Contents

List of Figures

List of Tables

Chapter 1

Introduction

There are a growing number of applications, which involve the radiation or reception of electromagnetic signals over ultra-wide frequency bandwidths. The term ultra-wideband refers to a fractional bandwidth of at least 25%, but generally implies much wider bandwidths of one or more octaves; bandwidths in excess of a decade are also possible. One of the earliest uses of ultra-wideband signals was in ground penetrating radar (GPR) for the detection of buried objects such as mines [1]. Since then, other forms of ultra-wideband radar have been developed such as synthetic aperture radar (SAR) for airborne detection of vehicles through foliage [2]. Other traditional ultra-wideband applications include electronic support measures (ESM) such as signal monitoring and direction finding, and electromagnetic compatibility (EMC) testing.

An emerging use of ultra-wideband signalling is in high-speed wireless communications where it is commonly referred to as UWB radio. The FCC has approved the unlicensed use of frequencies between 3.1 GHz and 10.6 GHz for this purpose [3]. Additionally, the Wireless-USB standard has been created to support the development of low-power wireless personal area network (PAN) devices, which provide short-range data transfer rates of up to 480 Mbps [4]. These devices are planned for integration into commercial products such as televisions, DVD players, and laptop computers for uses such as real-time streaming video transfer. The ultra wide bandwidth enables extremely high data rates, supports a high number of co-located devices, and provides resistance against multipath fading.

Another relatively new application which involves operation over ultra wide bandwidths is low frequency radio astronomy. The Long Wavelength Array (LWA) [5] and LOFAR [6] are large synthesis imaging radio telescopes currently under development to perform studies in the areas of astrophysics, solar and space weather science, and ionospheric science in the frequency range below 100 MHz. It is desired that these telescopes operate over multiple octaves of bandwidth in order to provide the flexibility to observe phenomena which occur, and make coordinated measurements with other telescopes which operate at many different frequencies. For instance, radio emissions from Jupiter are only evident below 40 MHz, while the lowest operating band of the Very Large Array (VLA), an instrument which will be used in conjunction with the LWA, is 74 MHz. The ultra-wide bandwidth also aids in the study of broadband phenomena such as the galactic radio continuum and transient phenomena such as solar bursts and cosmic-ray air showers [7].

An important part of any system involving electromagnetic radiation is the antenna. In an ultra-wideband system, the antenna must typically exhibit good impedance matching, high radiation efficiency, and stable radiation patterns over the entire operating band. In some applications, the antenna may also need to radiate or receive impulsive signals with high fidelity, in which case the antenna transfer function must be considered. In most cases, the antenna design will also be subject to both size and geometry constraints.

A number of antenna topologies have been considered for the purpose of operating over wide instantaneous bandwidths. TEM horns and reflector antennas such as the Impulse Radiating Antenna (IRA) [8] have found popular use in impulse radar applications as they have good power handling capabilities, high directivity, and can be designed to radiate pulses with good fidelity [1]. Frequency independent antennas such as log periodic antennas and spiral antennas offer good impedance matching and stable radiating patterns over extremely wide bandwidths of up to 20:1. Log periodic antennas such as log periodic dipole arrays (LPDA) have been used in EMC and antenna testing and as ultra-wideband feeds for reflector antennas [9]. Owing to their planar nature, which facilitates their integration with circuitry, spiral antennas have been used in many applications including direction of arrival (DOA) arrays [10], and multi-function communication and radar arrays [11].

Many forms of monopole and dipole antennas are also used for ultra-wideband applications. The bicone antenna is one of the best known ultra-wideband dipole designs and is typically used in EMC and antenna testing. There has been increasing interest in recent years in planar monopoles and dipoles for use in UWB radio [12]. Planar monopoles and dipoles offer extremely wide matching bandwidths (greater than 10:1 possible), reasonable pattern bandwidths (at least 3:1), are relatively electrically small (as compared with spiral antennas, for instance) and can be easily integrated into handheld wireless electronics. Bow-tie dipoles, which are planar versions of the bicone, and planar dipoles have been used in GPR applications [13]. Variations of bow-tie and planar dipoles have also been used as elements in low frequency radio telescope arrays, in which they are operated over bandwidths of up to 4:1 [14],[15].

In the design of ultra-wideband antennas, it can be challenging to simultaneously achieve all design objectives and satisfy all constraints given the wide range of frequencies considered. Genetic Algorithm (GA) optimization, which is a stochastic search technique based on the principles of natural selection and evolution, has become popular in engineering design [16]. As opposed to traditional, gradient-based optimization techniques, which converge to local optima, GA's are capable of finding near-global optima in a relatively efficient manner. GA's can be formulated easily to handle many design parameters and design objectives, which makes them useful for complex, multi-dimensional optimization problems. GA optimization has been applied to many antenna-related design problems including wire monopole and dipole antennas [17], micro-strip patch antennas [18], Yagi-Uda antennas [19], and antenna arrays [20].

There are two basic approaches to implementing multi-objective optimization in a GA. The first approach, here called scalar multi-objective GA, involves the use of a scalar cost function, which is a weighted sum of cost functions corresponding to different objectives. A traditional GA consisting of selection, cross-over, mutation, and cost function evaluation steps operates on the weighted sum cost function as it would a cost function related to only a single objective. The relative weights of the different cost function components must be selected manually by the user. In the scalar multi-objective GA approach, the entire GA population tends to converge to a single design, which best satisfies the cost function according to the weights chosen. This approach was used in [21], for example, to optimize crooked-wire monopole antennas for vehicular applications in terms of gain and impedance matching.

In a second approach to multi-objective optimization, called Pareto GA, all objectives are handled independently and explicitly rather than being combined into a single cost function. A popular implementation called non-dominated sorting GA (NSGA) [22] is similar to the traditional GA, but includes an additional ranking step after the cost function evaluation. The rank assigned to each individual in the population indicates the degree to which it is dominated by other individuals in terms of all objectives, where rank-1 indicates that a design is non-dominated. The group of rank-1 individuals form a so-called Pareto front, which indicates the optimal trade-off that can be made between different objectives for a range of objective values. In this way, a set of optimal designs exhibiting a range of performance trade-offs can be generated with a single GA execution. Pareto GA has been used, for example, to optimize phased arrays in terms of beamwidth and sidelobe level [23] and electrically small wire antennas in terms bandwidth, efficiency, and size [24].

Which of these two approaches to use largely depends on the problem at hand. If one particular trade-off between objectives is sought, and especially if the relationship between different objectives is understood, then a scalar multi-objective GA may be preferable. This type of GA has the advantage of being simple in design, making it easier to use. It also works well with relatively small optimization populations (a few tens of individuals are sufficient for many problems), so that the GA can execute quickly. On the other hand, if it is desired to consider multiple trade-offs between objectives and/or the relationship between objectives is not well understood, a Pareto GA may be preferable. This type of GA has the advantage that an entire set of Pareto optimal designs representing a range of different trade-offs between objectives can be generated from a single optimization. The design of a Pareto GA, however, is more complex than a scalar multi-objective GA, particularly when the implementation of certain refinements such as an elitism operator or constraint handling are considered. Additionally, very large optimization populations (typically hundreds or a few thousand individuals) are required to achieve good results with a Pareto GA, which leads to long run times.

While GA optimization has been applied to many antenna design problems, there have been few reported studies involving ultra-wideband antennas, and fewer yet involving multi-objective optimization of such antennas. The objective of this dissertation is to investigate the application of multi-objective GA optimization techniques to the design of ultra-wideband antennas. This investigation will be focused on applications related to wireless communications and low frequency radio astronomy.

In Chapter 2, multi-objective GA optimization is used to the design of planar monopole antennas, which exhibit both ultra-wideband operation and a narrow-band frequency notch. Such an antenna is useful in applications involving wideband communications where it is desired to mitigate interference with other radio systems co-located with the operating band. This could occur, for instance, between UWB radio devices, which may operate between 3.1 to 10.6 GHz and wireless local area network (WLAN) devices operating near 5.0 GHz. While previously reported band-notched planar monopole designs exhibit a narrow band notch at the desired frequency, the effective bandwidth provided by the notch is limited due to azimuth plane asymmetry in the radiation patterns. A scalar multi-objective GA optimizer with a weighted sum cost function related to impedance matching and radiation patterns is used to widen the bandwidth of the notch, and thus improve the filtering performance of the antenna, while maintaining good ultra-wideband performance.

In Chapter 3, Pareto GA optimization is applied to the design of planar dipole antenna elements for use in low frequency radio astronomy. Low frequency radio telescopes currently under development, such as the LWA or LOFAR, will consist of thousands of dipole elements operated in a number of large phased arrays. It is important that these antenna elements receive the Galactic background or ”sky” noise at a high level in order to optimize system sensitivity. The antenna elements should also exhibit wide beamwidth and smoothly varying radiation patterns to permit full-sky view and simplify system calibration. Given that the operating bands of these systems are so wide (20 to 80 MHz for LWA, for instance), it is difficult to meet these objectives over all frequencies. Therefore, a Pareto GA is used to determine the range of performance trade-offs that can be made in terms of the sky noise and radiation pattern objectives with planar dipole antennas. Multiple GA executions are performed to determine how antenna performance trade-offs are affected by different geometrical constraint values, feed impedance values, radiating element shapes and orientations, and ground conditions beneath the antennas.

As a follow-up to the previous chapter, Chapter 4 considers the effects of mutual coupling in a low frequency radio telescope array. Mutual coupling interactions between antenna elements in a phased array can lead to distortions in the beamformed response of the array, and therefore, it is desired to reduce these effects. While mutual coupling effects can be fully characterized by full-wave simulation of the entire array, this is very computationally intensive for large arrays. Therefore, a receive-based coupling calculation between two antennas is considered as a simplified means of designing antenna elements with reduced coupling. This approach is used to enable Pareto GA optimization of wire-frame bow-tie dipole elements in terms of mutual coupling, as well as sky noise, and radiation pattern objectives. The results from the GA are analyzed to understand the trade-offs that may be made between the three objectives. The performances of GA-generated antenna designs when operated in a large phased array are characterized through simulation.

In Chapter 5, conclusions are given and directions for future research are discussed.

Chapter 2

Design of a Band-Notched Planar Monopole Antenna Using Genetic Algorithm Optimization

2.1 Introduction

The development of wireless technologies such as ultra-wideband (UWB) radio, have increased the demand for wideband antennas. Planar monopole antennas have received much attention due to their wideband matching characteristic, omnidirectional radiation patterns, high radiation efficiency, and compact size [25]-[27]. When operating over wide bandwidths, it is possible to overlap with the operating band of other wireless systems. Therefore, it may be necessary to implement a notch filter in the wideband system to prevent interference with other systems. It is demonstrated in [28] that by etching a specific feature in a planar monopole, a narrow and deep notch band can be achieved within a wide operating band. Subsequent studies have shown that a wide range of etched features can be used to achieve this effect, and that the feature dimensions can be used to control the frequency and bandwidth of the notch [29]-[32]. It is also demonstrated that multiple notch bands can be achieved in a single planar monopole by etching multiple features in the antenna [33]. As mentioned in [29] and [33], however, traditional band-notched planar monopoles exhibit asymmetric radiation patterns in the horizontal plane within the notch band. This causes the attenuation provided by the notch to vary as a function of the azimuth angle, which as will be demonstrated in this chapter, lowers the effective bandwidth over which a given level of attenuation can be achieved. It is desirable to improve the pattern symmetry of band-notched planar monopoles in order to maximize attenuation bandwidth.

While a number of studies have been performed in which genetic algorithm (GA) optimization is used to generate broadband wire based monopole antennas [34]-[36], few have been reported involving GA and planar monopole antennas. In [37], GA is used to study the trade-off between impedance matching bandwidth and electrical size for planar monopoles. GA is used in [38] to design a planar monopole suitable for use in UWB communication systems. In both studies, GA is used to optimize the impedance matching of the antenna over a wide continuous bandwidth. In the present study, a GA is presented which optimizes impedance matching and radiation patterns over both an ultra-wide operating band and a narrow notch band within the operating band. As will be shown, this GA is capable of generating planar monopoles with improved band-notch characteristics compared with traditional band-notched planar monopoles.

This chapter is organized as follows: It is first demonstrated that traditional band-notched planar monopoles may suffer from radiation pattern asymmetry, which limits the useful attenuation bandwidth they provide. The design of a GA for use in optimizing band-notched planar monopoles and results generated by the GA are then presented. Results are then summarized.

2.2 Traditional Band-Notched Planar Monopole Antenna Design

A typical band-notched planar monopole antenna consisting of a square-shaped radiating element with an upside-down 'U' feature etched within the element is pictured in Figure 2.1. This relatively simple structure is selected for study to provide straightforward design and analysis. The dimension of the square is chosen as H = 7.1 cm to accommodate the measurement equipment and antenna manufacturing method available for this study. The feed height, h_f = 0.35 cm, provides the widest possible VSWR $\leq$ 2 matching band, 0.84 GHz to 1.76 GHz, assuming a 50 Ω feed. The notch frequency, given the dimensions of the band-notch feature, can be predicted by [30]

$$f_{notch} = \frac{c}{4(l_1 + l_2 - t)} \tag{2.1}$$

where c is the speed of light. The dimensions h_1 = 1.1 cm, t = 0.2 cm, l_1 = 4.1 cm, and l_2 = 1.6 cm, are chosen to place the notch band near the center of the matching band at 1.36 GHz. Versions of the square monopole both with and without the band-notch feature are simulated and measured. Simulations are performed with WIPL-D [39] assuming a lossless infinite ground plane. The antennas are constructed out of thin copper foil and measured over a 0.9 m square copper ground plane. The simulated and measured VSWR of the two designs are compared in Figure 2.2. It is evident that by adding the upside-down 'U' band-notch feature in the element, a narrow notch band has been achieved while maintaining the desired wideband performance. Good agreement is achieved between measurement and simulation.

The radiation patterns for the notched and un-notched square planar monopoles are compared in Figure 2.3. At frequencies above and below the notch frequency,

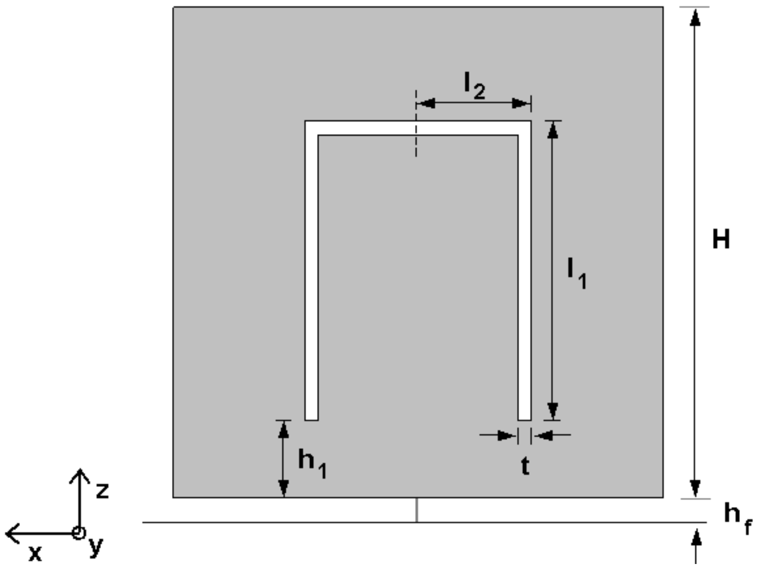

Figure 2.1: Geometry of the square planar monopole antenna with the traditional band-notch feature.

the patterns are essentially unchanged by the band-notch feature. However, the patterns are changed significantly at frequencies within the notch band, as seen in Figure 2.3b. In particular, the band-notched antenna exhibits highly directional radiation patterns in the horizontal plane (rightmost column of Figure 2.3), unlike the nearly omni-directional patterns of the un-notched antenna. In comparing Figure 2.3b to Figure 2.3c, it is also apparent that the azimuth angle of peak gain changes as the frequency is varied within the notch band. This effect can be seen more clearly in Figure 2.4, which compares the gain of the notched and un-notched antennas in the principal planes at the horizon as a function of frequency. It is clear from this figure that the gain of the antenna varies significantly within the notch band, and that the variation is asymmetric between the two principal planes.

To quantify the quality of the band-notched antenna, the attenuation pro-

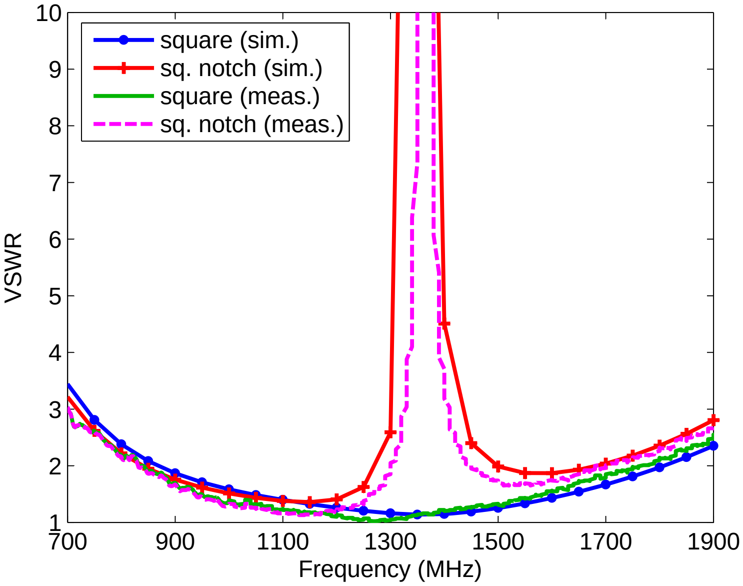

Figure 2.2: Comparison of simulated (sim.) and measured (meas.) impedance matching for square planar monopoles with (sq. notch) and without (square) the band-notch feature.

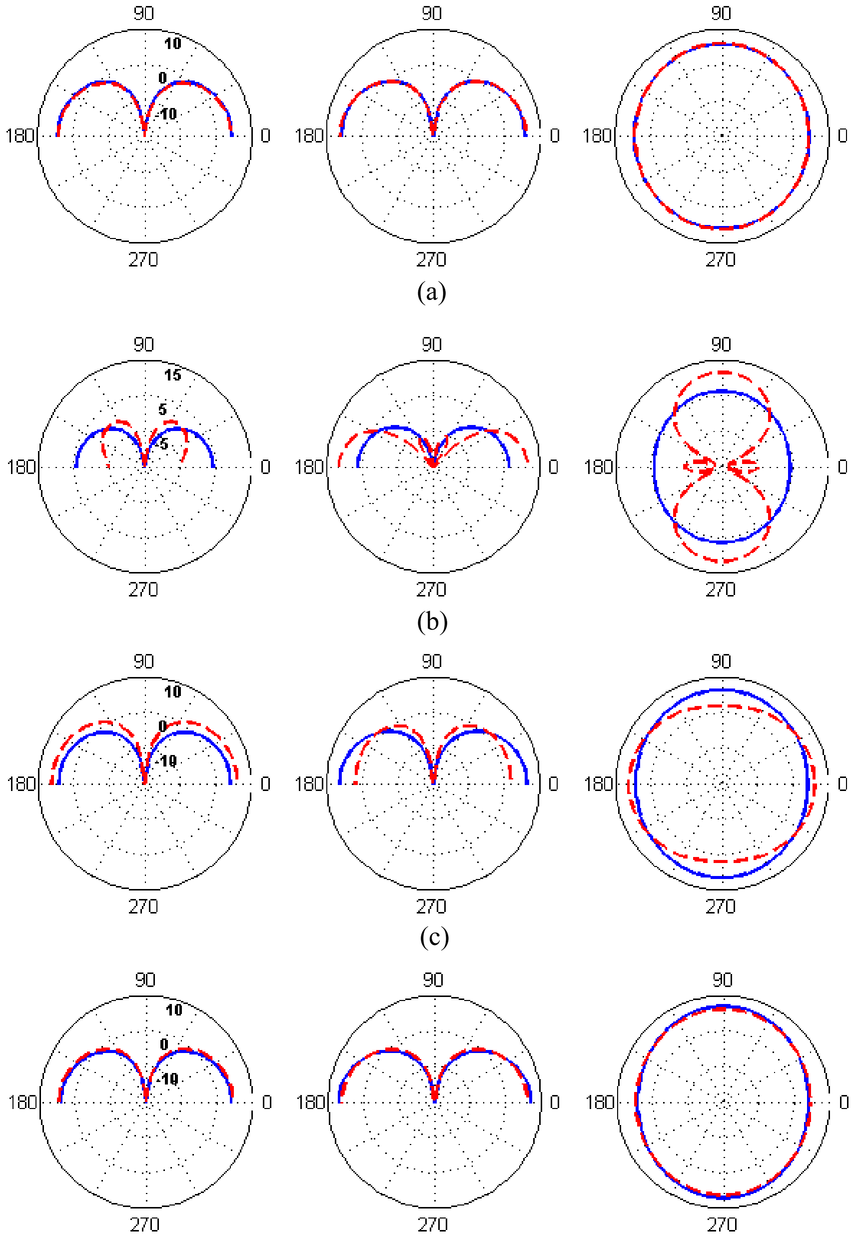

(a)

(b)

(c)

(d)

Figure 2.3: Simulated radiation patterns for the un-notched square planar monopole (solid), and the notched square planar monopole (dashed.) From left to right, x-z plane ($\phi = 0^\circ$), y-z plane ($\phi = 90^\circ$), x-y plane ($\theta = 90^\circ$). (a) 1100 MHz, (b) 1350 MHz, (c) 1400 MHz, (d) 1600 MHz.

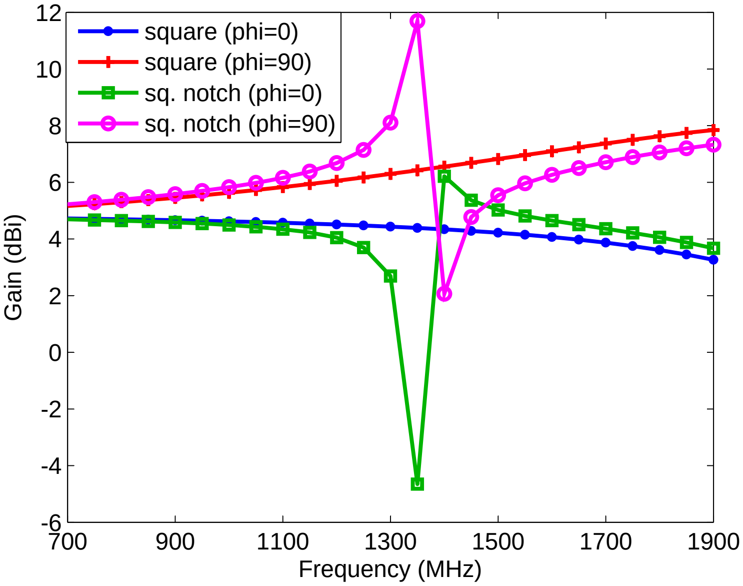

Figure 2.4: Simulated gain of the notched (sq. notch) and un-notched square planar monopoles (square) in the two principal planes ($\phi = 0^\circ$ and $\phi = 90^\circ$) at the horizon ($\theta = 90^\circ$).

vided by the antenna relative to the original, un-notched antenna is calculated. For simulated data, relative attenuation in dB is calculated using

$$\alpha_{sim} = (ML_n - ML_u) + (G_u - G_n) \tag{2.2}$$

where ML indicates mismatch loss as defined by

$$ML = -10\log_{10}(1 - |\rho|^2), \tag{2.3}$$

ρ is the reflection coefficient of the antenna, and G is the gain of the antenna in dBi. The subscripts 'n' and 'u' in Equation 2.2 refer to notched and un-notched antennas respectively. To measure attenuation, the antenna is installed over a 0.9 m by 0.9 m ground plane and placed 1.2 m away from a wideband double-ridged waveguide horn; both antennas are connected to a vector network analyzer. The test setup is shown in Figure 2.5. S_{21} measurements are taken of both the un-notched and notched square planar monopoles using this setup, yielding $S_{21,u}$ and $S_{21,n}$ in dB, respectively . The measured relative attenuation, in dB, is given by

$$\alpha_{meas} = S_{21,u} - S_{21,n}. \tag{2.4}$$

Measured and simulated relative attenuation for the band-notched planar monopole in the principal planes at the horizon are compared in Figure 2.6. Good agreement is achieved between the two results. Though the band-notch feature provides high peak attenuation in each of the principal planes, the frequency where peak attenuation occurs varies with azimuth angle. As shown earlier, this effect is due to the asymmetric radiation patterns exhibited within the notch band. The fractional bandwidths for attenuation levels of 5 dB, 10 dB, and 15 dB are tabulated in Table 2.1 for each principal plane. Additionally, the effective bandwidth over which each attenuation level is simultaneously achieved over all observation angles in the horizontal plane is calculated. Though the band-notched antenna can provide high attenuation over reasonable bandwidths in one direction at a time, it exhibits attenuation simultaneously over all observation angles over only a very narrow bandwidth.

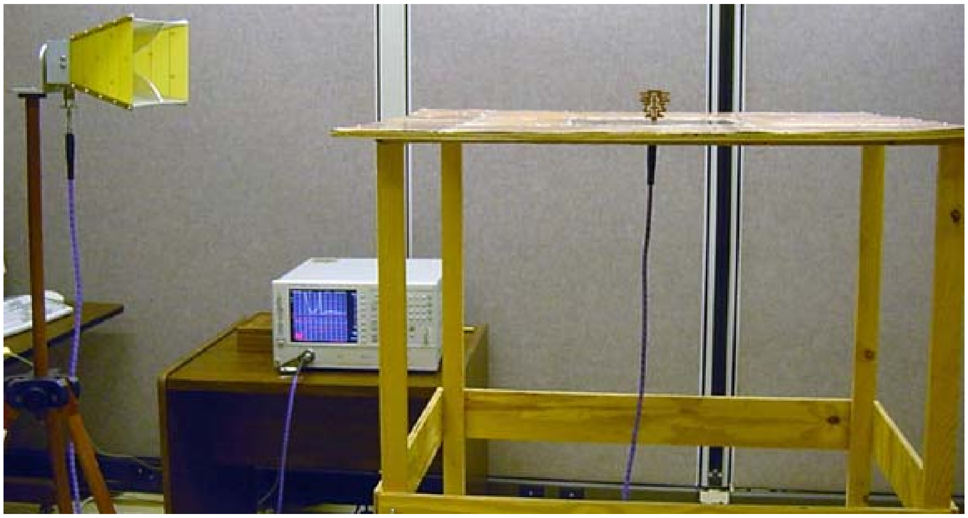

Figure 2.5: Picture of the test setup used in attenuation measurements.

2.3 GA Optimization of Band-Notched Planar Monopoles

A GA optimizer is developed in order to improve the performance of band-notched planar monopoles. The GA operates on a matrix chromosome, which describes the shape of the planar element of the antenna. This chromosome design is described notionally in Figure 2.7. Matrix cells which contain a ‘1’ correspond to portions of the antenna filled with metal; cells which contain a ‘0’ correspond to portions of the antenna that are not filled. There are no constraints placed upon how matrix

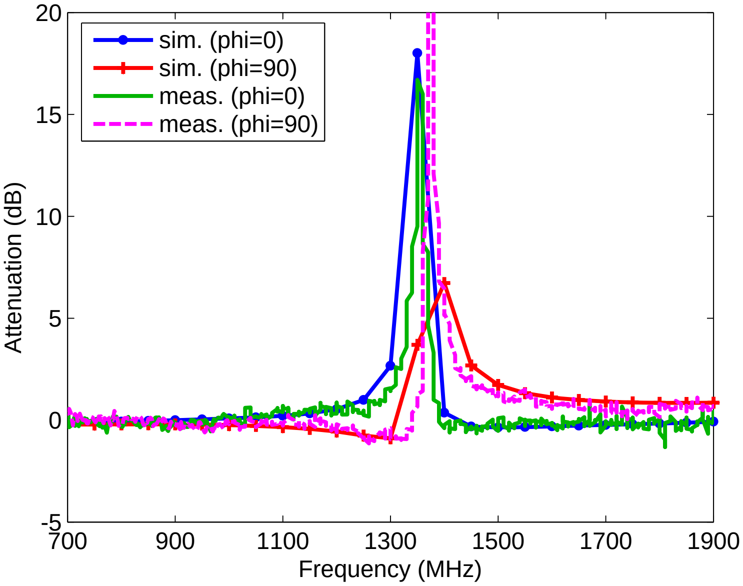

Figure 2.6: Comparison of simulated and measured relative attenuation provided by the band-notched square planar monopole relative to the un-notched square planar monopole in the two principal planes ($\phi = 0^\circ$ and $\phi = 90^\circ$) at the horizon ($\theta = 90^\circ$).

Table 2.1: Measured fractional bandwidths over which different attenuation levels are achieved by the band-notched square planar monopole in each principal plane at the horizon. Also provided is the corresponding bandwidth over which each attenuation level is achieved simultaneously over all azimuth angles.

	Fractional bandwidth (%) in $\phi = 0^\circ$ plane	Fractional bandwidth (%) in $\phi = 90^\circ$ plane	Effective fractional bandwidth (%) over all ϕ
Attenuation $>$ 5 dB	3.11	3.11	0.88
Attenuation $>$ 10 dB	1.03	1.45	0.00
Attenuation $>$ 15 dB	0.30	0.80	0.00

cells can be filled except that symmetry must be maintained along the antenna centerline. As depicted in Figure 2.7, this implies that holes may be placed within the radiating element, and that fragments separate from the main element may be created. A common dimension is assumed for all rows and columns in the matrix.

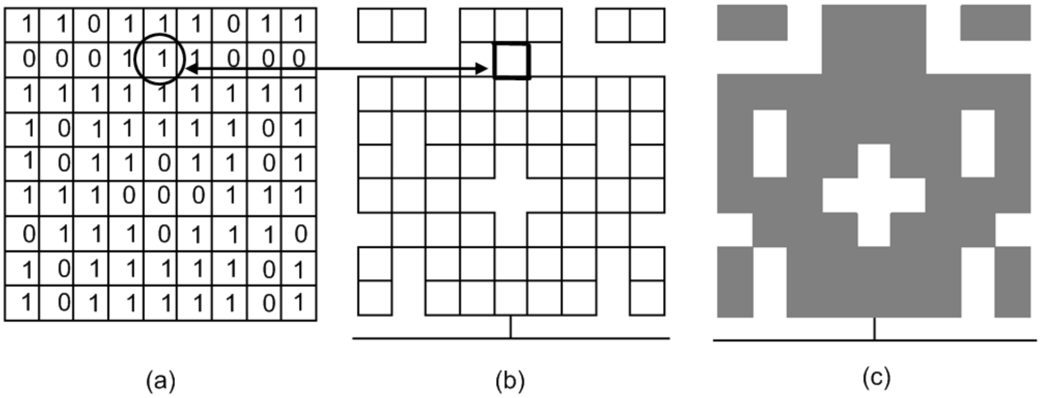

1	1	0	1	1	1	0	1	1
0	0	0	1	1	1	0	0	0
1	1	1	1	1	1	1	1	1
1	0	1	1	1	1	1	0	1
1	0	1	1	0	1	1	0	1
1	1	1	0	0	0	1	1	1
0	1	1	1	0	1	1	1	0
1	0	1	1	1	1	1	0	1
1	0	1	1	1	1	1	0	1

Figure 2.7: (a) A chromosome matrix, (b) the corresponding wire-grid model used in simulation, (c) the corresponding physical design. The arrow indicates the wire elements in the model which correspond to the circled chromosome entry.

The GA begins by applying random mutations to a preliminary antenna design to form an initial population of size N_{pop}. For each chromosome that is to be mutated, the GA first randomly determines how many mutations will be applied to the chromosome, which can vary between 0 and $N_{mut,MAX}$. Each mutation consists of setting all matrix cell values to '1' or '0' along a selected portion of a selected row or column, which is chosen randomly by the GA. The GA also randomly determines the length of each mutation (number of adjacent cells that will be affected), which can vary between 1 and $N_{cells,MAX}$ cells. All mutations must be applied symmetrically about the antenna centerline. Computer simulation is performed on each mutated design and the cost calculated. Binary tournament selection is used to determine the fittest designs in the population. The loser of each binary tournament is discarded corresponding to a replacement rate of 0.5. Single-point cross-over is then applied to each surviving chromosome in order to replenish the population to its original size. Cross-over is performed by randomly picking a matrix row number, and swapping the contents above and below this row between two selected surviving chromosomes in order to generate two new chromosomes. Mutation is applied to the new designs and their costs are calculated. This process is repeated until the GA reduces the cost below some pre-determined threshold or stagnates.

The Numerical Electromagnetics Code (NEC-2) is used to simulate antenna performance in the GA. Despite being a wire-based code, previous studies have indicated that NEC provides good accuracy for planar monopoles [37]. A wire grid corresponding to the entries of the chromosome matrix is used to model the shape of the planar element. The dimensions of the wire grid rows and columns are equal to those of the matrix chromosome. A "filled" chromosome entry corresponds to four individual wires in the model along the perimeter of the chromosome entry as indicated in Figure 2.7. The equal area rule is used to select the wire radius, r_{wire}, for a given grid spacing, d_{mesh} [40]. A lossless infinite ground plane is used in all simulations.

In order to generate improved band-notched planar monopoles, the GA must simultaneously optimize impedance matching and radiation pattern symmetry over both a wide instantaneous operating band and a narrow notch band. Therefore the GA seeks to minimize the following cost function

$$C = w_1 C_1 + w_2 C_2 + w_3 C_3 \tag{2.5}$$

$$C_1 = \begin{cases} \max\limits_{f \in F_m} \{\rho(f) - \rho_{m,goal}\}, & \text{if } \exists\ \rho(\text{f}) > \rho_{m,goal} \\ 0, & \text{otherwise} \end{cases} \tag{2.6}$$

$$C_2 = \begin{cases} \max\limits_{f \in F_u}\{\rho_{u,goal} - \rho(f)\}, & \text{if } \exists\ \rho(\text{f}) < \rho_{u,goal} \\ 0, & \text{otherwise} \end{cases} \quad (2.7)$$

$$C_3 = \begin{cases} \max\limits_{f \in F}\{G_{dev}(f,\theta) - G_{dev,goal}\}, & \text{if } \exists\ G_{dev}(\text{f},\theta) > G_{dev,goal} \\ 0, & \text{otherwise} \end{cases} \quad (2.8)$$

where C_1, C_2, and C_3 are the portions of the cost function corresponding to impedance matching over the operating band, impedance matching over the notch band, and radiation pattern symmetry over all frequencies, respectively; w_1, w_2, and w_3 are used to control the relative weight of each cost function term. Through C_1, the GA minimizes the maximum reflection coefficient, ρ, over the set of frequencies, F_m, that are in the operating band and thus, should be well matched. Through C_2, the GA minimizes the maximum of the negation of reflection coefficients over frequencies in the notch band, F_u. That is, high reflection coefficients are sought in the notch band. In C_3, $G_{dev}(f,\theta)$ is the maximum deviation in gain between any two azimuth angles for a given frequency, f, and elevation angle, θ. Therefore, C_3 is used to minimize the maximum azimuth pattern deviation over all frequencies in both the operating band and notch band, $F = \{F_m, F_u\}$. The constraints $\rho_{m,goal}$, $\rho_{u,goal}$, and $G_{dev,goal}$ are included in the cost function to prevent the GA from optimizing any of the terms C_1, C_2, or C_3 more than is needed.

This GA implementation is used to generate a planar monopole design with similar wideband properties as the reference band-notched antenna presented in Section 2.2, but with improved band-notch characteristics. It is desired to maintain the same VSWR $\leq$ 2 matching band, the same notch frequency, and the same approximate antenna size. The set of operating band frequencies (all in GHz) used in the GA is $F_m = \{0.85, 1.05, 1.25, 1.45, 1.6, 1.75\}$, and the notch band frequency (in GHz) is $F_u = \{1.35\}$ for a total number of frequencies of 7. The overall size of the antenna element is constrained to be 6.9 cm by 6.9 cm. This is discretized into a 23 by 23 matrix chromosome, which implies that the antenna model grid spacing is 0.3 cm. The feed height is fixed at 0.2 cm throughout the optimization. The GA parameters $N_{pop} = 60$, $N_{mut,MAX} = 4$, $N_{cells,MAX} = 4$ were found to give good performance with reasonable convergence time.

It is found that best results can be achieved if the optimization is executed in two separate steps. In the first step, only impedance matching is optimized in order to achieve the desired operating band and notch band matching characteristics. In this step, the cost function weights are $w_1 = 1.0$, $w_2 = 1.0$, and $w_3 = 0.0$ and the cost function constraints are $\rho_{m,goal} = 0.333$ and $\rho_{u,goal} = 0.9$. A rectangular element 3.9 cm wide by 6.9 cm tall is used as the initial condition. The GA reduces the cost function from 0.79 to 0.06 in 351 generations. This optimization takes approximately 26.0 hours to complete with four 1.0 GHz AMD Athlon processors running NEC-2. The best result from this initial optimization is used as the initial condition in a second optimization, in which radiation pattern symmetry is optimized along with impedance matching. In this optimization, the cost function weights are $w_1 = 1.0$, $w_2 = 1.0$, and $w_3 = 0.1$ and the cost function constraints are $\rho_{m,goal} = 0.333$, $\rho_{u,goal} = 0.9$, and $G_{dev,goal} = 0.0$. The antenna gain is calculated at the angles $\theta = 90^\circ$ and $\phi = \{0^\circ, 90^\circ\}$. In this optimization, the GA reduces the cost function from 0.32 to 0.21 in 193 generations, which takes 14.3 hours to run. Therefore a total of 544 generations and a run time of 40.3 hours is required to achieve the final design.

The final band-notched planar monopole antenna design generated by the GA is shown in Figure 2.8a. This design is fabricated out of thin copper foil; a small amount of transparent tape is used to suspend the detached pieces from the main element. Minor changes have been made to the design during fabrication, which are evident in Figure 2.8b, in order to improve the mechanical integrity of the antenna. The antenna is measured over a 0.9 m square copper ground plane. The measured and simulated VSWR for the GA band-notched design and the original square planar monopole are compared in Figure 2.9. Good agreement is achieved between measurement and simulation. As can be seen, the GA design exhibits poor matching at the desired notch frequency while maintaining a good match over the same operating band as the square monopole.

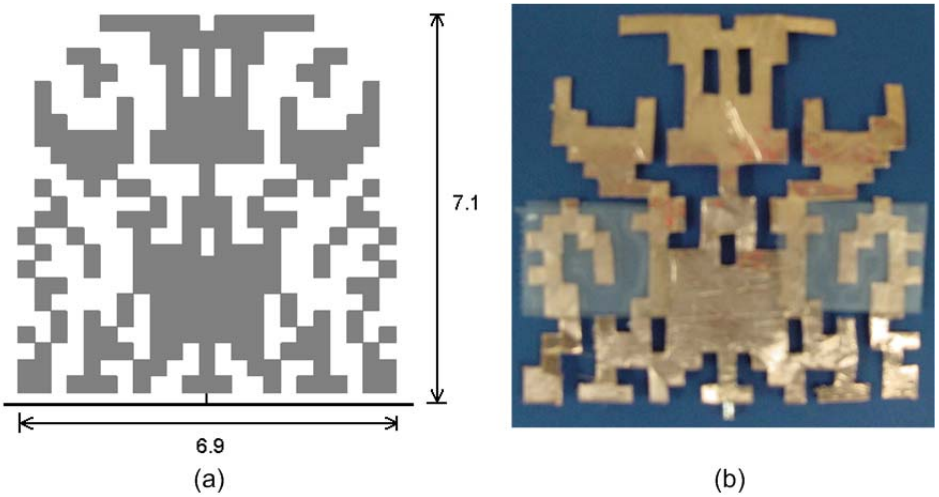

Figure 2.8: (a) The GA-generated band-notched planar monopole antenna design, (b) the fabricated version of the antenna design. Dimensions are given in centimeters.

The radiation patterns for the GA design are presented in Figure 2.10. As with the original band-notched design, the patterns of the GA design are essentially identical to the square planar monopole at frequencies above and below the notch frequency, but are perturbed at frequencies near the notch frequency. However, as seen in Figures 2.10b and 2.10c, the radiation patterns exhibit much better symme-

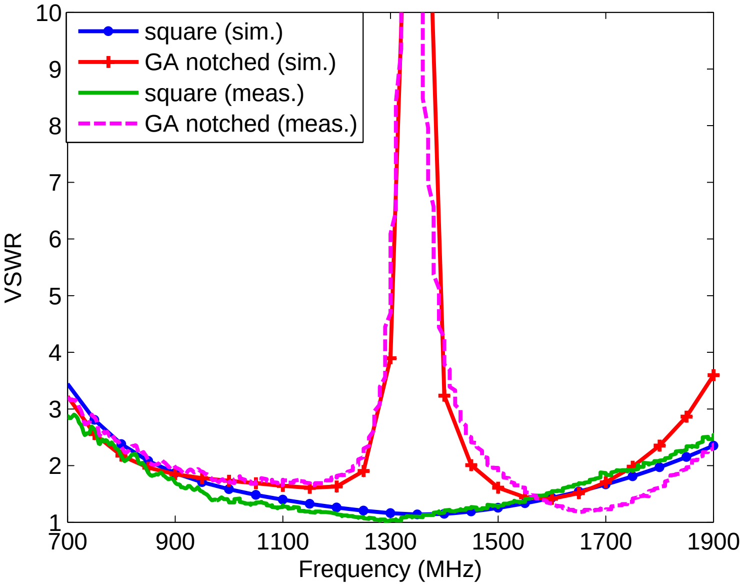

Figure 2.9: Comparison of simulated (sim.) and measured (meas.) impedance matching for the GA-generated band-notched planar monopole (GA notched) and the un-notched square planar monopole (square).

try in the azimuth plane throughout the notch band. The gain of the GA design and square monopole in the principal planes at the horizon are compared in Figure 2.11. As compared with Figure 2.4, the GA design exhibits significantly improved symmetry in the gain response between the two principal planes. As a side effect of optimizing pattern symmetry at all frequencies, the gain response of the GA design exhibits improved azimuth symmetry over the wide operating band as well. Therefore the gain response of the GA antenna deviates somewhat from the original square planar monopole.

The simulated and measured attenuation provided by the GA band-notched design relative to the square planar monopole as determined using Equations 2.2 and 2.4 are presented in Figure 2.12. Good agreement is achieved between measurement and simulation. The GA design exhibits nearly identical attenuation responses in the notch band between the two principal planes, with high peak attenuation levels, in excess of 20 dB, occurring at the same frequency. The attenuation performance of the GA design is summarized in Table 2.2. Comparing these results with Table 2.1, it can be seen that the GA design offers a significant improvement in band-notch performance over the original band-notched design. For a relative attenuation level of 5 dB, the GA design offers nearly a five times improvement in effective bandwidth over the original design. Furthermore, the GA design exhibits reasonable bandwidths for higher attenuation levels, which the original design does not. These bandwidths are suitable for use in mitigating interference between wideband radio systems and a wide range of narrowband radio systems.

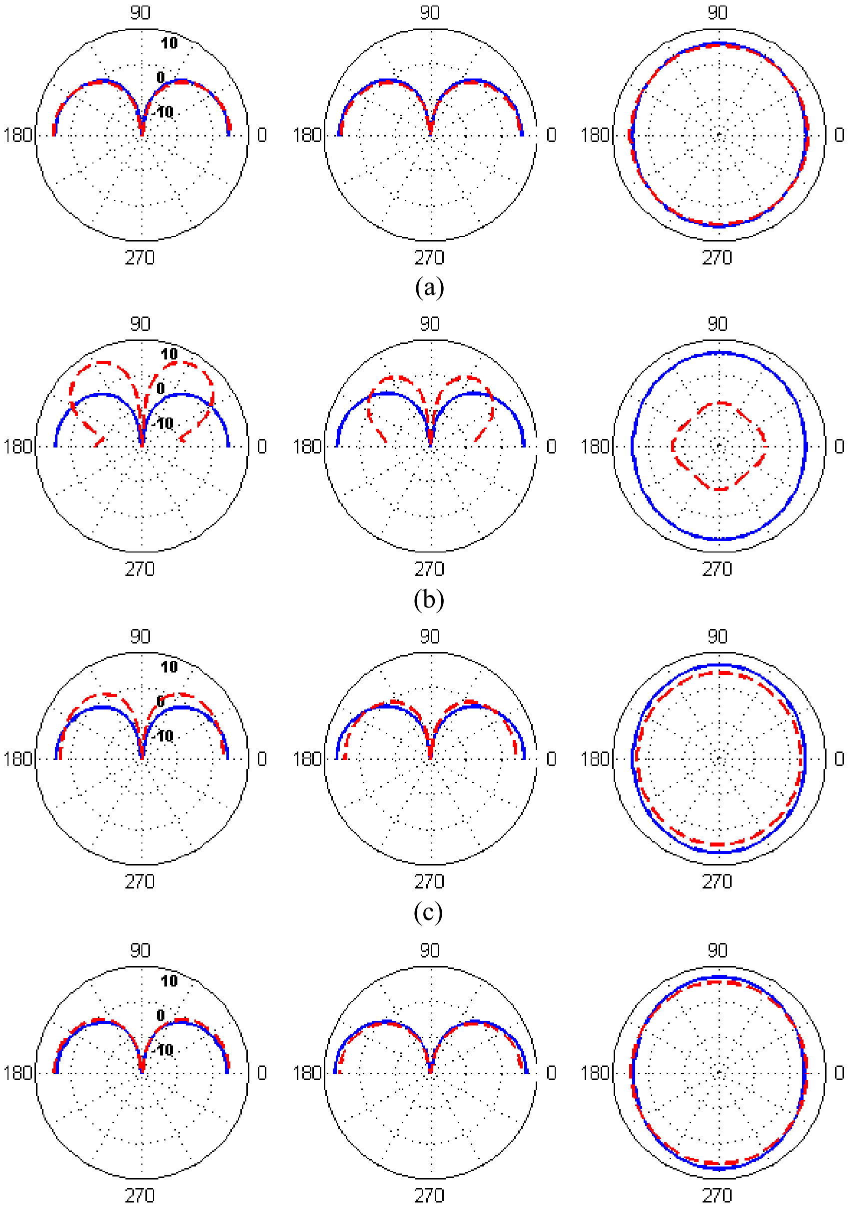

(a)

(b)

(c)

(d)

Figure 2.10: Simulated radiation patterns for the un-notched square planar monopole (solid), and the GA band-notched design (dashed.) From left to right, x-z plane, y-z plane, x-y plane. (a) 1100 MHz, (b) 1350 MHz, (c) 1400 MHz, (d) 1600 MHz.

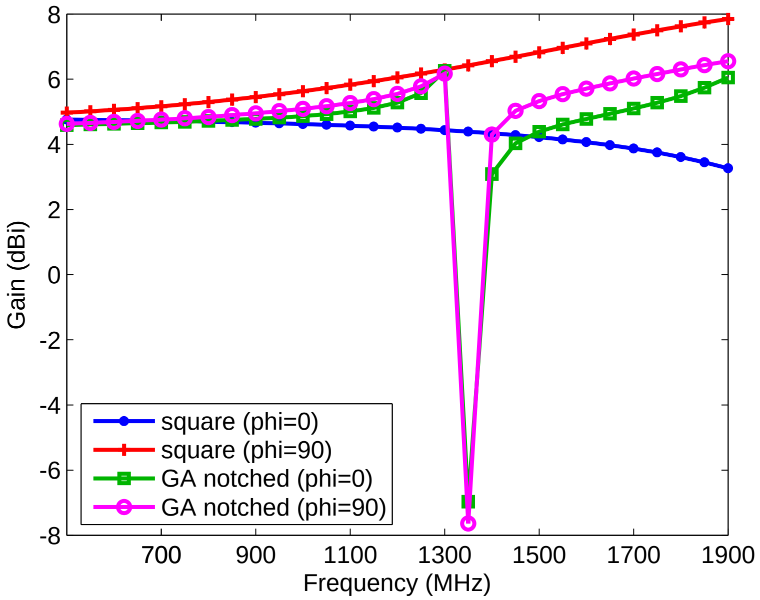

Figure 2.11: Simulated gain of the GA band-notched design (GA notched) and the un-notched square planar monopole (square) in the two principal planes ($\phi = 0^\circ$ and $\phi = 90^\circ$) at the horizon ($\theta = 90^\circ$).

Table 2.2: Measured fractional bandwidths over which different attenuation levels are achieved by the GA band-notched design in each principal plane at the horizon. Also provided is the corresponding bandwidth over which each attenuation level is achieved simultaneously over all azimuth angles.

	Fractional bandwidth (%) in $\phi = 0^\circ$ plane	Fractional bandwidth (%) in $\phi = 90^\circ$ plane	Effective fractional bandwidth (%) over all ϕ
Attenuation $>$ 5 dB	4.38	5.60	4.38
Attenuation $>$ 10 dB	2.31	2.53	2.31
Attenuation $>$ 15 dB	1.34	1.41	1.34

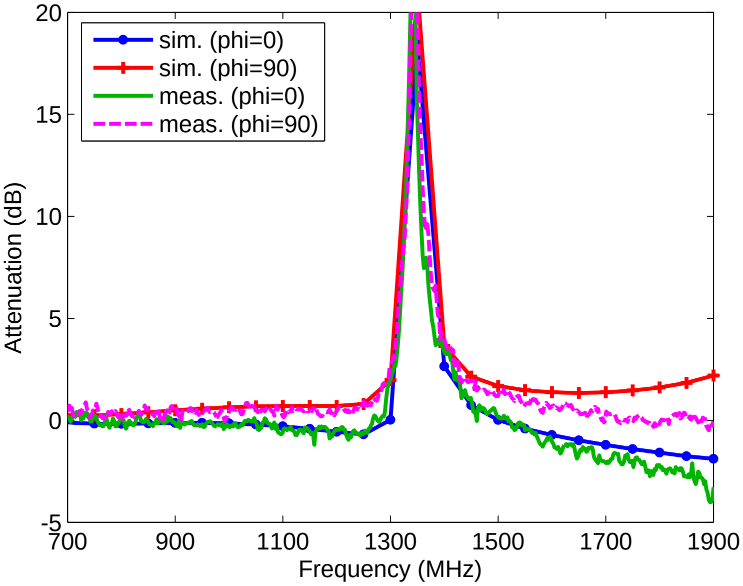

Figure 2.12: Comparison of simulated and measured relative attenuation provided by the GA band-notched design relative to the un-notched square planar monopole in the two principal planes ($\phi = 0^\circ$ and $\phi = 90^\circ$) at the horizon ($\theta = 90^\circ$).

2.4 Summary

GA optimization of planar monopole antennas with a band-notch characteristic has been considered in this chapter. It was first shown that a traditional band-notched planar monopole exhibits asymmetry in its azimuth plane radiation patterns, which limits the useful attenuation bandwidth provided in the notch band. A GA optimizer was presented, which uses a matrix-based chromosome to describe the shape of the planar monopole element. It was shown that by simultaneously optimizing impedance matching and radiation pattern characteristics in the GA that the pattern symmetry in the notch band can be improved. The GA optimized band-notched antenna exhibits significantly higher effective attenuation levels and wider attenuation bandwidths than the traditional band-notched planar monopole while maintaining the same desirable wideband characteristics.

Chapter 3

Design of Broadband Antenna Elements for Use in a Low Frequency Radio Telescope Array using a Pareto Genetic Algorithm Optimization Approach

3.1 Introduction

The Long Wavelength Array (LWA) is a synthesis imaging radio telescope currently under development to provide extremely high sensitivity and resolution in the frequency range of 20 MHz to 80 MHz. The LWA will be used in cosmological studies, for example, involving the high-redshift universe and the epoch of reionization, other astrophysical studies involving phenomena such as the interstellar medium, solar radio and space weather research, and ionospheric research [5]. It is currently planned that the LWA will consist of 52 stations spread over a diameter of roughly 400 km. Each station is a phased array of 256 antenna elements placed over a diameter of 100 m.

In order to maximize the sensitivity of the instrument, it is required that the antenna elements receive the Galactic background or “sky” noise at a level much higher than the “self” noise generated by system electronics so that the receive system is sky noise dominated. For a given system noise level, the sky to system noise dominance is primarily influenced by the efficiency of the antenna, which is affected by mismatch loss between the antenna and the input feed, and absorption of incident energy by the ground beneath the antenna. The LWA also requires nearly full-sky view in order to perform beamforming from the zenith to close to the horizon. This implies that a low directivity or wide beamwidth antenna element is desired. Additionally, to achieve high gain in all sky directions and simplify calibration of the instrument, the element patterns should be smoothly varying with observation angle and have minimal ripple. The antenna elements must also provide circular polarization in order to avoid distortion induced by the ionosphere. Since there will be thousands of such elements in the LWA, it is also desired to minimize the monetary cost of the antenna design.

Dipole antenna elements have been used successfully in other low frequency radio telescopes. In these systems, the dipoles are generally placed relatively close to a ground plane (on the order of a quarter wavelength) to maintain wide beamwidth radiation patterns. Additionally, two dipoles are co-located and oriented orthogonally or "crossed" to achieve a circularly polarized antenna. For example, a thin wire "inverted-V" dipole antenna is used in the LOFAR low-frequency demonstrator [6]. While this design is simple and low-cost, it does not provide wideband impedance matching to a low impedance, nominally 100 Ω, input feed such as is planned for LWA. To address this short-coming, dipoles consisting of broadband "drooped" planar elements were developed for the Long Wavelength Demonstrator Array (LWDA), a predecessor to the LWA. The antenna design, which is illustrated schematically in Figure 3.1, exhibits sky noise dominated operation when paired with a 100 Ω feed, and wide beamwidth and low axial ratio radiation patterns over the entire LWDA band of 60 MHz to 80 MHz [14]. These properties make the planar dipole an attractive candidate antenna element for LWA. The much wider bandwidth requirement of the LWA compared with the LWDA, however, makes it more difficult to maintain high sky noise dominance and desirable radiation patterns over all frequencies, and it becomes necessary to make a trade between these two objectives.

Pareto Genetic Algorithms (GA) [41], [42] have become popular for complex antenna design problems involving multiple objectives. In [24], a Pareto GA is used to optimize electrically small wire antennas in terms of input impedance matching bandwidth, radiation efficiency, and antenna size. In [43], Yagi antennas are optimized in terms of gain, sidelobe level, and impedance match. There are few results reported, however, involving Pareto GA optimization of wideband antennas, and no known results involving optimization of such antennas for radio astronomy. In the present study, a Pareto GA is used to optimize planar dipole antennas in terms of both sky noise reception and radiation pattern quality for use in the LWA. Through this approach, the range of available performance trade-offs between the two design objectives will be determined for a number of different design variations. These include different geometrical constraint values, antenna element shapes and orientations, feed impedance values, and ground conditions.

The chapter is organized as follows: The Pareto GA optimizer is first described. Results from GA optimization and measurement of selected antenna designs are then presented. Finally, conclusions are given.

3.2 Pareto GA Optimization Approach

A Non-dominated Sorting GA (NSGA) [22] is used to perform multi-objective optimization of planar dipole antennas for use in the LWA. Sharing is implemented by generating niche counts based upon euclidean distances between designs in objective

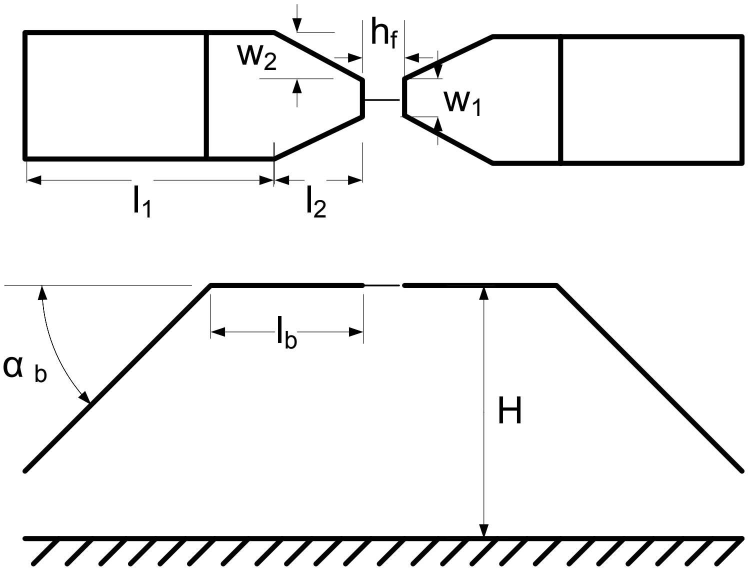

Figure 3.1: Geometry of planar dipole antenna.

space. The niche counts are used to scale the nominal fitness values generated by Pareto sorting. As in a traditional GA, selection, cross-over, mutation, and fitness evaluation are performed in each generation. An elitism operator is implemented in the Pareto GA by performing a second selection step at the end of each generation. In this step, selection is performed on the combined population consisting of both parent and child individuals resulting from crossover and mutation in order to return the population to its original size [44]. Roulette wheel selection is used in the initial selection step, while fitness ranking is used in the second selection step. A binary coded chromosome is used to represent antenna designs in the GA.

Constraints upon antenna geometry are handled explicitly in the GA. Linear constraints of the form $x \leq x_0$ or $x \geq x_0$ may be placed on individual dimensions of the antenna. Additionally, geometrical checks are performed to verify that an element design does not intersect its counterpart element in a crossed dipole antenna, and that no portion of the element extends below the ground plane; tolerances may be specified for each of these checks. If an element design violates any of these constraints, its fitness is set to zero, effectively removing it from the population.

A simulation code based upon the method of moments (MOM) formulation described in [45] is used to estimate antenna performance in the GA. In this formulation, first-order triangular patch basis functions are used to accurately model the current distribution over a planar surface. A Gaussian delta gap feed model is used to excite the antenna. An infinite PEC ground beneath the antenna is modeled by imaging the basis functions of the antenna across the ground plane. An infinite lossy ground beneath the antenna is approximated using a reflection coefficient-based model similar to the one described in [46]. EasyMesh version 1.4 [47] is used to generate triangular mesh discretizations of antenna designs for use in MOM simulation. EasyMesh uses constrained Delaunay triangulation and automatically performs iterative mesh refinement to generate well-conditioned triangular meshes. This code only generates 2-D meshes, however. Therefore, in order to generate a drooped planar dipole as shown in Figure 3.1, it is necessary to individually mesh each planar component, and then apply appropriate rotations and translations to the components to form a model for the complete antenna. An example of an antenna mesh generated using this approach is shown in Figure 3.2.

Note that although a geometrical check is performed to verify that crossed dipoles do not intersect, only a single dipole out of a crossed dipole pair is considered in MOM simulation in the GA. This is done to minimize GA run-time. This is an acceptable simplification to make, however, since crossed planar dipoles have been shown to couple to one another at a low level [48]. Therefore, it is possible to characterize the performance of a crossed dipole antenna with reasonable accuracy through analysis of a single dipole.

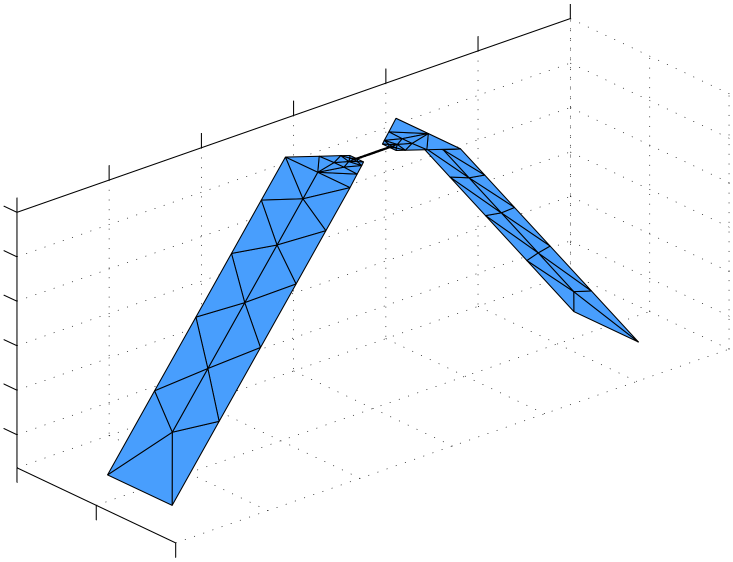

Figure 3.2: An example of a triangular mesh of a planar dipole used in the Pareto GA.

The GA simultaneously optimizes antenna performance in terms of sky noise frequency response and radiation pattern quality over the 20 MHz to 80 MHz operating band. The cost function used in the GA for sky noise frequency response is

$$C_1 = \sqrt{\frac{\sum_{f=1}^{N_f} h(f)}{N_f}} \tag{3.1}$$

where

$$h(f) = \begin{cases} (T_{ant}(f) - T_{ref}(f))^2, & \text{if } T_{ant}(f) < T_{ref}(f) \\ 0, & \text{if } T_{ant}(f) > T_{ref}(f) \end{cases} \tag{3.2}$$

and N_f is the number of frequencies evaluated. Equation 3.1 is the rms error over all frequencies, f, between the equivalent noise temperature at the terminals of an antenna due to sky noise, T_{ant}, and a reference temperature profile, T_{ref}. As implied by the equation, it is desired to achieve an antenna temperature at least as high as the reference temperature profile over all frequencies.

An approximation for the sky noise temperature received by a lossless, low-directivity antenna is [49]

$$T_{sky} = \frac{1}{2k} I_f \frac{c^2}{f^2} \tag{3.3}$$

where k is Boltzmann's constant, c is the speed of light, and I_f is intensity. In Equation 3.3, the intensity is assumed to be that of the Galactic polar region [50]

$$I_f = I_g \, f_{MHz}^{-0.52} + I_{eg} \, f_{MHz}^{-0.80} \tag{3.4}$$

where f_{MHz} denotes frequency in MHz, $I_g = 2.48 \times 10^{-20}$ and $I_{eg} = 1.06 \times 10^{-20}$. The sky noise temperature received by an antenna when losses are considered is given by

$$T_{ant} = T_{sky} \frac{(1 - |\Gamma|^2)}{L_{gnd}} \tag{3.5}$$

where $(1 - |\Gamma|^2)$ represents mismatch loss efficiency between the antenna and feed line, and L_{gnd} is loss due to absorption by the ground beneath the antenna; conductive loss in the antenna elements is generally small and is ignored here. Ground loss is calculated as the ratio of the total power radiated by the antenna in the upper hemisphere (above the ground) to the total power input to the antenna, P_{rad}/P_{in}, where

$$P_{rad} = \frac{1}{2\eta_0} \int_0^{2\pi} \int_0^{\pi/2} \left(|E^{\theta}(\theta,\phi)|^2 + |E^{\phi}(\theta,\phi)|^2 \right) \sin\theta d\theta d\phi \ , \tag{3.6}$$

$$P_{in} = \frac{|V_{in}|^2}{2} \mathbf{Re} \left\{ \frac{1}{Z_{in}} \right\} \ , \tag{3.7}$$

E^{θ} and E^{ϕ} are the calculated radiated field components, Z_{in} is the calculated input impedance, V_{in} is the exciting voltage, and η_0 is the wave impedance of free space.

As discussed in [49], Equation 3.3 makes the simplifying assumption that the collecting area of the antenna is constant for all observation angles above the ground plane. Though dipole antennas may exhibit wide pattern beamwidths, the collecting area of any real antenna will vary with observation angle. Also, Equation 3.4 is technically only valid at the time in each sidereal day when the Galactic pole transits. Therefore, the equivalent noise temperature received by a real antenna will deviate somewhat, in a time-varying fashion, from the value given by Equation 3.5. Despite these approximations, Equation 3.5 can be used to accurately calculate the ratio of the minimum sky noise values received by two different antenna designs over the course of a sidereal day. This ratio is useful in the context of Pareto optimization in the sense that it relates the relative receive performance of different antenna designs. While the absolute sky noise temperature received by an antenna may be calculated quite accurately using the sky map simulation method described later in this chapter, this method is very computationally intensive. The calculation of received sky noise, as described above, is trivial, and is therefore more appropriate for repeated execution in the GA optimizer.

The reference temperature profile, T_{ref}, is determined by the desired level of sky noise dominance, $D = T_{ant}/T_{sys}$, where T_{sys} is the noise generated by system electronics. For LWA, a sky noise dominance of 10 dB is desired, though 6 dB has been determined to be acceptable. For D = 10 dB and assuming $T_{sys} = 250$ K, the nominal reference temperature is $T_{ref,nom} = 2500$ K. At lower frequencies where $T_{sky} \geq T_{ref,nom}$, T_{ref} is set to $T_{ref,nom}$. At higher frequencies where this is not the case due to the rapid decrease in sky noise temperature with frequency, T_{ref} is set to T_{sky}. The relation between sky noise, T_{sky}, and the reference temperature profile,

T_{ref} is illustrated graphically in Figure 3.3.

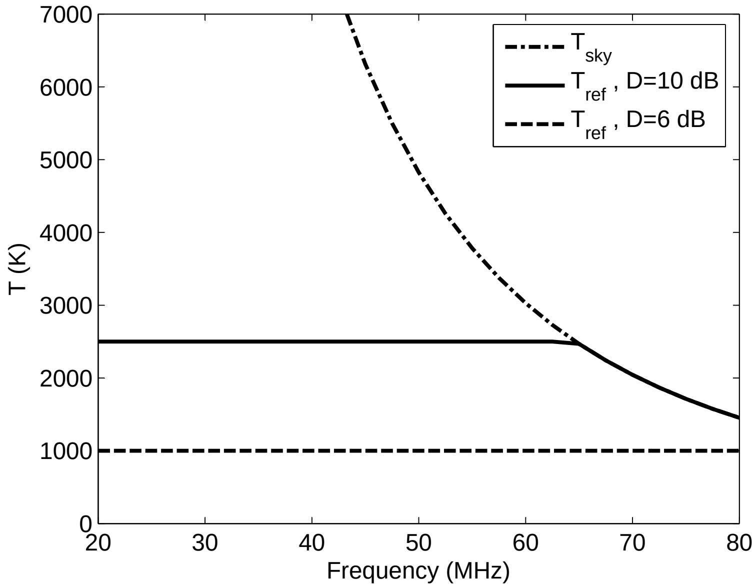

Figure 3.3: Comparison of sky noise and reference temperature profiles for sky noise dominance of 6 dB and 10 dB assuming $T_{sys} = 250$ K.

The cost function for radiation pattern quality is

$$C_2 = \max_{all\, f} \left\{ \sqrt{\frac{\sum_{i=1}^{N_\theta} \sum_{j=1}^{N_\phi} \left(G_{ant}(f,i,j) - G_{ref}(f,i,j)\right)^2}{N_\theta N_\phi}} \right\} \tag{3.8}$$

which is the maximum over all frequencies of the rms error over all observation angles between the gain pattern of an antenna, G_{ant}, and a reference gain pattern, G_{ref}; N_θ and N_ϕ are the number of elevation and azimuth angles, respectively, over which patterns are evaluated. In the calculation of C_2, G_{ant} is normalized at each frequency to the maximum over all elevation and azimuth angles. It is desired to minimize both C_1 and C_2.

3.3 Results

3.3.1 Initial Pareto GA Study

As an initial design case, the Pareto GA is used to optimize the planar dipole geometry depicted in Figure 3.1. The dipole is assumed to operate directly over an "average" lossy ground with a relative permittivity of 13 and a conductivity of 0.005 S/m. The GA evaluates each antenna design in 10 MHz increments between 20 MHz to 80 MHz. In evaluating C_1, a nominal reference sky noise temperature of $T_{ref,nom}$=2500 K is used, which corresponds to a sky to system noise dominance of D=10 dB given a system noise of 250 K. A feed impedance of 100 Ω is assumed in calculating mismatch loss. $G_{ref} = \sin\theta$ is used to calculate C_2. Radiation patterns are calculated in three degree increments in both elevation and azimuth. In addition to the constraints which forbid crossed elements from intersecting and elements extending beneath the ground, an additional constraint that the total width of the dipole element, $w_T = w_1 + 2w_2$ (referring to Figure 3.1), be less than 42 cm. This constraint is added in order to limit the total amount of sheet metal required to manufacture the dipole elements, and thus the monetary cost of the antenna. Otherwise, the remaining design parameters are allowed to vary over a relatively wide range in order to thoroughly explore available design trade-offs.

The eight dipole design parameters shown in Figure 3.1 are encoded in the GA using a 44 bit chromosome. A population size of N_p=200 is used and the GA runs for 300 generations before terminating. A cross-over rate of 0.5 and mutation rate of 0.1 are used. The niche radius used in the Pareto sharing scheme is $r_{niche} = (1/N_p) = 0.005$.

The GA took 119 hours to execute using six 1.0 GHz AMD Athlon processors. The Pareto fronts generated by the GA at generations 1, 50, 300 are shown in Figure 3.4. After the first generation, there are very few designs on the front. The front is greatly improved and contains many more designs after generation 50. By the final generation, the front is improved somewhat further and contains nearly the entire population (177 out of 200 designs.) The final front is relatively smooth and evenly sampled over a wide range of values for both objectives.

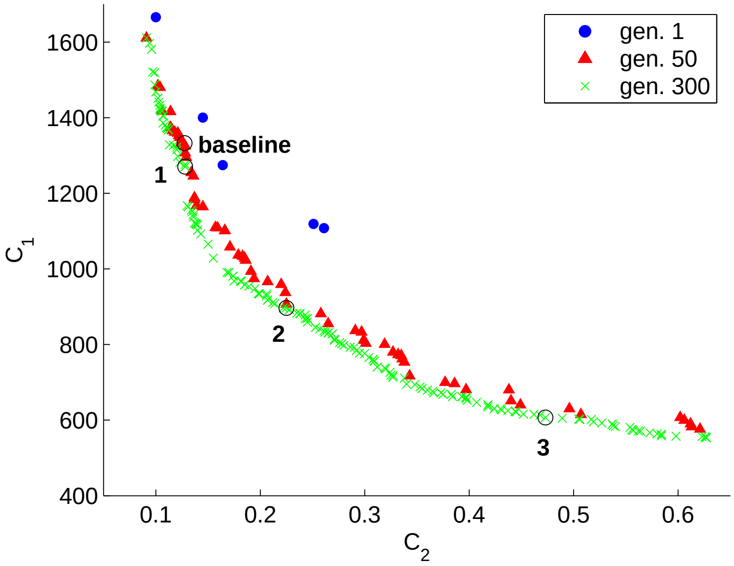

Figure 3.4: Pareto GA results for preliminary design case.

Three designs from the final Pareto front, labeled designs 1,2, and 3 in Figure 3.4, are selected for detailed analysis. The sky noise frequency responses calculated using Equation 3.5 for these three designs are compared in Figure 3.5. Also included in the figure for comparison are the reference sky noise profiles as defined in Section 3.2 for both $T_{ref,nom}$ = 2500 K (D=10 dB) and 1000 K (D=6 dB). Design 1, which has the highest (worst) C_1 value of the three designs, exhibits the lowest equivalent sky noise temperatures over most frequencies. The bandwidths over which design 1 performs better than the D=10 dB and D=6 dB reference profiles are relatively narrow. Sky noise temperatures consistently increase between designs 1 and 2 and between designs 2 and 3, particularly at the low and high ends of the operating band. The bandwidths over which designs 2 and 3 satisfy the reference profiles are also increased. Design 3, in fact, meets or exceeds the D=6 dB profile over the entire 20 MHz to 80 MHz band, though none of the designs satisfy the D=10 dB profile above 43 MHz for the assumed system noise.

The normalized principal plane co-polarized gain patterns for the three GA designs at 30 MHz and 80 MHz are given in Figure 3.6. Also included for comparison in each plot is the reference gain pattern, $\sin\theta$. As would be expected, all three designs exhibit relatively wide beamwidth and smoothly varying radiation patterns near the low end of the operating band. Though the patterns of design 1 follow the reference pattern well, design 2 and particularly design 3 exhibit reduced E-plane beamwidths at 30 MHz. At 80 MHz, all three designs exhibit some pattern ripple, though the patterns of design 1 follow the reference pattern relatively closely. Design 2 patterns exhibit reduced E-plane beamwidth and increased ripple in the H-plane. In the patterns of design 3, the gain near the zenith is considerably lower than that of the sidelobes, which is undesirable.

As discussed previously, although only a single dipole is included in simulation when evaluating a given antenna design in the GA, it is possible to infer some aspects of the crossed dipole antenna performance from analysis of the single dipole. For instance, the principal plane axial ratio with which the crossed dipole receives a circularly polarized signal can be approximated by

$$AR(\theta) \approx |G^E(\theta) - G^H(\theta)| \tag{3.9}$$

where G^E and G^H are the co-polarized E- and H-plane gain patterns of the single dipole. The calculated axial ratios for designs 1,2, and 3 at 80 MHz are compared in Figure 3.7. Comparing Figure 3.7 with Figure 3.6, it can be seen that dipole designs with radiation patterns that follow the reference pattern more closely, also exhibit lower axial ratio values or better reception of circularly polarized waves over most observation angles when used in a crossed-dipole antenna. This demonstrates that good pattern performance in the single dipole case corresponds to good pattern performance in the crossed dipole case.

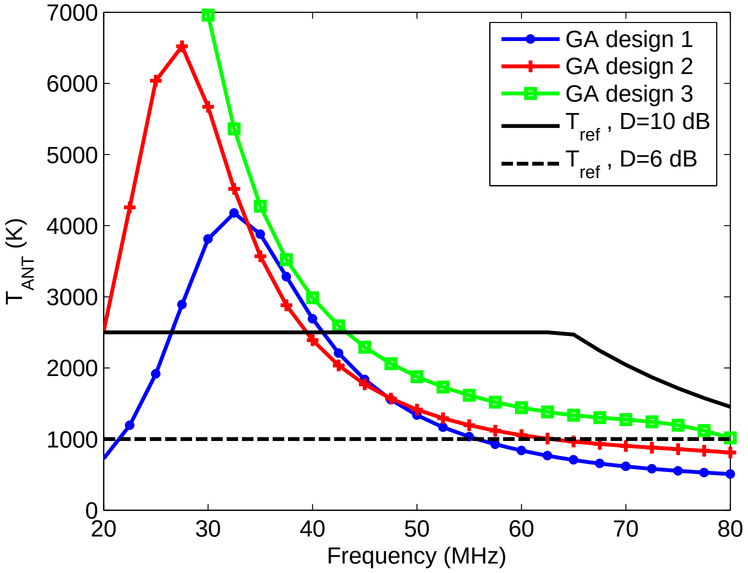

Figure 3.5: Sky noise responses for selected Pareto GA designs.

The performances of the GA designs can be understood through analysis of their dimensions, which are provided in Table 3.1. The total length of the dipole elements, $l_T = l_1 + l_2$, increases between designs 1 and 2 and between designs 2 and 3. The increased length leads to better impedance matching, and thus improved sky noise reception at lower frequencies in the operating band. Additionally, the

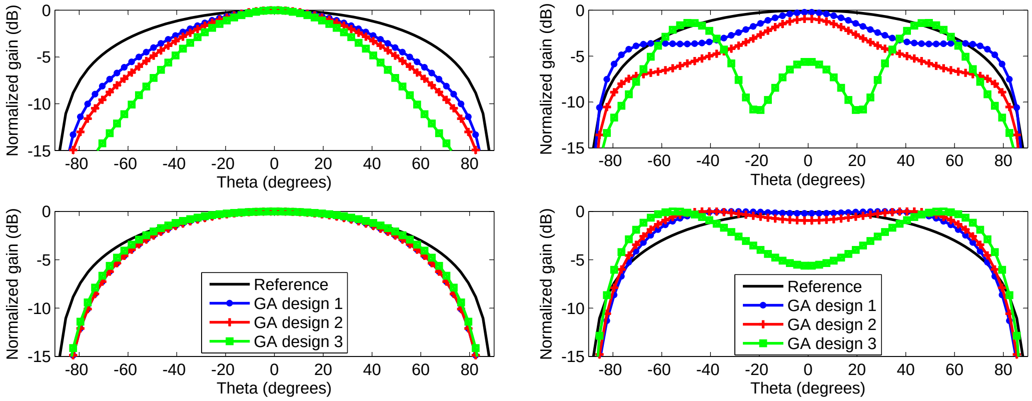

(a) (b)

Figure 3.6: Co-polarized radiation patterns for selected Pareto GA designs at (a) 30 MHz, and (b) 80 MHz. E-plane (top), H-plane (bottom).

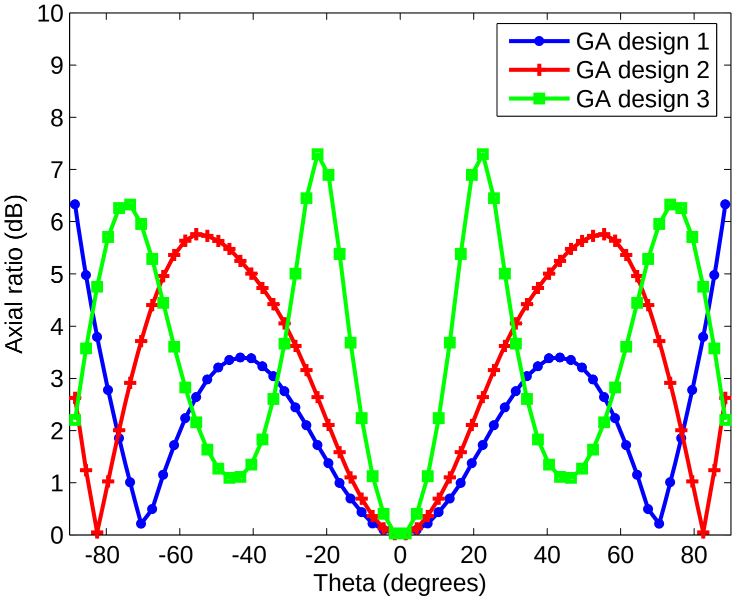

Figure 3.7: Principal plane axial ratio at 80 MHz for crossed dipoles based upon selected GA designs.

element lengths of designs 2 and 3 are such that the $3\lambda/2$ resonance is moved closer to 80 MHz, which improves impedance matching and sky noise reception at higher frequencies. As mentioned in [14], impedance matching is improved and ground loss is reduced by moving the element away from the ground. This can be accomplished by increasing the distance between the feed and the bend point, l_b, which is the case for design 2, by decreasing the droop angle, α, or by increasing the height of the feed point above the ground, h_f, both of which are the case for design 3. However, as also mentioned in [14], increasing the distance between the element and the ground degrades radiation patterns, principally E-plane beamwidth. Also, increasing the length of the element will tend to degrade high frequency radiation patterns by introducing sidelobes.

Table 3.1: Dimensions of selected Pareto GA designs.

	GA 1	GA 2	GA 3	Baseline
$l_1(cm)$	150.0	197.2	200.0	137.1
$l_2(cm)$	21.2	13.1	42.8	35.0
$w_1(cm)$	8.6	4.4	14.3	2.5
$w_2(cm)$	16.0	18.6	13.8	19.8
$h_f(cm)$	8.8	10.0	9.6	5.0
$H(cm)$	132.9	121.4	164.3	152.4
$l_b(cm)$	17.1	113.6	65.6	6.4
$\alpha_b(deg.)$	32.2	51.5	6.6	45.0

3.3.2 Validation of GA Results

Two antenna designs were constructed and measurements were performed to verify the accuracy of MOM simulation, and thus validate the results generated by the Pareto GA. The first of these is a planar dipole considered to be the “baseline” antenna design for LWA, which is described in [51]. This design is selected for evaluation in the present study since its performance is already well understood through previous analysis. The dimensions of this design are included in Table 3.1, and its cost function values are shown in Figure 3.4 were it is evident that this design resides behind the final Pareto front. The second antenna constructed is Pareto GA design 2 described in Section 3.3.1. Pictures of the constructed antennas are provided in Figure 3.8.

Measurements of input impedance were performed on both antenna designs using a vector network analyzer (VNA). The antenna under test is placed in an open field, and connected to the VNA via a long coaxial cable. A VNA calibration is performed at the end of the coaxial cable. At the antenna, the cable is then connected to the input of a balun, and short adapter cables are connected between the balun outputs and the dipole elements as shown in Figure 3.9. Since the setup is only calibrated up to the balun input, the VNA reflection coefficient measurement will contain the responses of the balun and the adapter cables in addition to the desired response of the antenna. In order to isolate the reflection coefficient, and thus the input impedance of the antenna itself, it is necessary to extract the responses of the balun and adapter cables from the measurement. A procedure based upon scattering-parameter or S-parameter analysis is used for this purpose and is described in Appendix A.

Since a ground screen is not used in these measurements, the antenna response will vary depending upon the relative permittivity and conductivity of the soil beneath the antenna. Therefore, these parameters are measured as a function of frequency using the ground probe-based technique described in [53]. The measured soil permittivity and conductivity are averaged over 20 MHz to 80 MHz, and the resulting values are used in simulation.

The measured and simulated impedances of the two antenna designs are compared in Figure 3.10. Measurements were first conducted with the center supporting masts installed in the antennas as depicted in Figure 3.8. Although good agreement is achieved between simulation and measurement over most frequencies, there is some disagreement near the full-wave resonances of the antennas. This disagreement is exhibited as a shift in resonance frequencies and different peak impedance values. The measurements were repeated after removing the center masts from the antennas; the struts near the ends of the antenna elements were used to temporarily maintain the antenna geometry. This significantly improves the agreement between measurement and simulation. This is due to the fact that the dielectric properties of the mast, which are not included in simulation, can affect the antenna response, especially when placed near the feed. A shift of roughly 4% in the full-wave resonance frequency of the baseline design, and a small offset in the high frequency reactance of GA design 2 remain. Otherwise, the agreement in results is very good for both designs, which suggests that the MOM code accurately calculates the current distributions of planar dipoles.

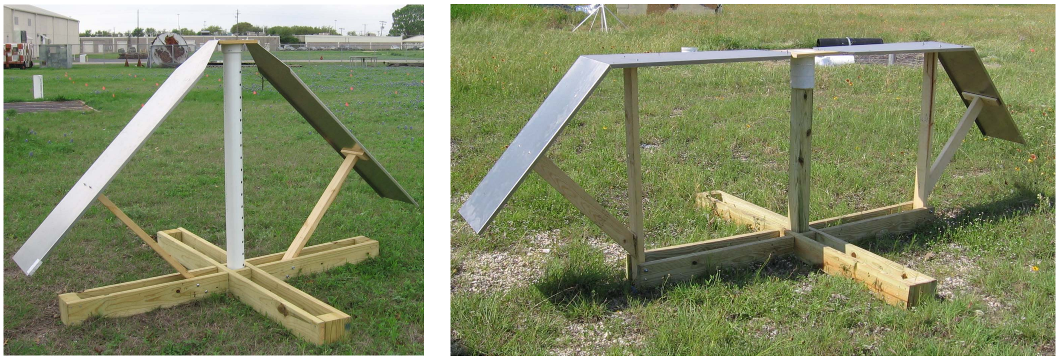
(a)

(b)

Figure 3.8: Built versions of planar dipole antenna designs. (a) LWA baseline design, (b) Pareto GA Design 2.

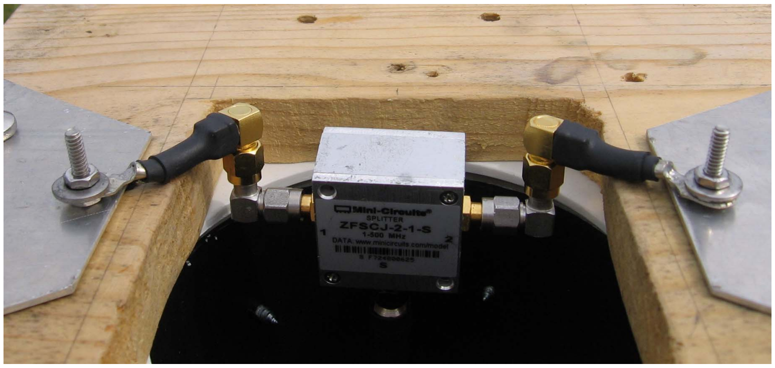

Figure 3.9: Detail of the connection between the balun and antenna elements.

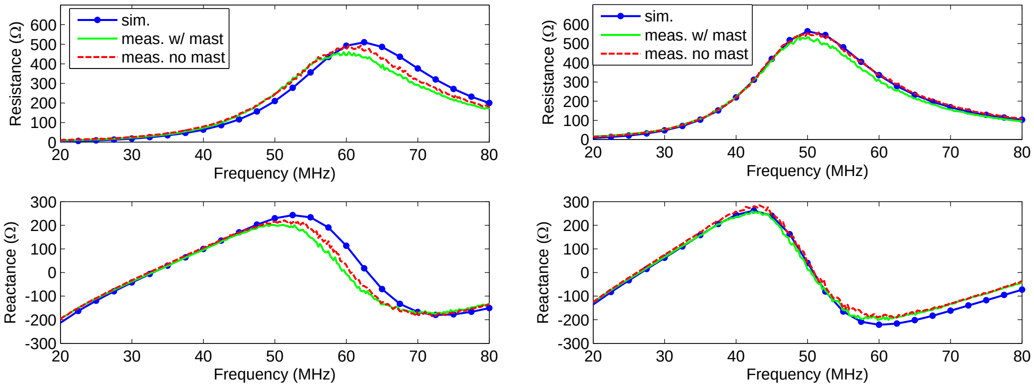

(a)

(b)

Figure 3.10: Comparison of measured and simulated input impedances. (a) LWA baseline design, (b) Pareto GA Design 2.

Drift scans, which consist of measuring the total power due to sky noise received by an antenna over an extended period of time, were performed with each antenna. The sky noise power received by the antenna varies diurnally in a deterministic fashion as different astronomical sources (most principally in the Galactic plane) go in and out of view of the antenna due to the rotation of the Earth. The drift scan response is strongly affected by the efficiency of the antenna, which is related to both impedance mismatch and ground losses, as well as its radiation patterns. Therefore drift scan measurements can provide a more complete validation of simulation results than impedance measurements alone.

The test setup used for these measurements is shown in Figure 3.11. The antenna is connected directly to a wideband active balun, which transforms between a 100 Ω balanced output and a 50 Ω unbalanced input, and provides 24 dB of gain with an equivalent noise temperature of roughly 250 K [54]. The output of the active balun is connected by a length of low-loss coaxial cable to a bias-T, which provides power to the active balun. The output of the bias-T is connected to an LC filter, which bandpasses the response to approximately 20 MHz to 80 MHz. This filter is used to reduce the received power due to out of band radio frequency interference (RFI) in order to avoid generation of inter-modulation products or saturation in downstream components. The output of this filter is fed to an additional 24 dB amplification stage and then to a spectrum analyzer. A laptop is used to control the spectrum analyzer, and log measurement data. The spectrum analyzer measures the total power collected by the antenna over the frequency range of 20 MHz to 80 MHz, in 10 kHz intervals, once every 5 minutes for a period of at least two consecutive days.

A relatively simple procedure is used to process drift scan measurement data. Each raw data file, which corresponds to a single sweep over the 20 MHz to 80 MHz band, is sub-divided into bins each 50 points, or 500 kHz, in width. In each bin, iterative outlier removal is performed in an attempt to remove RFI, and the mean is calculated on remaining points to reduce measurement noise.

Though it is desired to measure the sky noise received by the antenna, the raw drift scan measurement contains noise due to both the sky and system electronics.

Therefore a Y-factor calibration [52] is performed on the test setup. A noise diode with known temperature is connected in place of the antenna and a total power measurement is taken; the measurement is repeated after turning off power to the noise diode. These two measurements are combined to generate estimates of the gain and noise temperature of the test setup. The raw drift scan measurement is then corrected using these values to determine the sky noise received by the antenna, which can be compared directly with simulation results. This correction is applied individually for each data bin.

Drift scan measurements with the two antennas were performed two weeks apart from one another at a rural site roughly 35 miles west of Austin, TX. The peak RFI levels were found to be much lower there than in the city. Antennas are placed in a relatively open area at this site to provide nearly full sky view. As with impedance measurements, drift scan measurements are performed with the antenna operating directly over an Earth ground. Therefore it is necessary to conduct ground parameter measurements, as described previously, prior to each drift scan measurement.

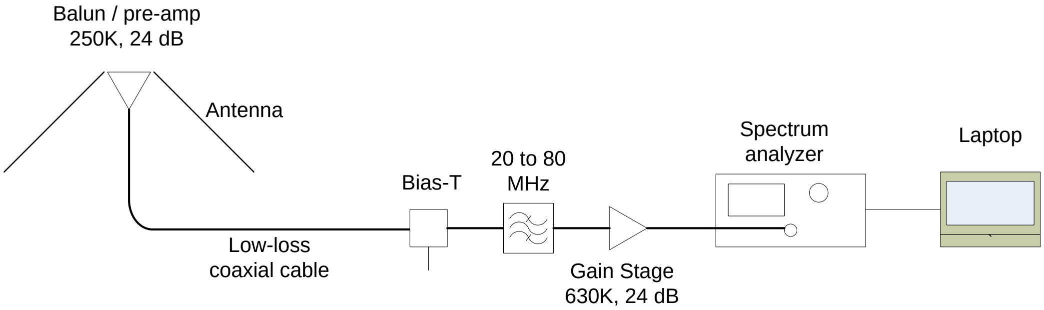

Figure 3.11: Test setup used for drift scan measurements.

The drift scan response of each antenna is predicted by convolving simulated radiation patterns with an all-sky map of radio continuum. In particular, the equivalent noise temperature due to sky noise for a lossless antenna at a given time, t, is given by [55]

$$\begin{aligned} T_{sky}(t) &= \frac{1}{\sum_{i}\sum_{j} U\left(\theta(i,j)\phi(i,j)\right)\cos b(i)} * \\ &\quad \sum_{i}\sum_{j} M\left(i,j\right)\, U\left(\theta(i,j)\phi(i,j)\right)\cos b(i) \end{aligned} \tag{3.10}$$

where M denotes the all-sky map, i and j are the map indices for galactic latitude and longitude, respectively, U is the normalized power pattern of the antenna, and b(i) is the galactic latitude corresponding to i. $\theta(i,j)$ and $\phi(i,j)$ are the elevation and azimuth, respectively, relative to the frame of the antenna and corresponding to the direction, in terms galactic latitude and longitude, indicated by i and j. The relationship between the galactic latitude and longitude of a source and antenna-referenced elevation and azimuth varies as a function of time due to the rotation of the earth. The noise temperature received by an antenna when losses are taken into account, T_{ant}, is given by Equation 3.5.

The Haslam 408 MHz all-sky map [56] is used in this study. Prior to simulation, this map must first be scaled to the observation frequency, which in the case of LWA, varies between 20 MHz to 80 MHz. A typical approach is to scale the entire map by a constant factor according to

$$M_{sc,orig} = M\left(\frac{f_{obs}}{f_{map}}\right)^{-\beta_0} \tag{3.11}$$

where f_{map} is the map frequency, f_{obs} is the observation frequency, and β_0 is the spectral index, which is assumed to be constant between f_{map} and f_{obs}. The approach taken in this study is to handle separately the contributions to sky noise due to the Galactic component, the extra-Galactic component, and the cosmic microwave background (CMB). The galactic component of sky noise is scaled from f_{map} to an intermediate frequency, f_{int}, by one spectral index, β_1, and then between f_{int} and f_{obs}, by another spectral index, β_2 to account for the known bend in spectral index near 200 MHz [57]. All pixels in the map are scaled according to

$$\begin{aligned} M_{sc,new} &= [M - T_0 - T_1(f_{map})] \left(\frac{f_{int}}{f_{map}}\right)^{-\beta_1} \left(\frac{f_{obs}}{f_{int}}\right)^{-\beta_2} \\ &\quad + T_1(f_{map}) \left(\frac{f_{obs}}{f_{map}}\right)^{-\beta_3} + T_0 \end{aligned} \tag{3.12}$$

where T_0 is noise temperature of the CMB component, $T_1(f_{map})$ is the noise temperature of the extra-galactic component at the map frequency, and β_3 is the spectral index of the extra-Galactic component. Values for these parameters were obtained from astronomic survey data provided in [58] and are $T_0 = 2.7$ K, $T_1(f_{map}) = 3.2$ K, $f_{int} = 38$ MHz, $\beta_1 = 2.6$, $\beta_2 = 2.4$, and $\beta_3 = 2.75$.

Simulated and measured drift scan data for the two antenna designs, presented in terms of equivalent sky noise temperature referenced to the antenna terminals, are compared as a function of frequency for two different points in time, 37 hours and 47 hours past 00:00 local sidereal time (LST) on the first day of testing, in Figure 3.12. Apart from the large spike due to TV channel 2 between 50 and 60 MHz, the measurement data for both antennas above 50 MHz are relatively RFI-clean. Good agreement is seen between measurement and simulation at these frequencies for both designs and at both times. The measurement data clearly indicates that GA design 2 exhibits improved sky noise reception compared with the baseline design above 50 MHz. At lower frequencies, a comparison between simulation and measurement is more difficult to make due to RFI that is present most of the time. Occasionally, RFI is reduced at these frequencies, and results appear to agree well. This can be seen in Figure 3.12(b) for example at 26.5, 32, and 38 MHz for the baseline design, and 25, 35, and 43 MHz for GA Design 2. The 22.5 MHz bin, however, was found to be RFI-clean over extended portions of the measurements for both antennas. At this frequency, an offset between simulation and measurement is evident for both designs. The offsets in simulated low frequency sky noise temperatures, however, have similar magnitudes for the two antenna designs. Therefore as predicted by simulation, the measured sky noise for GA design 2 at 22.5 MHz is significantly higher than for the baseline design. The relative performances of the two designs in terms of sky noise reception shown here are consistent with the relative cost function values shown in Figure 3.4. The likely causes for the low frequency discrepancies between measurement and simulation will be addressed later in this section.

The drift scan data for GA design 2 is presented as a function of time for the four frequency bins with the least amount of RFI contamination, 22.5 MHz, 49.5 MHz, 65.6 MHz, and 79.0 MHz, in Figure 3.13; the results for the baseline antenna design are similar, and thus, are not presented. At each frequency, an additional scaling factor has been applied to the simulated results in order to achieve the best possible fit with the measured data. This was done to simplify the comparison of temporal trends in measured and simulated results. The scaling factors applied at each frequency are noted in the plot legends in Figure 3.13. Despite haven chosen the cleanest measurement bands available, it can be seen that some interference remains, particularly at the lowest band 22.5 MHz where multiple, long-duration spikes are apparent. There appears to be an extended period of relatively clean data, however, between 37:00 to 55:00 LST for most frequencies. The cleanest period for 79.0 MHz occurs between 15:00 and 25:00 LST, however.

In the clean periods of measurement data, it is apparent that the shapes of the simulated drift curves agree well with those of the measured drift curves at all frequencies. From inspection of Equation 3.10, it is evident that the shapes of the drift curves with time are completely dependent upon the radiation patterns of the antenna. Therefore, the agreement shown in Figure 3.13 indicates that the radiation patterns calculated using the MOM code are accurate for all frequencies. At the three highest frequencies considered, a good fit between measurement and simulation is achieved by applying a scale factor of magnitude 0.6 dB or less. This suggests that at high frequencies, simulation provides a good estimate of both mismatch loss and ground loss. As expected from Figure 3.12, a relatively large scaling factor, -3.5 dB, is applied to simulation at 22.5 MHz to achieve good agreement with measurement. Although not shown here, a similar best-fit scaling factor of -3.3 dB was determined for the baseline antenna design simulation at 22.5 MHz. Since good agreement in measured and simulated input impedances was previously demonstrated, this implies that there is likely some error in the simulated ground loss calculation at this frequency. This error could result from using the approximate reflection coefficient-based ground model in the MOM code, which tends to be less accurate at lower frequencies than higher frequencies. Some error may also be due to not explicitly accounting for HII absorption near the Galactic center in the skymap simulation procedure, which will tend to reduce the measured sky noise at frequencies below 50 MHz as compared with the expected value from Equation 3.12 [57]. As discussed previously, despite these limitations, the MOM code appears to correctly predict the *relative* performances of different antenna designs at low frequency.

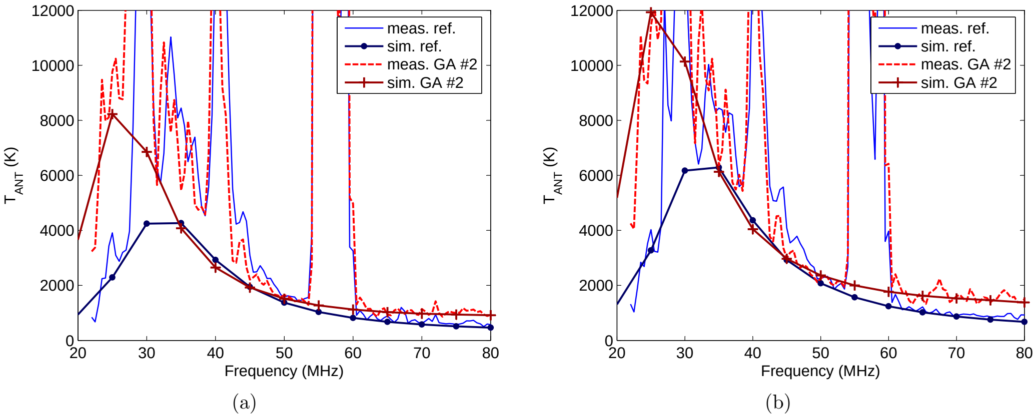

(a)

(b)

Figure 3.12: Comparison of measured and simulated drift scan results for the baseline design and GA design 2 in the frequency domain at (a) 37 hours past 00:00 LST, and (b) 47 hours past 00:00 LST on day one of testing.

3.3.3 Pareto GA Study of Design Variations

The Pareto GA optimizer is now used to study how performance trade-offs are affected when different aspects of the antenna design problem presented in Section 3.3.1 are changed. The effect of changing the element width constraint value, $w_{T,max}$, is first considered assuming the original planar dipole antenna geometry shown in Figure 3.1, average ground conditions, and a 100 Ω feed impedance. The GA is re-run for $w_{T,max}$ values of 28 cm and 60 cm; results for $w_{T,max} = 42$ cm were given in Section 3.3.1. The final Pareto fronts generated after 300 generations by the three GA runs are compared in Figure 3.14(a). For values of C_2 below 0.11, the difference between the fronts is relatively small, with higher values of $w_{T,max}$ only offering marginal improvement in performance. However, for higher values of C_2, the fronts diverge, and performance is improved significantly as $w_{T,max}$ is increased. Simulated input impedances for designs from each front, which satisfy $C_2 = 0.20$, are compared in Figure 3.15(a). In each case the GA has selected an element width close to the

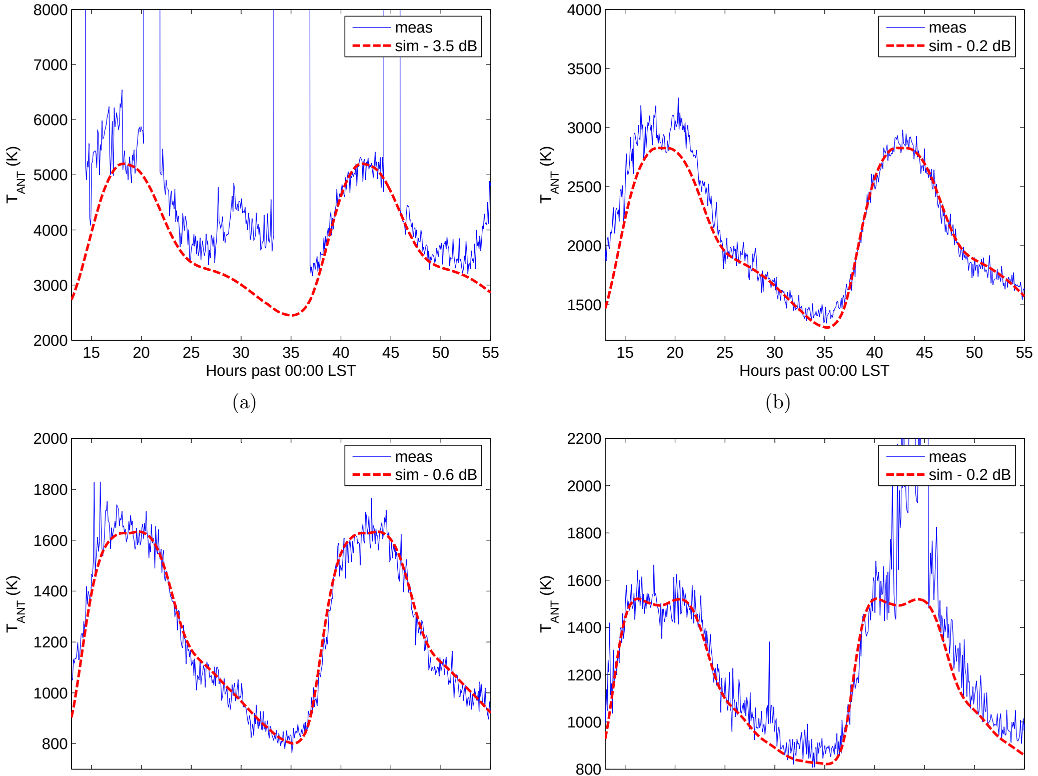

(a) (b)

(c) (d)

Figure 3.13: Comparison of measured and simulated drift scan results for GA design 2 in the time domain at (a) 22.5 MHz, (b) 49.5 MHz, (c) 65.6 MHz, (d) 79.0 MHz.

specified constraint value, though the lengths of all three designs are similar. As the element width is increased, the amount of impedance variation over the operating band is reduced. This makes it possible to achieve better broadband matching to a low impedance feed line, which is evident in Figure 3.15(b) where the VSWR's for the designs are compared. Improved impedance matching, in turn, leads to improved sky noise reception. The disadvantage of a wider element, however, is that more sheet metal is required to construct the antenna, which increases its monetary cost.

Also included in Figure 3.14(a) is the final front from a GA run in which w_T, max is set to 42 cm, but the feed impedance is increased to 150 Ω. The use of a higher impedance feed line improves the performance trade-off for the full range of C_2. For a given value of C_2, the antenna dimensions selected by the GA for different values of Z_L are very similar. Therefore, the input impedances of the corresponding designs are also very similar, as is evident in Figure 3.15(a). As seen in Figure 3.15(b), however, a better broadband match is achieved with $Z_L = 150\ \Omega$, which improves sky noise reception. The improvement in performance is such that the front for $w_T = 42$ cm and $Z_L = 150\ \Omega$ is nearly as good as that for $w_T = 60$ cm and $Z_L = 100\ \Omega$. This suggests that using a higher feed impedance may be a more cost effective way to improve antenna performance than increasing antenna size. However, if additional circuitry is required between the antenna terminals and the pre-amplifier to increase the feed impedance, the system noise will be increased. This may negate any improvement in sensitivity achieved by reducing mismatch loss.

Next, the effects of changing the radiating element shape and orientation are studied. Four different antenna geometries are considered to determine if improvement in either sky noise reception or radiation pattern quality can be achieved relative to the original geometry described previously. Descriptions of these antenna geometries are as follows:

1. Same as the original geometry, but an additional outward taper is added at the bottom (feed) end of the element (9 design parameters);
2. Same as the original geometry, but an additional downward element bend (for a total of two) is allowed (10 design parameters);
3. Same as the original geometry, but an additional inward taper is added at the far end of the element (10 design parameters);
4. Same as the original geometry, but the bend is removed, and the element is oriented perpendicularly (or vertically) relative to the ground ; the element is allowed to tilt downward from the feed point (7 design parameters).

The GA is re-run for each of these geometries assuming an average ground and $w_{T,max} = 42$ cm. The final fronts for geometries 1 and 2 are nearly identical to the front for the original geometry, meaning that their performances are essentially equal. Therefore, these two geometries are not considered further here. The final fronts for the other antenna geometries are compared in Figure 3.14(b). As can be seen, the fronts for the original geometry and geometry 3 are very similar, but there is some improvement in performance with geometry 3 for lower values of C_1. The inward taper added to the far end of the element in this geometry appears to improve high frequency radiation patterns somewhat. Geometry 4 performs much worse than the other two geometries, particularly for intermediate values of C_1. Comparing GA designs from each front for a common value of C_1, the element height above the ground is much higher for geometry 4 than for the other geometries. For instance at $C_1 = 900$, the chosen element lengths are nearly identical, but the height of geometry 4 is 46% higher than the original geometry. Since the element in geometry 4 is oriented vertically, it must be raised higher in order to clear the ground than the other geometries, which are oriented parallel to the ground. As mentioned in Section 3.3, raising the height of the antenna above the ground will tend to degrade radiation patterns.

Finally, the effects of different ground conditions are considered. Since ground permittivity and conductivity at a given site can change as a function of time, particularly due to changes in soil moisture, it may necessary to install a ground screen beneath the antenna in order to stabilize its response. The effects of a ground screen are approximated in MOM simulation by using an infinite PEC ground; this greatly reduces computation time as compared with modeling a finite-sized ground screen. The final GA fronts for PEC ground and average ground assuming the original antenna geometry, and $w_T, max = 42$ cm are compared in Figure 3.14(c). For $C_2 < 0.17$, a better performance trade-off is achieved with the antenna operating over a lossy ground than a PEC ground. The antenna image due to PEC ground perturbs the dipole radiation patterns such that they do not match well to a $\sin(\theta)$ reference pattern at lower elevation angles. Over lossy ground, the effect of the antenna image is not as pronounced. The 80 MHz radiation patterns of designs from each front, which satisfy $C_1 = 1360$, are compared in Figure 3.16. Over PEC ground, the antenna exhibits high sidelobes near the horizon, which lead to higher values of C_2; this does not occur with a lossy ground. For $C_2 > 0.17$, a significantly better trade-off can be achieved over PEC ground. This is due to ground absorption present when operating over lossy ground, which is not present when operating over PEC ground. The calculated ground loss for designs from each front with $C_2 = 0.31$ are compared in Figure 3.17. As expected, the ground loss is zero with PEC ground, but is significant with lossy ground over all frequencies. For higher values of C_1, the designs from the PEC front have consistently shorter element lengths than those from the lossy ground front. For instance, a length reduction of roughly 25% is achieved with PEC ground relative to lossy ground at both $C_1 = 1270$ and 900. This length reduction may reduce the monetary cost of the antenna by reducing the amount of material needed; this could offset, to some degree, the additional cost incurred by installing the ground screen. The difference in element lengths between different ground types reduces to nearly zero as C_2 is reduced to its minimum value.

3.4 Summary

Pareto GA optimization has been applied to the design of broadband planar dipole antennas for use in the LWA radio telescope. In an initial study, it was shown that the GA can be used to generate a Pareto optimal set of antenna designs providing a wide range of trade-offs between sky noise reception and radiation pattern quality over the 20 MHz to 80 MHz operating band. An analysis was performed on the generated designs to determine how different compromises between these two objectives can be achieved. Two planar dipole designs were constructed, and input impedance and sky noise drift scan measurements were performed on each. In general, good agreement was achieved between measurement and MOM simulation, validating the results of the GA.

The Pareto GA was also used to study the effect of different design variations on antenna performance. By imposing a constraint on antenna width in the GA, a trade-off between antenna performance and antenna size, and thus, monetary cost can be made. Through proper selection of the feed impedance presented

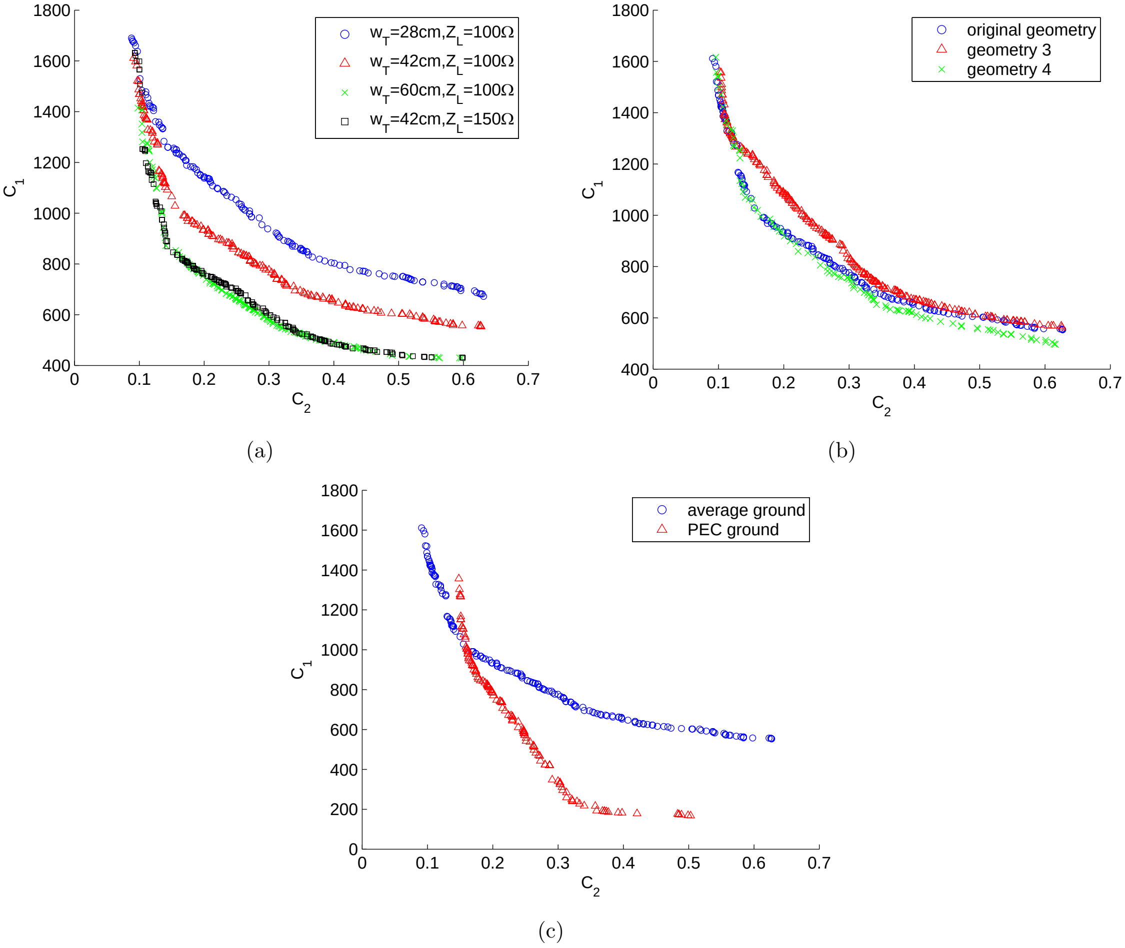

Figure 3.14: Results from Pareto GA design variation study. (a) Vary element width constraint / feed line impedance, (b) vary antenna geometry / orientation, (c) vary ground conditions.

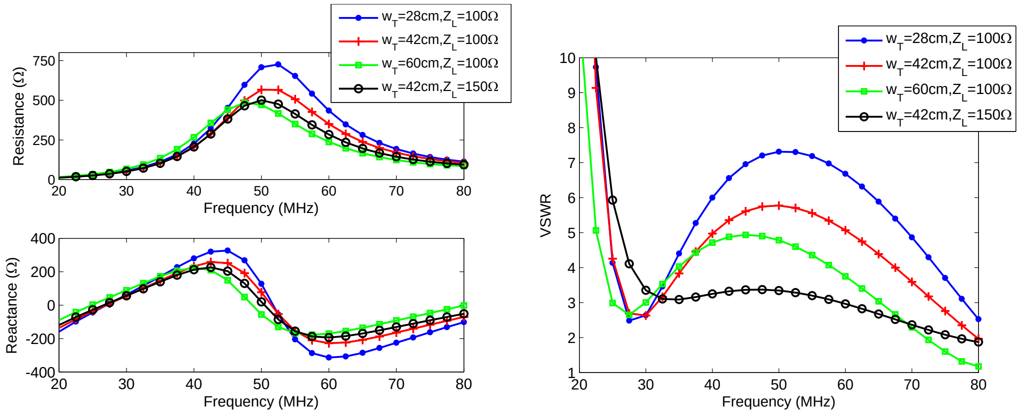

(a) (b)

Figure 3.15: Comparison of GA designs for different element width constraints / feed line impedances assuming $C_2 = 0.2$. (a) Input impedance, (b) VSWR.

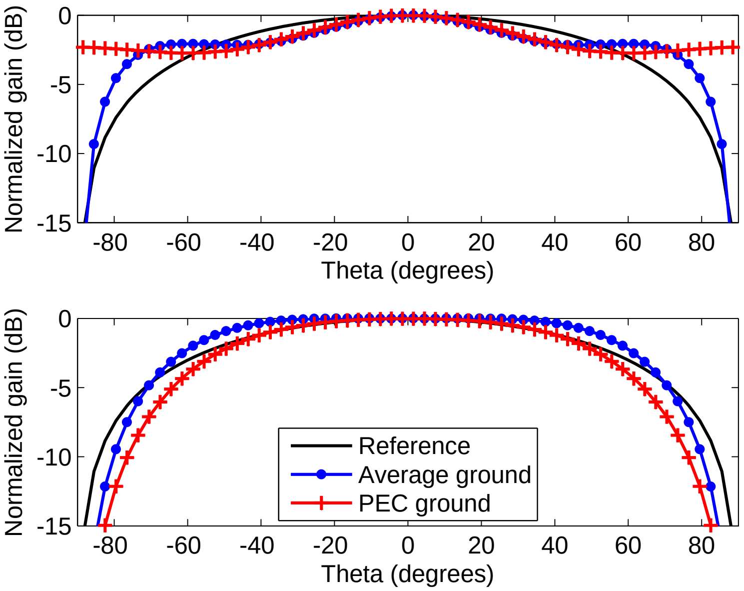

Figure 3.16: Comparison of 80 MHz radiation patterns of GA designs over different ground types and satisfying $C_1 = 1360$. E-plane (top), H-plane (bottom).

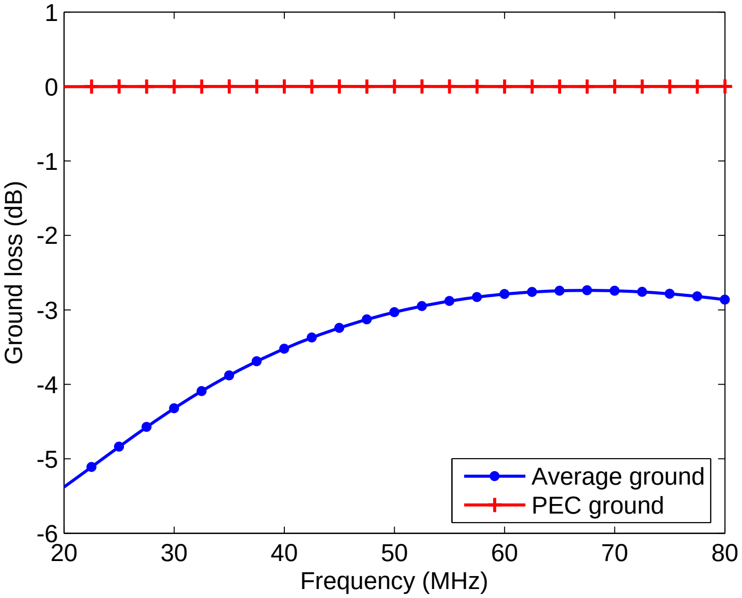

Figure 3.17: Comparison of ground loss for GA designs over different ground types and satisfying $C_2 = 0.31$.

to the antenna, improved performance can be achieved without increasing antenna size, though care must be taken not to increase the system noise in doing so. For the assumed constraints, the shape of the radiating elements only slightly effects the performance trade-off that can be achieved. The orientation of the radiating elements relative to the ground, however, has a more significant effect, with a horizontal orientation performing better than a vertical one. Finally, it was found that the ground beneath the antenna has a significant effect on the performance trade-off with a perfectly conducting ground being far superior in most cases to a lossy ground.

Chapter 4

Pareto Genetic Algorithm Optimization of Antenna Elements for Use in a Low Frequency Radio Telescope Array Including Mutual Coupling Effects

4.1 Introduction

As discussed in Chapter 3, currently planned low frequency radio telescopes, such as the LWA, will consist of a number of phased arrays, referred to as stations, spread over a large area. There are a number of issues to consider in the design of an LWA station. Based upon field of view requirements, the station main beam half-power beamwidth at the zenith should be at least $\psi(\theta = 0) = 2^\circ$ at 80 MHz [7]. Assuming a circular planar array, the required station diameter, D, can be determined using $\psi(\theta = 0) = 1.02(\lambda/D)$, where λ is the operating wavelength [59]. A station diameter of D = 100 m was chosen for LWA. From an analysis of the required collecting area to implement full-field calibration of the full LWA, it was determined that at least 256 antennas per station will be required [60]. A remaining question is how to arrange the antennas within the station. Using a uniform arrangement of antennas, it would be necessary to maintain an inter-element spacing of less than one half wavelength at the highest frequency of operation, or 1.875 m at 80 MHz, in order to completely avoid deleterious grating lobes for scanning down to the horizon. Though in practice, it will not be necessary to scan all the way to the horizon, a relatively small inter-element spacing, and thus a large number of antenna elements, will still be required to fill a uniformly sampled aperture. This, in turn, leads to a high station cost.

With an aperiodic distribution of antennas, however, it is possible to sparsely fill the aperture, and achieve grating lobe-free operation over a wide bandwidth. For instance, in [61], an optimization approach is used to design a 100 m diameter, 256 element, aperiodic station layout, which exhibits a maximum sidelobe of -17 dB over all possible scanning directions down to the horizon and across the entire LWA operating band of 20 to 80 MHz. As mentioned in [62] and [63], however, a disadvantage of the aperiodic array is that mutual coupling interactions are randomized between different elements in the array. This causes the antenna element response at a given frequency to vary in a random fashion between different elements and wave incidence angles. This, in turn, can lead to degradations in array performance such as scan angle-dependent changes in the main beam and sidelobe level [64]. A standard approach to reduce mutual coupling in an aperiodic array is to increase the average spacing between elements. However, as mentioned before, the size of the station is limited to approximately 100 m due to the field of view requirement, which limits the amount that element spacing can be increased. An alternative approach to reducing mutual coupling, and one that is considered in the present study, is to manipulate the geometry of the antenna element.

The computation time required to evaluate the response of a large array, including antenna element effects, can limit the degree to which array performance can be optimized. Infinite array theory [65] takes advantage of the periodic nature of a uniform array in order to determine its approximate response with reduced computation time. However, this approach is not applicable to aperiodic arrays due to the lack of periodic structure. It is possible to use full-wave simulation to calculate the exact response of a finite array with an arbitrary arrangement of antenna elements and arbitrary element design. This may be reasonable for characterization of a limited number of array design variations. However, due to the large computational complexity associated with this approach, particularly for large arrays, it is not generally useful for full-scale optimization of the array. Therefore a simplified method is sought to predict antenna element effects on the response of a aperiodic array; this issue is also addressed in the present study.

In this chapter, transmit and receive-mode definitions for mutual coupling between two antennas are first presented. A design analysis is performed using simple wire inverted-V dipole antennas to determine methods for reducing receive coupling between two antennas. The responses of large uniform and aperiodic receive arrays are evaluated assuming different wire inverted-V dipole designs. From these results, it is shown that the receive coupling calculation for two antennas can be used to efficiently design antenna elements which exhibit reduced mutual coupling effects when operated in a phased array. A Pareto GA is then used to optimize broadband dipole antennas for use in the LWA in terms receive coupling, as well as sky noise frequency response and radiation pattern quality.

4.2 Mutual Coupling Between Two Antennas

Two unique definitions of mutual coupling between a pair of antennas are described in [66]. In the “transmit mode” coupling definition, an excitation source is placed at the feed of one antenna, and the other antenna is terminated in a load. Coupling between the two antennas is then calculated by

$$C_{tr} = \frac{P_L}{P_D} \tag{4.1}$$

where P_D is the power delivered (or radiated) by the excited antenna, and P_L is the power delivered to the load of the un-excited antenna. The power delivered by an antenna when an ideal voltage source, V_s, is placed at the feed, ignoring conductive losses on the antenna, is

$$P_D = \frac{V_S^2}{2}\mathbf{Re}\left\{\frac{1}{Z_{in}}\right\} \tag{4.2}$$

where Z_{in} is the input impedance of the antenna. The power delivered to an antenna load, Z_L, due to the induced current at the antenna terminal by an incident wave, I_{rec}, is

$$P_L = \frac{I_{rec}^2}{2}\mathbf{Re}\left\{Z_L\right\}. \tag{4.3}$$

This is the typical notion of coupling between a pair of antennas, which can be easily calculated by simulation or measured. When considering the interaction between antennas in a receive-only phased array, however, this definition of coupling seems problematic since the excitation is generated by a transmitting antenna at a fixed orientation relative to the other antenna. Therefore, there is no way to evaluate the change in coupling between the two antennas when they are excited by an incident wave from different directions. It is also expected that different current modes can be setup in the antennas when excited by a plane wave rather than by a source placed at the feed of one of the antennas.

An alternative, “receive mode” definition of mutual coupling between two antennas is also proposed in [66]. In this definition, excitation is provided to one antenna, but not to the other by an incident plane wave from a direction (θ, ϕ).

Both antennas are terminated in a load. Coupling between the two antennas is calculated using

$$C_{rec} = \frac{P_{L,un-ex}}{P_{L,ex}} \tag{4.4}$$

where $P_{L,ex}$ is the power delivered to the load of the excited antenna, which is due to the incident wave and scattering between the antennas while $P_{L,un-ex}$ is the power delivered to the load of the un-excited antenna which is only due to scattering between the antennas. $P_{L,ex}$ and $P_{L,un-ex}$ are defined in a manner analogous to Equation 4.3 with substitution of the proper induced currents and load impedances. This definition of coupling has the advantage that both antennas are operating in a receive mode, and that the coupling response can be evaluated for different directions of the incident field. Though it is not as straightforward to measure as transmit coupling, receive coupling can be calculated easily through simulation. For instance, using a method of moments code such as NEC, this calculation is performed by simply zeroing out those elements in the right-hand-side excitation vector corresponding to the un-excited antenna, and solving the full matrix equation to determine the currents on both antennas as usual.

A version of NEC-2, nec2++, was modified as described above to enable the calculation of receive coupling. Transmit and receive coupling calculations as defined in Equations 4.1 and 4.4 were then performed with the modified code to verify that it gave identical results as those given in [66] for short dipoles operating in free space.

An initial study is performed to determine the coupling properties of wire inverted-V dipoles operating over an infinite PEC ground. The antenna design parameters considered in this study include the antenna element length, L, the height of the antenna above the ground, H, the droop angle of the element, α, and the wire radius, r_w, as shown in Figure 4.1. For a given distance between the two antennas, d, both parallel and co-linear antenna orientations, as shown in Figure 4.2, are considered when calculating mutual coupling. The original design considered has dimensions of L = 1.77 m, H = 1.77 m, $\alpha = 45$,and $r_w = 9.5$ mm. The load impedance is assumed to be $Z_L = 100\ \Omega$.

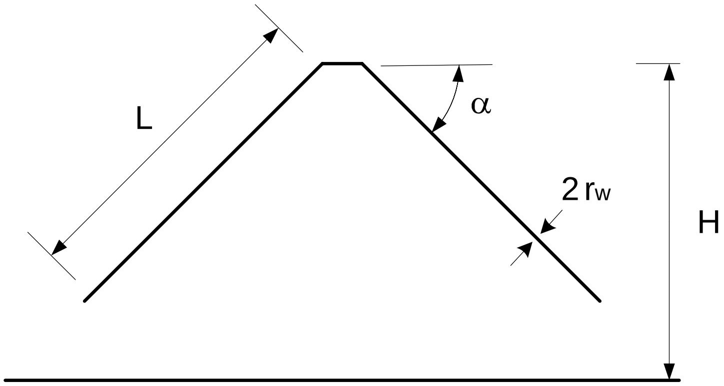

Figure 4.1: Geometry of the inverted-V wire dipole antenna.

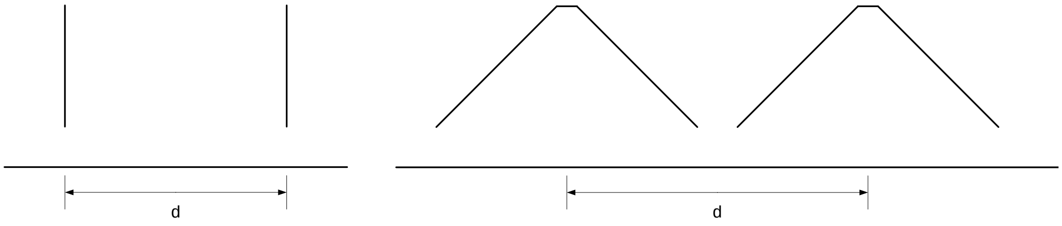

(a) (b)

Figure 4.2: Parallel dipole orientation (left), co-linear dipole orientation (right).

Assuming d = 4 m, transmit and receive coupling are calculated for the original inverted-V design for parallel and co-linear antenna orientations as a function of frequency, and the results are given in Figure 4.3. For both antenna orientations, receive coupling is calculated at incidence zenith angles, $\theta = 0^{\circ}$, 22.5°, 45°, and

67.5 ° for co-polar excitation in the E-plane of the antennas. Except for the fact that both tend to peak up near the half-wave resonance of the dipole, which in this case is near 40 MHz, transmit and receive coupling exhibit considerably different trends with frequency. Transmit coupling is much higher at low frequencies (below half-wave resonance) than receive coupling. At higher frequencies, receive coupling tends to be higher. Also, while receive coupling is similar for different incidence angles at lower frequencies, there can be significant variation with incidence angle at higher frequencies, especially for co-linear dipoles.

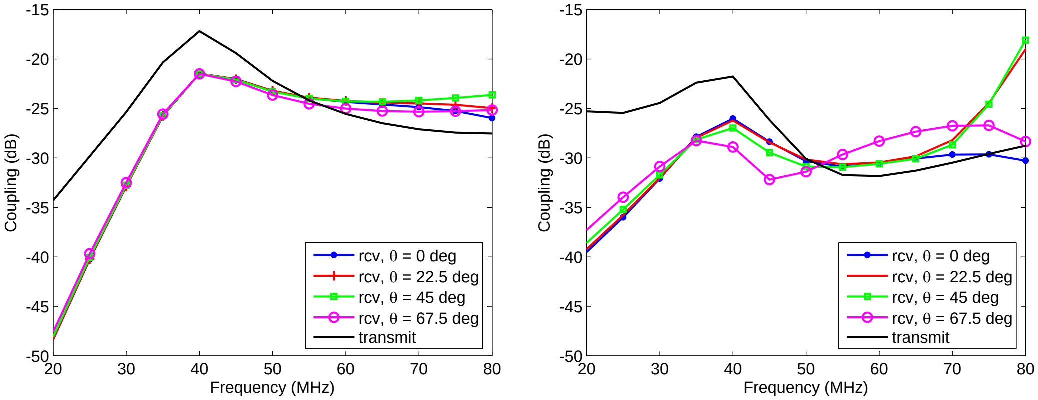

(a)

(b)

Figure 4.3: Comparison of transmit and receive coupling calculations for the original wire inverted-V dipole design. (a) Parallel dipoles, (b) co-linear dipoles.

The effect of varying antenna design parameters on receive coupling between two wire inverted-V dipoles is now considered. The goal here is to reduce coupling over all frequencies, both dipole orientations (parallel and co-linear), and all incidence angles for a fixed distance between dipoles, d = 4 m. The length of a dipole arm and the wire radius are maintained the same as the original design (L = 1.77 m, and r_w = 9.5 mm) so that the frequency coverage of the two designs are similar.

The coupling between the dipoles is evaluated for different values of the design parameters, H, α, and Z_L. While H and α are allowed to vary over a relatively wide range of values, only a limited set of values of Z_L is considered: 100 Ω, 150 Ω, 200 Ω, 300 Ω, and 400 Ω.

It is found to be rather challenging to achieve a simultaneous improvement in coupling over all frequencies, dipole orientations, and incidence angles by manual adjustment of design parameters. This is due to the fact that what parameter changes tend to reduce coupling for the parallel orientation, in many cases also tend to increase coupling for the co-linear orientation. Additionally, parameter changes which tend to reduce coupling for lower frequencies (below half-wave resonance), in many cases also tend to increase coupling for higher frequencies (above half-wave resonance.) Luckily, parameter changes which tend to reduce coupling for a given incidence angle, also tend to reduce coupling for other incidence angles for the same dipole orientation and frequency, though some exceptions to this are noted. After some trial and error, a combination of parameters, H = 1.2 m, $\alpha = 30^\circ$, and Z_L = 200 Ω, is found which exhibits reduced receive coupling for both orientations, all frequencies, and all incidence angles. The calculated receive coupling for the new inverted-V design is compared with that of original design in Figure 4.4. The new design exhibits a reduction in coupling of up to 8 dB at 40 MHz, and a reduction of better than 3 dB over all frequencies above 30 MHz for both orientations and all incidence angles.

Although receive coupling between antennas is a useful quantity for analysis, it is not straightforward to measure. In [67], an approach is given for measuring a similar quantity, the receive-mode mutual impedance between two antennas. This study, however, considers antennas operating at microwave frequencies, which makes

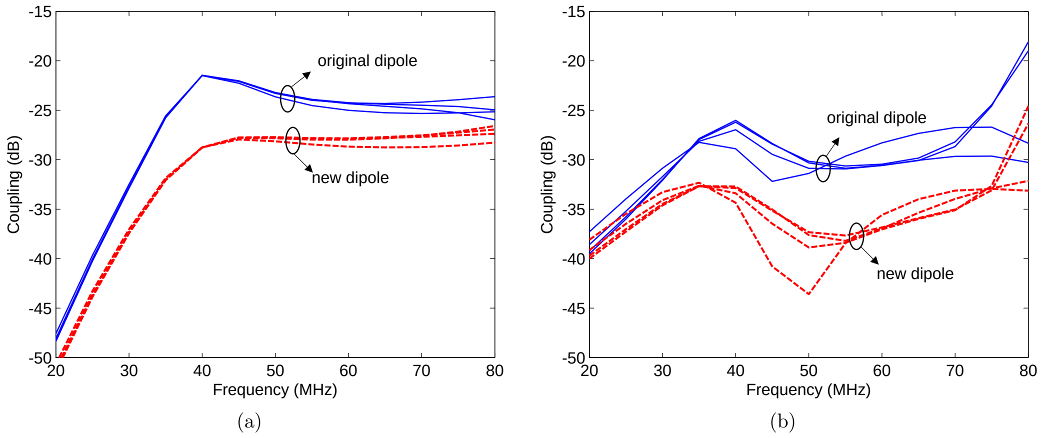

(a) (b)

Figure 4.4: Comparison of receive coupling for the original and the new wire inverted-V dipole designs. (a) Parallel dipoles, (b) co-linear dipoles. Coupling is calculated at the zenith angles [0 °, 22.5 °, 45 °, 67.5 °] for both designs.

it relatively easy to generate the far-field wave needed to excite the antennas. It is not so easy to generate a far-field excitation for antennas operating at LWA frequencies, particularly since the antennas must be operated over the ground, and it is desired to excite the antennas from any arbitrary direction. Therefore, such a measurement is not attempted in the present study. However, in order to assess the accuracy of NEC-2 simulation, measurements are made of transmit coupling between two antennas.

An alternative definition of transmit coupling is considered here and is given by

$$C'_{tr} = |S_{21}|^2 \tag{4.5}$$

where S denotes an S-parameter; this quantity is also known as the matched transducer power gain [52]. It is related to the original definition of transmit coupling, Equation 4.1, by

$$C'_{tr} = (1 - |S_{11}|^2)C_{tr}. \tag{4.6}$$

S_{21} between two antennas can be measured directly by a VNA. In the case of dipole antennas, however, it is necessary to connect a balun between each of the balanced antenna inputs and the corresponding un-balanced ports on the VNA. Since VNA calibration can be performed only up to the un-balanced inputs of the baluns, the S-parameters measured by the VNA will contain the responses of the baluns in addition to the desired response of the antenna pair. Therefore, an inversion procedure, which is described in Appendix A, is used to extract the S-parameters of the antenna pair from the measurement including the baluns. For comparison, the response of the antenna pair is also determined by simulation. First, Equation 4.1 is used to determine C_{tr}. Equation 4.6 is then used to calculate $C'_{tr} = |S_{21}|^2$; S_{11} in this equation is calculated using the simulated input impedance of the transmitting antenna when operated in the presence of the receiving antenna.

A pair of wire inverted-V dipoles were constructed for measurements, and are shown in Figure 4.5. The dimensions of the constructed antennas are similar to those of the original wire inverted-V dipole design considered earlier in this section except that a much narrower wire radius, $r_w = 2.1$ mm is used. This was done in order to make use of available 6 gauge copper bus wire. The “as-built” dimensions of the antennas and the ground parameters beneath the antennas were measured and used in simulation. Measured and simulated values for transmit coupling over the LWA frequency band for dipoles spaced at 4 m in both parallel and co-linear orientations are compared in Figure 4.6. As can be seen, the measured and simulated trends with frequency agree very well for both antenna orientations over the entire frequency range. The agreement in measured and simulated coupling values is also good, especially for the parallel dipole orientation. There is more disagreement in results for the co-linear orientation where the measured coupling is shifted up somewhat compared with simulated values over most frequencies. It was found that the depth of the null predicted by simulation for co-linear coupling near 45 MHz, where measurement and simulation agree the worst, is rather sensitive to the ground parameter values used. For instance, the agreement in results can be improved, especially near the mentioned null, by increasing the ground conductivity and permittivity values (compared with the measured values) used in simulation. This may suggest that there was some error in the original ground parameter measurements or that there is some error in the Sommerfeld ground model used in NEC-2. The "bumps" that can be seen in the measured response are likely due to scattering from buildings, which are roughly 6m to 9m away from the antennas. This could be avoided by moving the measurement setup to a more open area. Nonetheless, these results show that NEC-2 can accurately predict coupling frequency trends and estimate coupling values to within at least a few dB of measured values.

Figure 4.5: Picture of constructed wire inverted-V dipoles arranged in a parallel orientation.

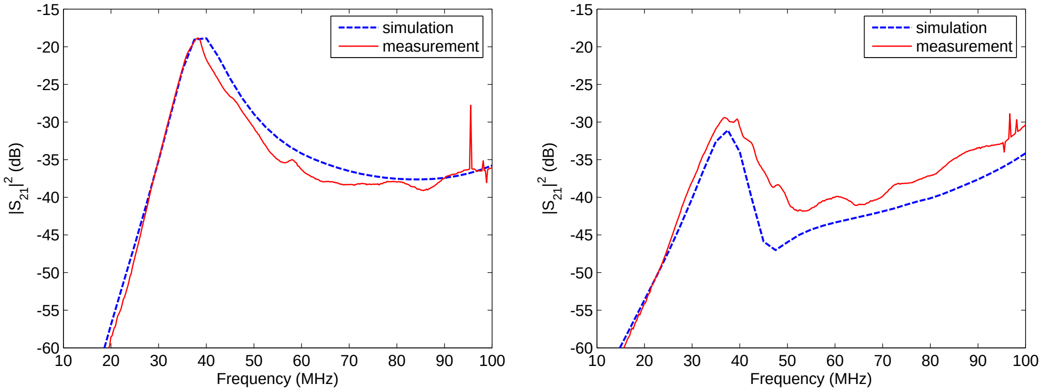

(a)

(b)

Figure 4.6: Comparison of measured and simulated transmit coupling between original inverted-V wire dipoles at 4 m spacing. (a) Parallel orientation, (b) co-linear orientation.

4.3 Phased Array Performance

4.3.1 Analysis of Array Element Terminal Currents

The effect of the antenna element design on the phased array performance is next considered. An approach for evaluating different array designs including antenna element effects using the NEC code is described in [63]. In this approach, multiple instances of a given antenna element model are generated and placed according to a specified array layout. An impedance load is placed at the terminals of each antenna in order to simulate the effect of the pre-amp. The modeled array is then excited by a plane wave incident at different directions. Note that in this case, all antennas in the array are being excited by the plane wave, which differs from the receive coupling calculation discussed in Section 4.2, in which only one of the two antennas is excited. The variation in terminal currents due to mutual coupling effects across different antenna elements in the array, and for different wave incidence directions is analyzed to determine the quality of the array design. An array which exhibits significant variation in terminal currents will, in general, be more difficult to calibrate than one which exhibits lower terminal current variation. Thus, it is desired to achieve an array design with low terminal current variation.

This approach is used to simulate the response of large arrays consisting of wire inverted-V dipole antennas. An aperiodic array layout, based on the design given in [61], is first considered. This is a circular array consisting of 256 elements with a minimum inter-element spacing of 4 m, and is optimized for low sidelobes over 20 MHz to 80 MHz. To reduce computation time, only the central-most 128 elements of this array layout are included in simulation in this study. For comparison, simulations of a uniform array are also conducted. The uniform array considered is a circular arrangement of 129 elements with an inter-element spacing of 3.6 m. Due to the geometrical symmetry exhibited throughout a uniform array, mutual coupling effects will tend to be similar between different antenna elements. This will lead to reduced terminal current variation between different elements, and thus reduced spurious behavior in the array response. As discussed previously, however, uniform arrays are susceptible to grating lobes, particularly at higher frequencies. The aperiodic and uniform array layouts are compared in Figure 4.7. Simulations of the aperiodic array are conducted using both the original and new wire inverted-V dipole designs discussed in Section 4.2. Only the original dipole design is considered in uniform array simulations. For simplicity, only a single dipole (out of a crossed dipole pair) at each antenna location is included in simulation. Additionally, only co-polar plane wave excitation of the array is considered.

The terminal current magnitudes and phases from all of the antenna elements in both the uniform and aperiodic arrays for the original dipole design, and in the

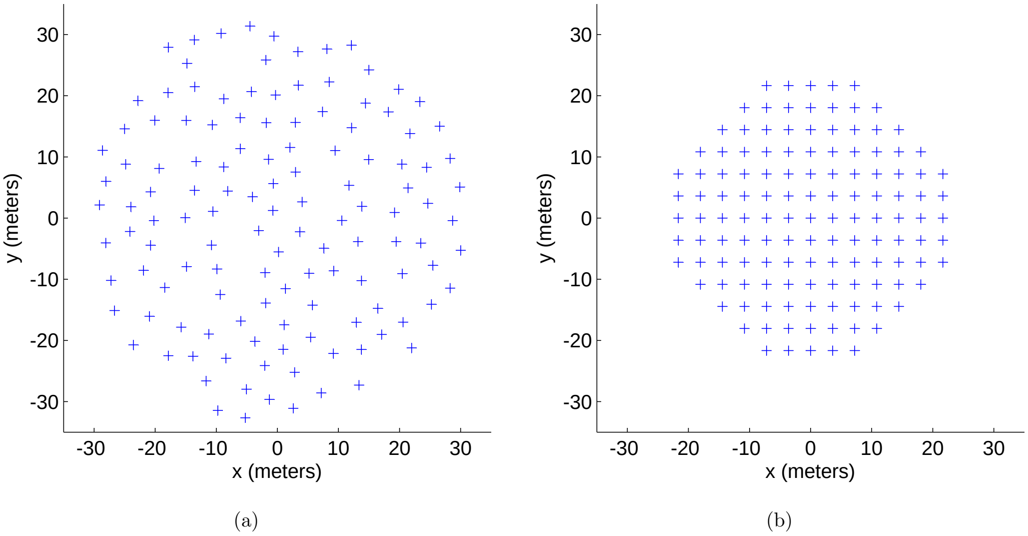

(a)

(b)

Figure 4.7: Array layouts considered. (a) Aperiodic array, (b) uniform array.

aperiodic array for the new dipole design are compared in Figures 4.8 and 4.9. Figure 4.8 provides results at 40 MHz for an incidence angle of $\theta = 0^\circ$ (boresight) and Figure 4.9 provides results at 75 MHz for $\theta = 45^\circ$ in the E-plane of the array. The geometric component of the phase due to the spacing between antennas has been removed from the phase results so that only perturbations due to mutual coupling remain. The results are sorted in ascending order as a function of distance from the center of the array. As can be seen, when the original dipole design is considered, the uniform array exhibits significantly lower variation in both terminal current magnitude and phase than the aperiodic array for both frequency / incidence angle combinations shown. However, the current variations are significantly lower for the aperiodic array for both frequency / incidence angle combinations when the new dipole design is used, as compared with the original dipole design, so that the performance is more comparable to that of the uniform array. This is consistent with the receive coupling results given in Section 4.2.

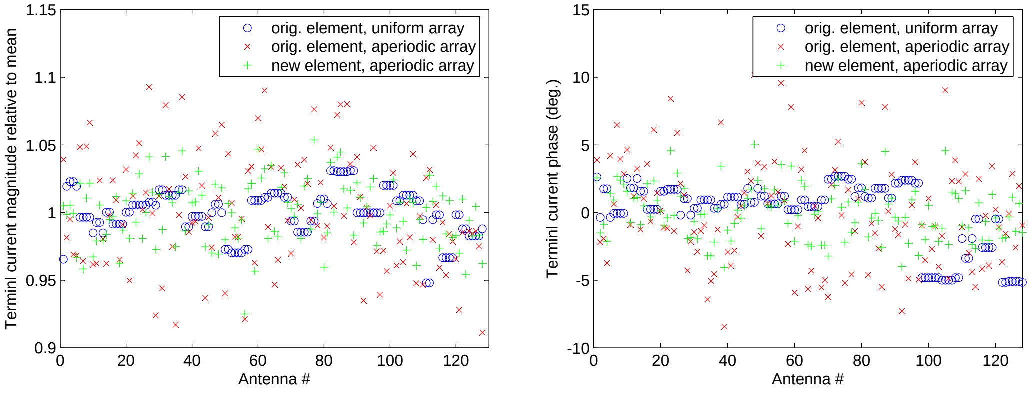

(a) (b)

Figure 4.8: Comparison of (a) terminal current magnitudes, and (b) phases for different array / antenna element combinations at 40 MHz, for co-polarized excitation at $\theta = 0^\circ$ (boresight).

In order to simplify analysis of array performance over a wide frequency range, statistics are calculated at each frequency over the terminal currents from all antennas. These include the standard deviation of current phase, and the standard deviation of current magnitude relative to the mean magnitude; it is necessary to define the magnitude statistic this way since the mean value changes at each frequency. These statistics are plotted in Figure 4.10 for all three array design / dipole design combinations in 5 MHz steps between 20 to 80 MHz for two different incidence angles, $\theta = 0^\circ$ and $\theta = 45^\circ$ in the array E-plane. Both magnitude and phase statistics are significantly better over most frequencies and incidence angles with the uniform array than with the aperiodic array when the original dipole design is used. The statistics of the aperiodic array are significantly improved (by a factor of 2 or more in some cases), however, by using the new dipole design, as compared with the original design, for all frequencies and incidence angles. This is completely

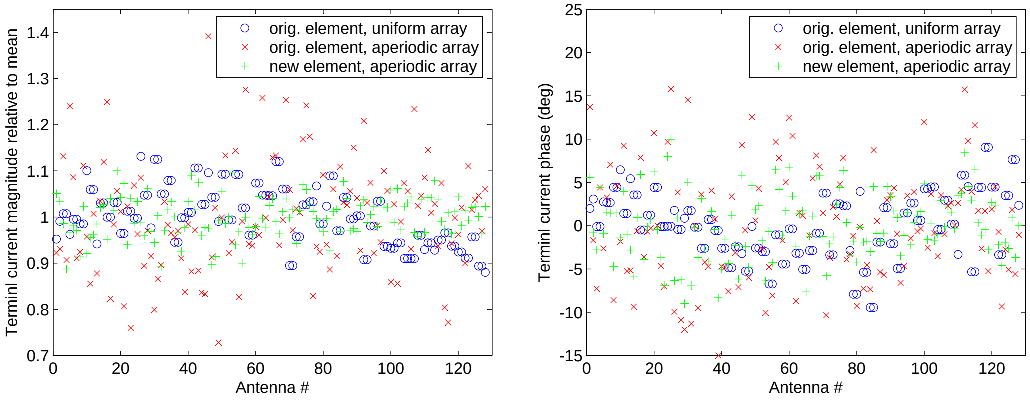

(a) (b)

Figure 4.9: Comparison of (a) terminal current magnitudes, and (b) phases for different array / antenna element combinations at 75 MHz, for co-polarized excitation at $\theta = 45^\circ$ in E-plane of array.

consistent with the receive coupling behavior of the two dipole designs described in Section 4.2. The performance of the aperiodic array with the new dipole design is, in fact, comparable to that of the uniform array over the entire frequency range. It should be noted that all array design / dipole design combinations exhibit a significant increase in both current magnitude and phase variation at the high end of the operating band for low incidence angles (higher values of θ.) This behavior is also evident in the receive coupling calculations shown in Figure 4.4, particularly for the co-linear antenna orientation. These results appear to indicate that there is a correlation between the receive coupling calculation for two antennas of a common design and the performance of a phased array when that same antenna design is used in the array.

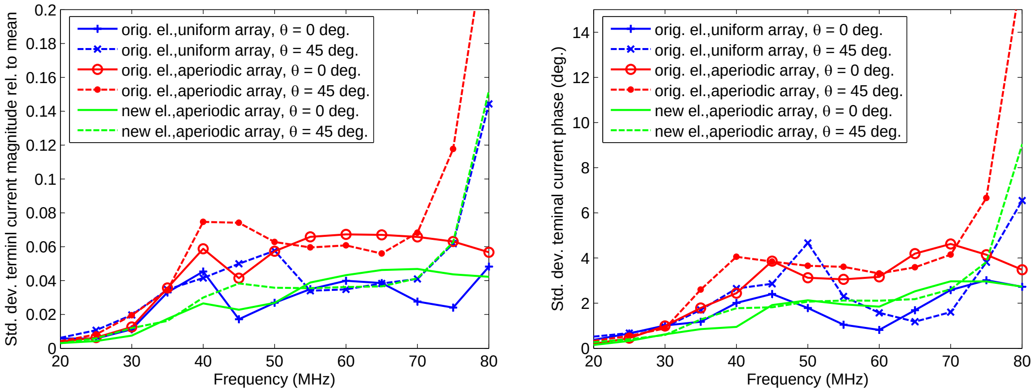

(a) (b)

Figure 4.10: Standard deviations calculated over all antennas, of (a) terminal current magnitude, and (b) phase over LWA band for different array / antenna element combinations.

4.3.2 Analysis of Beamformed Response

One way that array antenna outputs can be combined is through beamforming. To analyze mutual coupling effects on beamforming performance, it is necessary to compare the ideal beamformed response of an array, which assumes an ideal model of the array elements neglecting coupling altogether, with the actual beamformed response, which includes coupling. Any difference between the two results is assumed to be due to mutual coupling. The ideal beamformed response is calculated using

$$TF_{ideal}(\theta,\phi) = EF_{ideal}(\theta,\phi)AF_{ideal}(\theta,\phi) \tag{4.7}$$

where EF_{ideal} and AF_{ideal} are the ideal element and array factors, respectively, and (θ,ϕ) is the observation direction. In this analysis, EF_{ideal} is the receive pattern (based on terminal currents) for a single isolated antenna element determined through simulation. The ideal array factor is given by

$$AF_{ideal}(\theta,\phi) = \sum_{i=1}^{N} \alpha_i e^{jk_0(\mathbf{r'_i}\cdot\mathbf{r} - \mathbf{r'_i}\cdot\mathbf{r_0})} \tag{4.8}$$

where N is the number of array elements, α_i is the beamforming weight for element i, and $k_0 = 2\pi/\lambda_0$ where λ_0 is the observation wavelength. In Equation 4.8,

$$\mathbf{r'_i} = x_i\hat{\mathbf{a_x}} + y_i\hat{\mathbf{a_y}} + z_i\hat{\mathbf{a_z}}$$

is the coordinate vector of antenna element i,

$$\mathbf{r} = \cos\phi\sin\theta\hat{\mathbf{a_x}} + \sin\phi\sin\theta\hat{\mathbf{a_y}} + \cos\theta\hat{\mathbf{a_z}}$$

is the unit vector corresponding to the observation direction (θ,ϕ), and

$$\mathbf{r_0} = \cos\phi_0\sin\theta_0\hat{\mathbf{a_x}} + \sin\phi_0\sin\theta_0\hat{\mathbf{a_y}} + \cos\theta_0\hat{\mathbf{a_z}}$$

is the unit vector corresponding to the desired beamforming direction (θ_0,ϕ_0). To calculate the actual beamformed response, the full array is simulated. This simulation provides the receive pattern for each antenna element, $EF'_{calc,i}$. Here, the prime indicates that the simulation result contains the term $e^{jk_0\mathbf{r'_i}\cdot\mathbf{r}}$ in addition to the element response. The actual beamformed response is then given by

$$TF_{calc}(\theta,\phi) = \sum_{i=1}^{N} \alpha_i EF'_{calc,i}(\theta,\phi) e^{-jk_0\mathbf{r'_i}\cdot\mathbf{r_0}}. \tag{4.9}$$

The above expressions are used to calculate the ideal and actual beamformed responses of the 128 element aperiodic array considered in Section 4.3.1. NEC-2 is used to simulate all element and array responses. Simulations are run with both the original and new wire inverted-V dipole designs described earlier in the chapter. As in Section 4.3.1, one dipole per antenna location is included in simulation so that only reception of linearly polarized waves is considered. Unlike Section 4.3.1, however, the incident wave contains both horizontal and vertical components (which are in-phase with one another) in order to excite both the co-polar and cross-polar response of the antenna elements. The element responses EF_{ideal} and $EF'_{calc,i}$ are simulated in $0.1\,^{\circ}$ degree steps for $\theta \in [-90\,^{\circ}, 90\,^{\circ}]$ for each $\phi = 0\,^{\circ}$ (E-plane cut), $\phi = 90\,^{\circ}$ (H-plane cut), and $\phi = 45\,^{\circ}$ (diagonal cut) at 20, 40, 60, and 80 MHz. For each frequency and azimuth cut, the beamformed responses TF_{ideal} and TF_{calc} are calculated in $1.0\,^{\circ}$ steps for $\theta_0 \in [-75\,^{\circ}, 75\,^{\circ}]$. The elements are assumed to be uniformly weighted in beamforming. As examples of these calculations, the ideal and actual beamformed responses of the array, TF_{ideal} and TF_{calc}, with the original dipole design at 80 MHz are compared in Figures 4.11 and 4.12 for beamforming angles of $0\,^{\circ}$ and $70\,^{\circ}$ in the E-plane azimuth cut, respectively. Note that in these plots, both the ideal and actual responses are normalized to the peak of the ideal response. When the array is beamformed to $0\,^{\circ}$, differences in the sidelobe distributions of the ideal and actual responses, which are due to mutual coupling effects, are evident. The effects of mutual coupling on the main beam at this beamsteering angle are relatively small. At a beamsteering angle of $70\,^{\circ}$, however, changes to the main beam in terms of gain, beam pointing direction, and beamwidth are more pronounced.

To simplify analysis of results over many frequencies and incidence angles, the following four metrics are calculated from the beamformed response at each beam steering angle:

1. Error in main beam half-power beamwidth (HPBW) of TF_{calc} relative to the

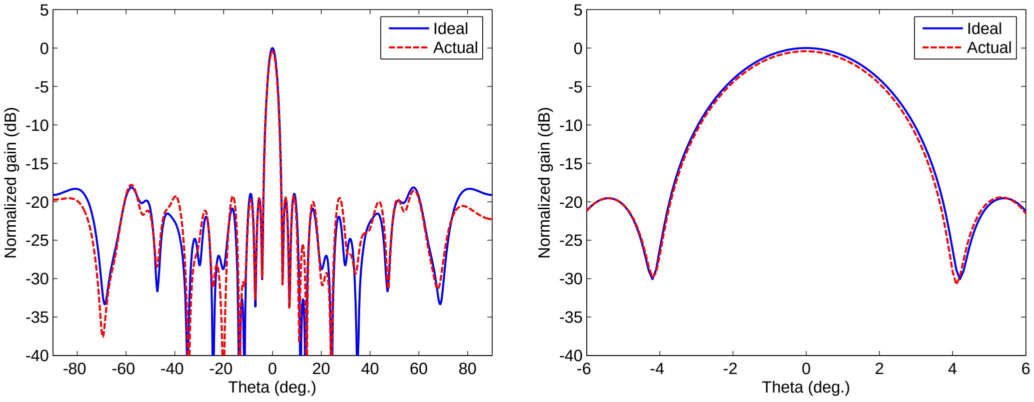

(a) (b)

Figure 4.11: Comparison of ideal and actual beamformed responses of 128 element aperiodic array using the original inverted-V wire dipole design at 80 MHz and beamformed to 0 ° relative to zenith. (a) Beamformed response over all incidence angles, (b) zoomed in on main beam. Both ideal and actual beamformed responses are normalized to the peak gain of ideal response.

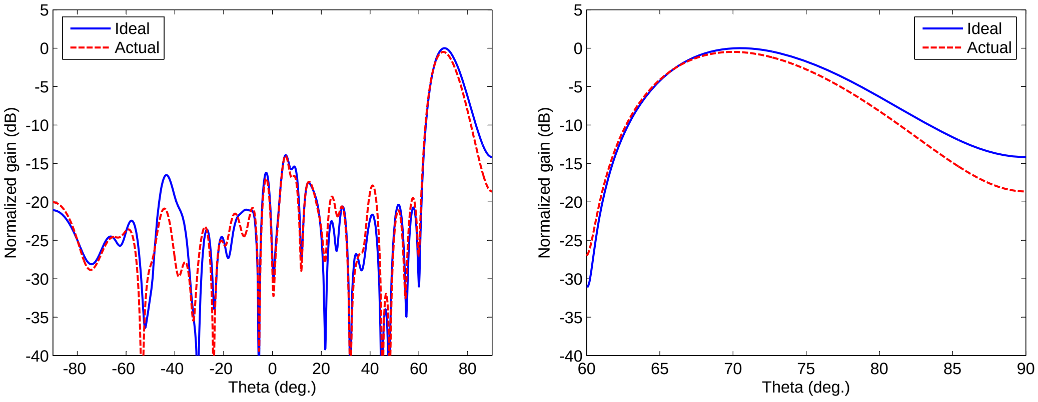

(a) (b)

Figure 4.12: Comparison of ideal and actual beamformed response of 128 element aperiodic array using the original inverted-V wire dipole design at 80 MHz and beamformed to 70 ° relative to zenith. (a) Beamformed response over all incidence angles, (b) zoomed in on main beam. Both ideal and actual beamformed responses are normalized to the peak gain of ideal response.

HPBW of TF_{ideal},

2. Error in beam pointing direction of TF_{calc} relative to the HPBW of TF_{ideal},
3. Change in maximum gain of TF_{calc} relative to maximum gain of TF_{ideal},
4. Change in peak sidelobe level (SLL) of TF_{calc} relative to peak SLL of TF_{ideal}.

The beamforming metrics at 40 and 80 MHz for the original and new dipole designs are compared in Figure 4.13. Results are only given for beam-forming in the E-plane azimuth cut as the results in the other azimuth cuts were found to be comparable. Overall, the effects of mutual coupling on array beamforming performance are relatively mild for the array and antenna element designs considered. However, in some extreme cases, the changes due to mutual coupling can be significant. For example, the main beam gain changes by up 1 dB or 26% using the original element design at 80 MHz, which could lead to some degradation in performance in a synthesis imaging application. The values of all metrics are significantly higher at 80 MHz than at 40 MHz. For most metrics, the highest values are exhibited at steering angles far from the zenith. All metrics are significantly improved in terms of both peak value and amount of variation with steering angle using the new element design as compared with using the original element design. Note that all three of these observations agree with the findings of the receive coupling and array terminal current analyses provided earlier in this chapter. Although not shown here, beamforming metrics at other frequencies also followed trends noted in receive coupling and array terminal currents.

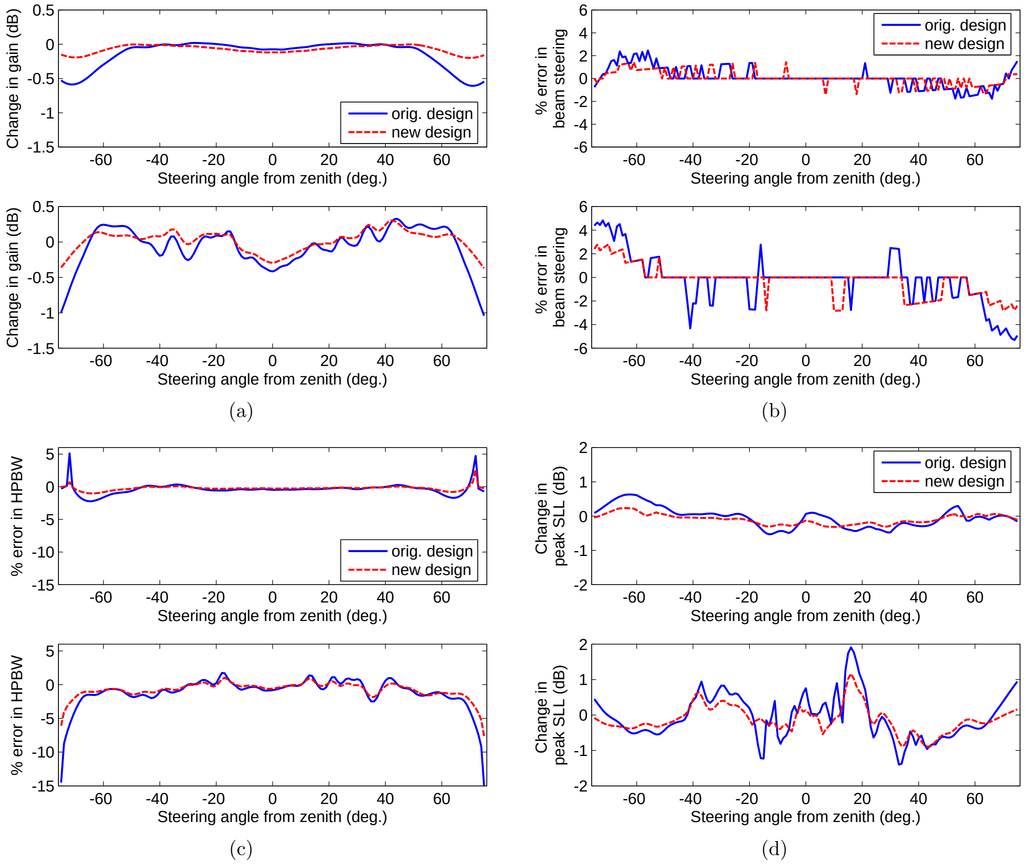

Figure 4.13: E-plane beamforming metrics for 128 element aperiodic array for both original and new wire inverted-V dipole designs. (a) Change in main beam gain, (b) error in beam pointing direction, (c) error in half-power beamwidth, and (d) change in peak sidelobe level. In each plot, top subplot provides results at 40 MHz, and bottom subplot provides results at 80 MHz.

4.4 Pareto GA Design of Array Antenna Elements Including Mutual Coupling Effects

As in Chapter 3, Pareto GA optimization is used to design antenna elements for use in the LWA. In this case, however, the effects of mutual coupling between elements when operated in a phased array are considered. This is accomplished by making use of the relationship demonstrated in Section 4.3 between the receive coupling calculation and the full array response for a given antenna element design. Since the receive coupling calculation requires modeling only two antenna elements in simulation, it is much more reasonable to execute in GA optimization than the full array calculation.

4.4.1 Pareto GA Optimization Approach

In this study, the "fork" dipole, which is a broadband element originally described in [68], is considered. As shown in Figure 4.14, the fork is essentially a drooped bow-tie dipole in which each arm consists of three radial conductors terminated by a horizontal conductor. The antenna is operated over a ground with the dipole arms oriented parallel to the ground. In [69], fork dipoles are shown to exhibit similar sky noise bandwidth as the planar dipoles considered in Chapter 3. Since a fork dipole consists of only a few relatively thin conductors, however, it should cost less monetarily to construct than an antenna made of wide pieces of sheet metal such as a planar dipole. The antenna design parameters considered in the GA are the element length, L, element droop angle, α, element flare angle, β, conductor radius, r_w, feed width, w_f, and antenna height above the ground, H, as illustrated in Figure 4.14. It was shown in Chapter 3 that antenna performance is generally improved by adding a metallic ground screen beneath the antenna. Therefore, the use of a ground screen is assumed throughout the present study. The effects of a ground screen are again approximated by an infinite PEC ground.

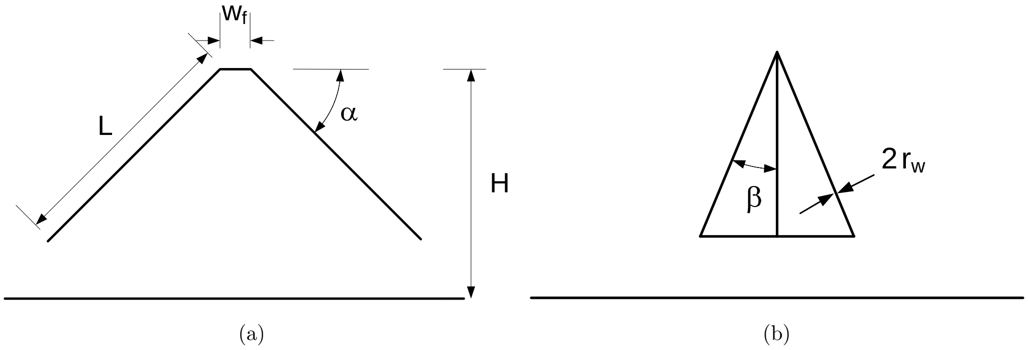

(a) (b)

Figure 4.14: Geometry of fork dipole antenna. (a) Front view, (b) side view.

Pareto GA is used to optimize fork dipole antennas in terms sky noise frequency response, radiation pattern quality, and mutual coupling. The GA formulation described in Chapter 3 is re-used here, as are the sky noise and radiation pattern cost functions, C_1 and C_2, given by Equations 3.1 and 3.8. As in Chapter 3, the sky noise response and radiation patterns are determined for a given antenna element design considering only a single, isolated dipole in the simulation. To characterize the mutual coupling performance of the element design, it is necessary to run a second set of simulations involving two identical dipoles separated by a distance, d_{el}. The GA cost function related to mutual coupling performance is

$$C_3 = \max_{all\, f,o,\theta} \{C_{rec}(f,o,\theta)\} \tag{4.10}$$

which is the maximum receive coupling, as defined in Equation 4.4, between the two dipoles over all frequencies, f, dipole orientations, o, and wave incidence angles, θ. The GA seeks to minimize the three cost functions C_1, C_2, and C_3. NEC-2 is used to perform simulations in the GA.

The GA evaluates each antenna design in 10 MHz increments between 20 MHz to 80 MHz. In evaluating C_1, a reference sky noise temperature of $T_{ref,nom}$ = 2500 K and a feed impedance of 100 Ω are assumed. $G_{ref} = \sin\theta$ is used to calculate C_2. Radiation patterns are calculated in three degree increments in both elevation and azimuth. In evaluating C_3, a nominal element spacing of $d_{el} = 4$ m is assumed. Receive coupling is calculated for wave incidence angles between $\theta = 0^\circ$ and 75° in 15° increments in the E-plane of the antennas for both parallel and co-linear dipole orientations; only co-polar wave excitation is considered. The constraints disallowing the intersection of crossed elements, and elements extending into the ground are enforced in the GA. The constraint $2L\cos\alpha + w_f < d_{el}$ is also enforced so that adjacent dipoles in the array will not overlap. Otherwise, the design parameters are allowed to vary over a relatively wide range in order to thoroughly explore available design trade-offs. The six dipole design parameters shown in Figure 4.14 are encoded in the GA using a 43 bit chromosome. A population size of N_p=500, a cross-over rate of 0.5, a mutation rate of 0.1, and a niche radius of 0.001 are used.

4.4.2 Pareto GA Results

The GA ran for 150 generations before termination, which took 73 hours to run on a single Pentium IV 2.4 GHz processor. The entire population converges to the Pareto front within 30 generations, however, and after this point, there is little further improvement in the front. Therefore, analysis here is focused on results from generation 30. The final Pareto front is shown in Figure 4.15. Note that in the figure, the mutual coupling cost function, C_3, is expressed in a log format. As can be seen, the GA has generated a set of designs that span a wide range of values for all three objectives. To simplify analysis of GA results, projections of the final front onto each of the three planes defined by pair-wise combinations of cost functions are given in Figure 4.16. Pareto ranking is performed on the final front for each pair of cost functions to generate corresponding two objective fronts, which are also shown in Figure 4.16. It is evident that a clear performance trade-off must be made between sky noise response and mutual coupling performance. All of the individuals of the projected three objective front are located relatively close to the re-ranked two objective front for this cost function pair. A trade-off must also be made between sky noise response and radiation pattern quality, which agrees with the results from Chapter 3. For this cost function pair, the projected three objective front is spread over a wider range of cost function values relative to the re-ranked two objective front. Finally, a two objective front in terms of mutual coupling performance and radiation pattern quality only exists for relatively low values of C_3, below -25. This implies that for higher values of C_3, the cost functions C_2 and C_3 are correlated, and it is not necessary to make a trade-off between these two objectives. As is evident in Figure 4.15, however, the correlation between these two cost functions is relatively weak so that many design options are available.

To determine the effect on the quality of the GA solution due to adding a third objective, the Pareto GA was re-run with only two objectives. The GA was run for both the sky noise response / mutual coupling performance and sky noise response / radiation pattern quality cost function pairs. Since these runs involved only two cost functions, a much smaller population of 60 could be used. Apart from increasing the niche radius, no other changes were made to the GA settings as described above. The final fronts from these runs are also shown in Figure 4.16. For nearly all cost function values, the sky noise / mutual coupling fronts from two objective and three objective optimizations are very similar. This indicates that the presence of a third objective did not negatively impact the performance of the GA. The two objective fronts are also similar for the sky noise / radiation pattern cost function pair. However, the front from three objective optimization lies somewhat behind the front from two objective optimization, particularly for C_1 less than 600. This implies that three objective optimization did not perform as well as two objective optimization. Given that the population of three objective optimization converged to the front relatively quickly (30 generations), it is suspected that the GA parameters could be adjusted to improve performance. In particular, increasing the population size and adjusting the niche radius should have a positive impact on performance.

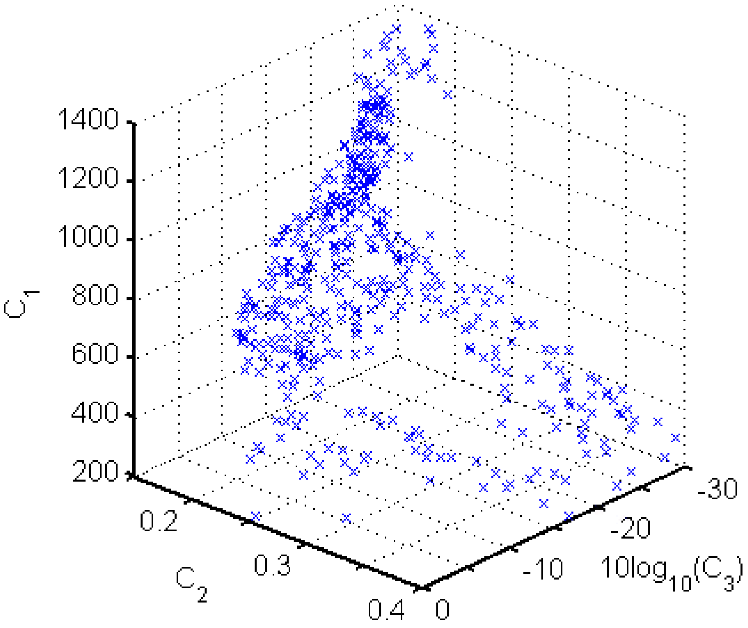

Figure 4.15: The final Pareto front generated by the GA.

One metric for selecting an antenna design from the final three objective

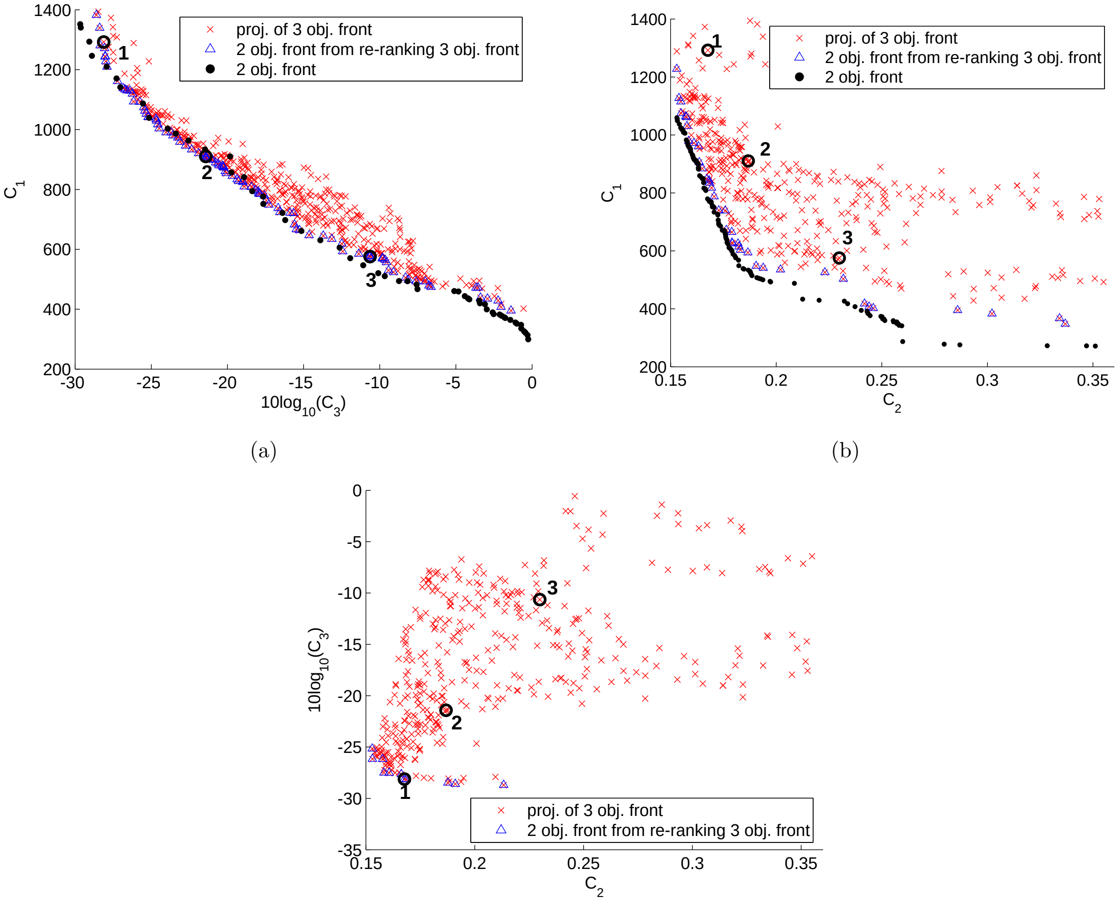

(a)

(b)

(c)

Figure 4.16: Planar projections of final Pareto front. (a) Sky noise response and mutual coupling plane, (b) sky noise response and radiation pattern quality plane, (c) mutual coupling and radiation pattern quality plane. Also included in (a) and (b) are the results from two objective optimization.

Pareto front might be that the design also resides along each of the re-ranked two objective fronts shown in Figure 4.16. Since the front for mutual coupling / radiation patterns extends over only limited cost function values, there is no individual that resides on all three two objective fronts. There are three individuals that reside on both the sky noise / mutual coupling and sky noise / radiation pattern fronts, however, the maximum receive coupling of each of these designs is very high, -2 dB or worse. It is unlikely that any design which exhibits such high mutual coupling would be desirable for use in a phased array.

Since no practical designs reside on both two objective fronts, analysis is focused instead on designs that reside on or near the sky noise / mutual coupling front. It was found necessary to sort through the designs near the two objective front in order verify that the value for the third objective (pattern quality in this case) was not exorbitantly high. Three such designs, here termed designs 1, 2, and 3, are indicated in each plot in Figure 4.16. Although, these designs are on or near the sky noise / mutual coupling front, they are all well away from the sky noise / radiation patterns front. The same behavior is noted in the sky noise / mutual coupling plane when designs are selected from the sky noise / radiation patterns front (though not shown here.) These results suggest that in general, antenna design features which lead to an optimal trade-off between two objectives will lead to sub-optimal performance in the other objective.

The sky noise responses of designs 1,2, and 3 are given in Figure 4.17. The reference sky noise profiles corresponding to 6 dB and 10 dB dominance relative to a system temperature of 250 K are also provided for comparison. As expected from Figure 4.16, design 1 exhibits the worst sky noise performance. Design 2 offers significant improvement at lower frequencies and some improvement at higher frequencies so that 6 dB dominance is achieved over most of the operating band. Sky noise reception is further improved at low frequency and above 70 MHz so that 6 dB dominance is achieved over the entire band with design 3. None of the designs achieves 10 dB dominance over the entire operating band.

The receive coupling of the three designs for both parallel and co-linear dipole orientations and wave incidence angles between $\theta = 0^\circ$ and 75° in 15° increments are given in Figure 4.18. It is evident that the peak receive coupling over all frequencies, orientations, and incidence angles of design 2 is significantly lower than design 3, as is that of design 1 compared with design 2, which is consistent with the cost function values in Figure 4.16.

The co-polarized principal plane radiation patterns at 30 MHz and 80 MHz are given in Figure 4.19. The patterns of design 1 conform better to the reference pattern at both frequencies than do those of design 2, which is expected since design 1 has a lower value of the cost function C_2 than design 2. Though the patterns of design 3 at 30 MHz are similar to those of design 1, its patterns at 80 MHz fit the reference pattern relatively poorly, exhibiting narrow E-plane beamwidth and higher sidelobes at the horizon. This causes design 3 to have the highest value of C_2 of the three designs.

Finally, the dimensions of the three GA designs are given in Table 4.1. The element perimeter, which is calculated using $p = 2L(1 + \tan^2 \beta)$, of design 2 is approximately 20% greater than design 1. This implies that design 2 will be matched better at lower frequencies than design 1. The height above ground of design 2 is also much higher than design 1, which will help matching over all frequencies. It was shown previously, however, that increased element height degrades radiation patterns and increases coupling between antennas. Both the element perimeter and height of design 3 are further increased as compared with design 2. This will further improve matching, especially at lower frequencies, but also will further degrade patterns and coupling, especially at higher frequencies. Note that these observations are consistent with the results in Figures 4.17, 4.18, and 4.19.

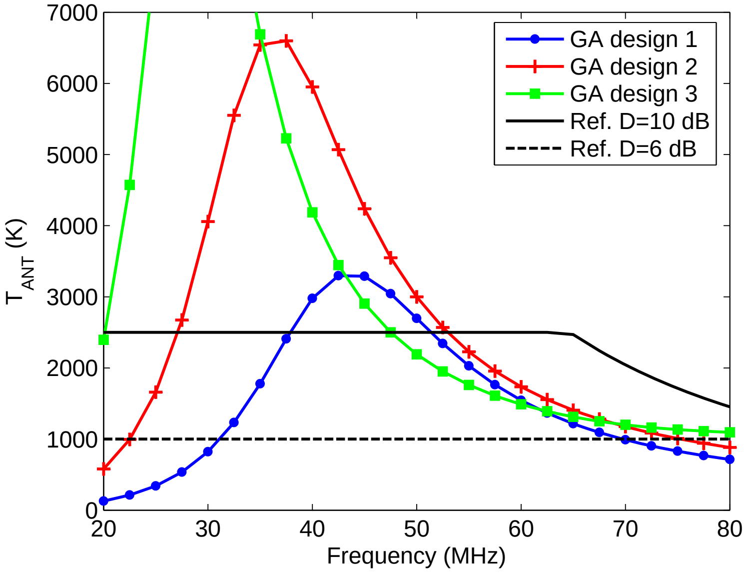

Figure 4.17: Sky noise responses for selected Pareto GA fork dipole designs.

4.4.3 Phased Array Performance of Pareto GA Fork Dipole Designs

The performances of the Pareto GA-generated fork dipole antenna designs presented in Section 4.4.2 when operated in a phased array are now studied. The array design considered here consists of the 64 most central elements of the aperiodic array depicted in Figure 4.7(a). The number of elements is reduced in order to maintain reasonable simulation run times since the fork antenna models used in simulation are considerably more complex (require more unknowns) than those of the wire dipoles

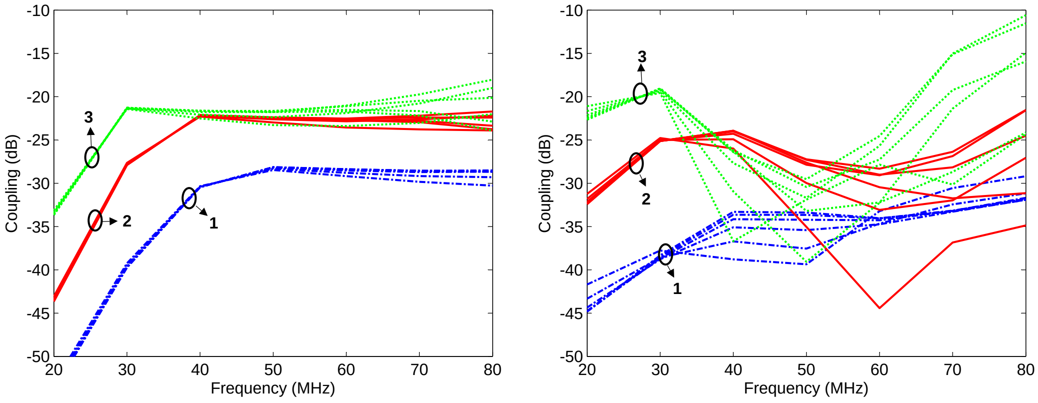

(a) (b)

Figure 4.18: Comparison of receive coupling for selected Pareto GA fork dipole designs. (a) Parallel dipoles, (b) co-linear dipoles. Coupling is calculated at the zenith angles [0 °, 15.0 °, 30.0 °, 45.0 °, 60.0 °, 75.0 °] for all designs.

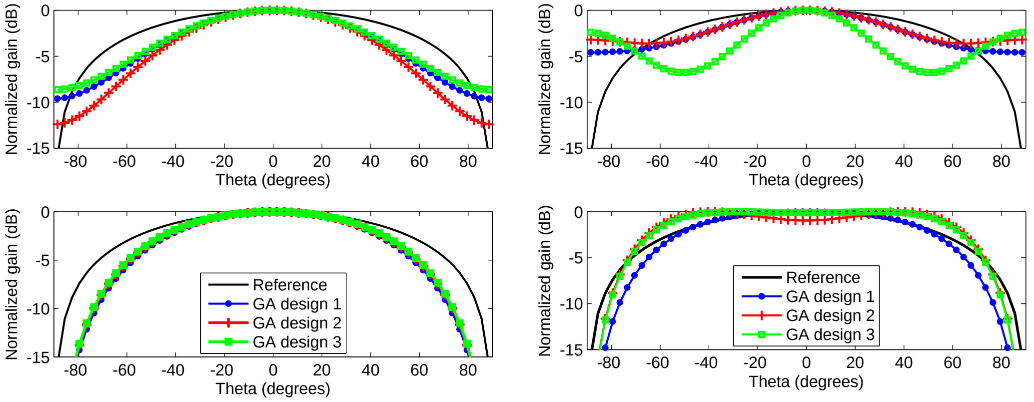

(a) (b)

Figure 4.19: Co-polarized radiation patterns for selected Pareto GA fork dipole designs at (a) 30 MHz, and (b) 80 MHz. E-plane (top), H-plane (bottom).

Table 4.1: Dimensions of selected Pareto GA designs.

	GA 1	GA 2	GA 3
$L(cm)$	101.1	111.3	175.9
$\beta(^\circ)$	31.2	38.9	17.7
$w_f(cm)$	10.0	9.3	10.0
$r_w(cm)$	0.8	1.0	1.0
$H(cm)$	120.0	166.9	180.0
$\alpha(^\circ)$	41.8	36.7	37.0

considered in Sections 4.2 and 4.3.

An analysis of array terminal currents, which follows the approach described in Section 4.3.1, is first performed. Separate simulations of the 64 element aperiodic array are conducted using each of the GA fork dipole designs, 1, 2, and 3, as the radiating element. In each case, the array is simulated between 20 and 80 MHz in 10 MHz steps, and at incidence angles between 0 and 75 ° in 15 ° steps in the antenna E-plane. The standard deviations of terminal current magnitudes and phases over the entire array are calculated at each frequency and incidence angle. The magnitude and phase standard deviations resulting from array simulations involving the three GA fork dipole designs are compared in Figure 4.20 as a function of frequency for two different incidence angles. As can be seen, the amount of terminal current variation across the array, in terms of both magnitude and phase, is greatly reduced with design 1 as compared with design 2 over all frequencies and both incidence angles. This is consistent with the results given in Figure 4.18 where the receive coupling of design 1 is much lower than design 2 over all frequencies and nearly all incidence angles. It is also evident in Figure 4.20 that array terminal current statistics are generally improved with design 2 as compared with design 3. In particular, the peak magnitude and phase standard deviation values of design 2 are much lower than those of design 3. However, there is slightly greater terminal current variation with design 2 than with design 3 between 40 and 50 MHz for one of the incidence angles. These results are also consistent with the receive coupling results in Figure 4.18.

Next, an analysis of array beamforming performance is performed following the approach described in Section 4.3.2. For each GA fork dipole design, array simulations are run at 20, 40, 60, and 80 MHz. Ideal and arrayed element responses are calculated in $0.1\,^\circ$ degree steps for $\theta \in [-90\,^\circ, 90\,^\circ]$ in the antenna E- and H-planes. The ideal and actual beamformed responses of the array are calculated in $1.0\,^\circ$ steps for $\theta_0 \in [-75\,^\circ, 75\,^\circ]$. The elements are assumed to be uniformly weighted in beamforming. As in Section 4.3.2, metrics corresponding to change in main beam gain, beamsteering error, HPBW error, and change in peak SLL are calculated from the ideal and actual beamformed responses to assess the effects of mutual coupling. The calculated metrics for E-plane steering at 40 and 80 MHz for the three GA designs are compared in Figure 4.21. At 40 MHz, the beamforming metrics for design 1 are generally improved as compared with design 2 in terms of both peak values and variation with steering angle. However, design 1 exhibits a higher peak change in gain at this frequency than design 2, though the peak values for both designs are relatively low. At 80 MHz, all of the metrics are consistently improved with design 1 as compared with design 2. In general, the metrics for design 3 are much higher than those for the other designs at both frequencies. The only exception is that designs 1 and 2 exhibit higher peak % errors in HPBW near the horizon at 40 MHz than design 3. Besides the two exceptions noted, the beamforming results for the three GA fork dipole designs are consistent with the receive coupling and array terminal current results for these designs given in Figures 4.18 and 4.20.

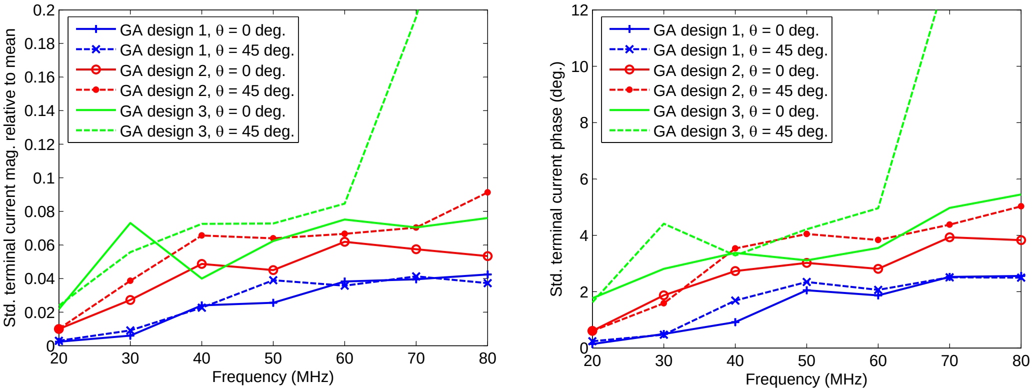

(a) (b)

Figure 4.20: Standard deviations, calculated over all antennas, of (a) terminal current magnitude, and (b) phase over LWA band for GA fork dipole designs in the 64 element aperiodic array.

4.5 Summary

The design and optimization of antennas for use in the LWA including mutual coupling effects has been considered. Transmit mode and receive mode definitions of coupling between two antennas were discussed and compared. It was shown that receive coupling can be reduced simultaneously over a wide range of frequencies, antenna orientations, and wave incidence angles by proper manipulation of the antenna element design. It was also shown that by using an element which exhibits lower receive coupling in a phased array, it is possible to reduce the amount of variation in terminal currents between different array elements and as a function of wave incidence angle. This, as was demonstrated, leads to an improvement in array beamforming performance. Since only two antenna elements are involved in the receive coupling calculation, it is much more computationally efficient than the calculation

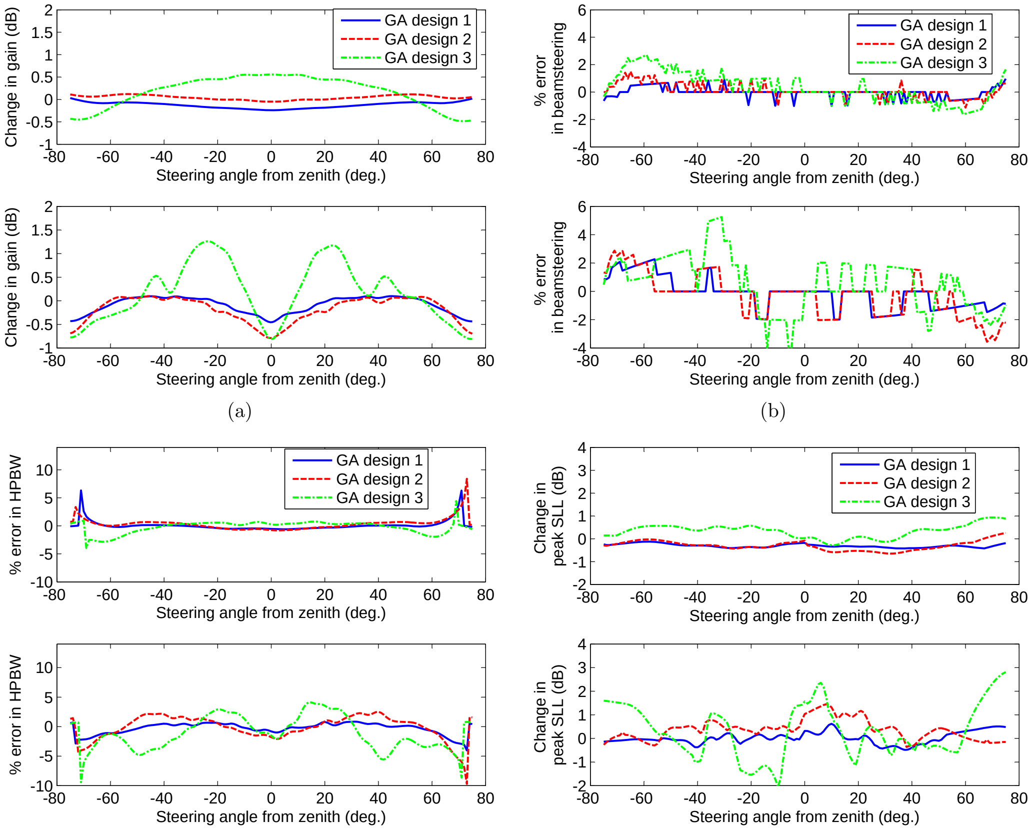

(a) (b) (c) (d)

Figure 4.21: E-plane beamforming metrics for 64 element aperiodic array with GA fork dipole designs. (a) Change in main beam gain, (b) error in beam pointing direction, (c) error in half-power beamwidth, and (d) change in peak sidelobe level. In each plot, top subplot provides results at 40 MHz, and bottom subplot provides results at 80 MHz.

of the full array response for use in designing antenna elements for low mutual coupling. This property of the receive coupling calculation was utilized in a Pareto GA approach to optimize broadband dipoles in terms of mutual coupling performance, sky noise frequency response, and radiation pattern quality. The Pareto GA generated a set of designs which spanned a wide range of values for all three objectives. It was found that performance trade-offs must be made between sky noise response and mutual coupling performance and between sky noise response and radiation pattern quality, but that mutual coupling performance and radiation pattern quality are correlated positively, though weakly. Selected designs from the final Pareto front were evaluated, and were found to offer unique performance trade-offs between the three objectives. It was verified that GA designs which exhibit reduced receive coupling cause an improvement in beamforming performance when operated in a phased array.

Chapter 5

Conclusions

This dissertation has investigated the use of multi-objective GA optimization in the design of ultra-wideband antennas for use in high-speed wireless communications and low frequency radio astronomy.

The design of ultra-wideband planar monopole antennas, which have a band-notch feature to mitigate interference with other radio systems was first considered. A GA optimizer using a scalar cost function related to both impedance matching and radiation patterns was used to improve the performance of such antennas. A matrix-based chromosome was used in the GA to describe a wide range of planar radiating element shapes. A two step optimization process was used to first optimize impedance matching in the operating and notch bands, and then optimize radiation pattern symmetry in the azimuth plane over all frequencies. As compared with previously-reported band-notched antenna designs, the GA design exhibited significantly improved notch bandwidth with attenuation levels in excess of 15 dB while maintaining ultra-wideband operation. Measurements were made of the GA design to confirm these results.

Next, Pareto GA optimization was applied to design of planar dipole antennas for use in a radio telescope array operating between 20 to 80 MHz. It was demonstrated that the GA can be used to generate a set of designs which provide a Pareto-optimal trade-off between sky noise response and radiation pattern quality. Analysis was performed on GA design geometries to determine how different design parameters affect antenna performance. Good agreement was achieved between measurements and simulations of input impedance and sky noise drift scans of selected planar dipole antennas, which validated GA results. The GA was used to study the effect that design variations such as changes in geometry constraints, feed impedance, element shape and orientation, and ground conditions have on antenna performance trade-offs.

Finally, mutual coupling effects in a low frequency radio telescope array were considered. It was shown that a receive-based coupling calculation between two identical antenna elements is related to the performance of a phased array consisting of the same antenna element. It was also demonstrated that the coupling between antennas, and thus mutual coupling effects in a phased array, can be reduced over a wide frequency range by proper adjustment of antenna element geometry. These findings were utilized to include mutual coupling, as well as sky noise response, and radiation pattern quality in Pareto GA optimization of broadband antennas for use in low frequency radio astronomy. The GA generated a Pareto optimal set of designs over a wide range of values for all three objectives. It was found that a trade-off must be made between sky noise response and radiation patterns, and sky noise response and mutual coupling; in general, no such trade-off must be made between mutual coupling and radiation patterns.

This dissertation has demonstrated that GA optimization can be applied effectively to different challenging multi-objective antenna design problems involving ultra-wide frequency bandwidths. Further research is warranted, however, in order to refine results for the applications considered here, and to apply the work to new applications. Some potential topics of future research are discussed below.

Transmit coupling measurements between wire dipoles were provided in Chapter 4, which suggest that NEC2 simulations are reasonably accurate. However, due to time limitations, no measurements were made of receive coupling between antennas, or mutual coupling effects in a receive array. Such measurements should be completed in order to fully validate the findings of Chapter 4. The principal challenge in performing both types of measurements is the need for a far-field source which can be positioned over a number of different directions in the field of view of the antennas. One possibility would be to place a transmitter on a telescoping antenna mast installed on a flatbed trailer, which can be driven to various locations around the antennas. Of course, this would be a complicated and time-consuming procedure and measurements could be performed only at source directions near the horizon. A beacon satellite could also be used as a source for these measurements. However, there is only one known frequency in the LWA band, near 29.5 MHz, at which a beacon satellite is available and still only a limited number of source directions can be tested. Therefore, the best option for performing comprehensive receive-based measurements may be to scale down the size of the antennas to operate at much higher frequencies, say between 0.5 and 1.0 GHz. In this way, it is much easier to generate a far-field source and position it in any arbitrary direction relative to the antennas under test. Furthermore, measurements can be performed in a laboratory environment.

In general, the mutual coupling performance of a phased array agrees with the receive coupling performance of the antenna element used. However, some exceptions to this were noted in the beamforming results presented in Chapter 4. There should be further study to determine how both the element design and the array layout contribute to the mutual coupling performance of the array to see if an improved approach to developing low mutual coupling elements can be developed.

It was shown that, in general, the performance of a dipole operated parallel and close to the Earth is improved by placing a metallic ground screen beneath the antenna. In all of the optimizations performed in this dissertation, the effects of a ground screen were approximated by an infinite perfect electrically conducting (PEC) ground model. In reality, however, a finite-sized ground screen is used, which changes both the radiation patterns and efficiency (mostly due to ground loss) of the antenna, as compared with assuming a PEC ground. Therefore, finite-sized ground screens should be included in the optimization. However, due to the detail required to accurately model the ground screen in simulation, this significantly increases the computational complexity of the problem. Although parallel computation was used to perform optimizations in this dissertation, further parallelization, which can be achieved by using more processors, will be required to run optimizations, which include finite-sized ground screen effects. It may be possible to reduce the complexity of the simulations somewhat by assuming a fixed-sized ground screen. This allows the portion of the Z-matrix in MOM simulation containing the ground screen to be computed prior to optimization, and for matrix partitioning to be used in solving the system [18]; both operations speed up the simulation and thus, reduce the time needed to run the optimization.

Although the application considered in this dissertation is low frequency radio astronomy, the optimization approach presented for the design of reduced mutual coupling antenna elements is equally relevant to other applications involving phased arrays. Applications that should be considered in future work include multi-input, multi-output (MIMO) wireless communications, direction finding, and radar.

The work presented here demonstrates that GA optimization is capable of finding useful solutions to complex multi-dimensional problems, owing to its global search characteristic. However, the solutions returned by GA are generally only quasi-global optimal. It has been shown that hybrid GA optimizers, which supplement a traditional GA with a local search ability, will generally improve the quality of the solution [70]. Therefore, hybrid GA optimizers should be applied to the antenna design problems considered in this dissertation, as well as any new problems considered, to determine if results can be improved.

Appendix A

S Parameter Extraction Approach to the Reduction of Dipole Antenna Measurements

Modern test equipment used for antenna measurements, such as vector network analyzers (VNA), generally provide un-balanced coaxial measurement ports. This presents a problem when performing measurements on devices such as dipole antennas, which present a balanced input. A balun must be used to interface the dipole to the VNA. Since there is no straightforward way to include the balun in the standard VNA calibration procedure, the calibration, and thus the measurement is referenced to the un-balanced input of the balun. However, it is desired to measure the antenna response at its input terminals, which are on the output side of the balun. Therefore, it is necessary to account for the balun response in VNA measurements of dipole antennas. Methods based upon scattering parameter, or S-parameter analysis are discussed here for this purpose. First the reduction of measurements from a single dipole to determine input impedance is considered. Then the reduction of measurements from a pair of dipoles to determine the coupling between them is considered.

A.1 Reduction of Dipole Antenna Input Impedance Measurement

A typical test setup used to measure the input impedance of a dipole antenna is shown in Figure A.1. A VNA is connected to the unbalanced side of a balun. The balun is assumed to have coaxial connectors on all three ports. Short adapter cables are used to connect the ports on the balanced side of the balun to the dipole radiating elements. It is assumed that these adapter cables each consist of a coaxial connector, in order to mate to the balun ports, and a short bare conductor, in order to mate to the dipole elements.

It is desired to determine the complex reflection coefficient at the antenna terminals, from which antenna input impedance can be determined. However, the VNA complex reflection coefficient measurement is referenced to the unbalanced side of the balun. In general, if the S-parameters for the cascade of components between the balun input and the antenna terminals are known, it is possible to determine the reflection coefficient at the antenna terminals, Γ_{ant}, from the VNA measured reflection coefficient, Γ_{meas}. A standard three port model for the balun is shown in Figure A.2(a) where the balun S-parameters are denoted as $\mathbf{S}''$. All ports are assumed to be referenced to a common characteristic impedance of Z_0. Analysis is greatly simplified by converting the S-parameters corresponding to the three port model, $\mathbf{S}''$, to those corresponding to an equivalent two port model, $\mathbf{S}'$, depicted in Figure A.2(b). The transform between these two models is given by [71]

$$\mathbf{S}' = \begin{bmatrix} S''_{11} & \dfrac{S''_{12} - S''_{13}}{2} \\ S''_{21} - S''_{31} & \dfrac{S''_{22} + S''_{33} - S''_{23} - S''_{32}}{2} \end{bmatrix}. \tag{A.1}$$

Note that this transform assumes that the balun exhibits perfect amplitude and phase balance between the two ports of the balanced output. Also note that in the two port model, the input side is referenced to a characteristic impedance of Z_0 while the output side is referenced to $2Z_0$.

The pair of short adapter cables between the balun and dipole terminals are modeled as a single lossless transmission line of length, L, and characteristic impedance, Z_{0k}. This model is meant to account for the phase delay due to the coaxial connectors and any coaxial cabling that make up the adapter cables. The S-parameters for a lossless transmission line are [72]

$$\mathbf{S}^* = \begin{bmatrix} \dfrac{j(\overline{Z}_{0k}^2 - 1)\sin\beta L}{2\overline{Z}_{0k}\cos\beta L + j(\overline{Z}_{0k}^2 + 1)\sin\beta L} & \dfrac{2\overline{Z}_{0k}}{2\overline{Z}_{0k}\cos\beta L + j(\overline{Z}_{0k}^2 + 1)\sin\beta L} \\ \dfrac{2\overline{Z}_{0k}}{2\overline{Z}_{0k}\cos\beta L + j(\overline{Z}_{0k}^2 + 1)\sin\beta L} & \dfrac{j(\overline{Z}_{0k}^2 - 1)\sin\beta L}{2\overline{Z}_{0k}\cos\beta L + j(\overline{Z}_{0k}^2 + 1)\sin\beta L} \end{bmatrix} \tag{A.2}$$

where $\overline{Z}_{0k} = Z_{0k}/Z_0$. It is assumed that $\beta = 2\pi/\lambda_0$ where λ_0 is the free space wavelength of the operating frequency. There may be some reactance due to the unshielded ends of the adapter cables which interface to the dipole elements. However, this reactance is assumed to be small and is ignored here.

An S-parameter model for the combination of balun and adapter cables is shown in Figure A.3. To determine the response of the combination of the balun and adapter cables, it is necessary to convert the S-parameters of each component, $\mathbf{S}'$ and $\mathbf{S}^*$, to their corresponding scattering transfer parameters, or T-parameters, $\mathbf{T}'$ and $\mathbf{T}^*$ as described in [73]. The cascaded response is then given by

$$\mathbf{T} = \mathbf{T}'\mathbf{T}^*. \tag{A.3}$$

This result is then converted to the corresponding S-parameters, $\mathbf{S}$. The reflection coefficient at the antenna terminals can be determined using [52]

$$\Gamma_{ant} = \frac{S_{11} - \Gamma_{meas}}{S_{11}S_{22} - S_{22}\Gamma_{meas} - S_{12}S_{21}}. \tag{A.4}$$

Finally, the desired antenna input impedance is given by

$$Z_{ant} = 2Z_0 \frac{1 + \Gamma_{ant}}{1 - \Gamma_{ant}}. \tag{A.5}$$

The above procedure is now applied to the reduction of impedance measurements of an inverted-V wire dipole antenna. The antenna considered has a total length of roughly 3.6 m, with elements made of wire 4 mm in diameter and which are drooped down by 45 °. The antenna is operated directly over an Earth ground. The characteristic impedance of all VNA measurements is $Z_0 = 50\Omega$. The full three-port S-parameters of the balun, $\mathbf{S}''$, are first measured. The electrical length of the adapter cable coaxial connectors are then measured. This is accomplished by soldering two such connectors back to back, and measuring the electrical delay of the connector pair, τ, using a VNA. The electrical length of one connector is then $L_c = \tau c/2$ where c is the speed of light. In Equation A.2, it is assumed that $L = L_c$ and $Z_{0k} = 2Z_0$. The antenna impedance determined by accounting for both the balun and adapter cables using the reduction procedure described in this section, by accounting for the balun but not the adapter cables (setting L=0 in Equation A.2), and by accounting for neither the balun or adapter cables (replacing Γ_{ant} with Γ_{meas} in Equation A.5) are compared in Figure A.4. The result from NEC2 simulation is also included for reference. As can be seen, when the effects of the balun and adapter cables are ignored in measurement data reduction, the measured impedance bears no resemblance to the simulated impedance. By properly accounting for the balun in data reduction, the measured impedance exhibits similar characteristics as the simulated impedance. In this case, however, the measured resistance peak is shifted down in frequency significantly, by roughly 14%, and is narrower as compared with the same feature in simulation. When the effects of both the balun and adapter cables are included in data reduction, the measured and simulated impedances agree reasonably well over the entire frequency range.

It is evident in Figure A.4 that the resistance peak in the final reduced measurement is still shifted down by about 5.5% compared with simulation. Some of this disagreement is likely due in part to not modeling in simulation the supporting structure of the constructed dipole, which includes the mast made out of four inch diameter PVC tube. Previous measurements have suggested that this mast could shift the peak resistance down in frequency by 2%. The other most likely causes of discrepancy are not accounting for all of the delay in the adapter cables, and simulation error.

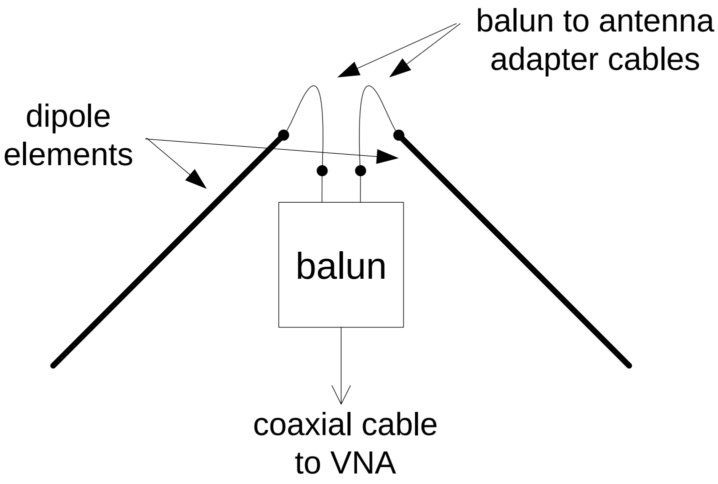

Figure A.1: Test setup for measurement of dipole antenna input impedance.

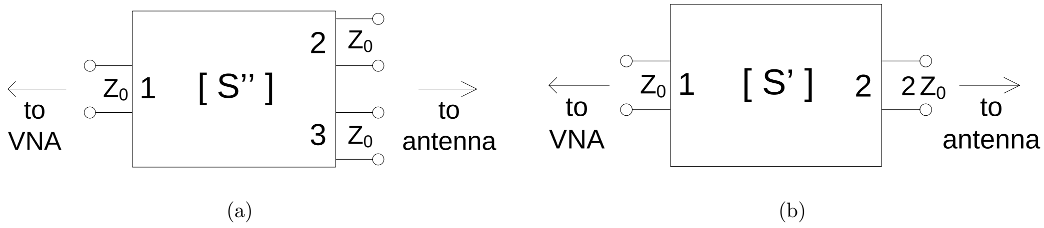

Figure A.2: S parameter models for balun. (a) Three port model, (b) equivalent two port model.

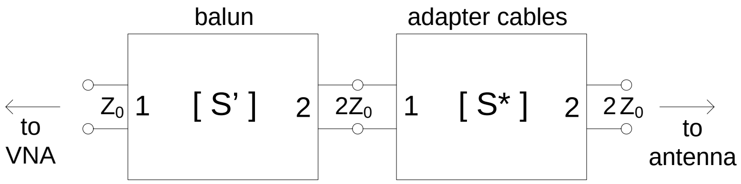

Figure A.3: S parameter model for the combination of balun and adapter cables.

A.2 Reduction of Coupling Measurements Between Dipole Antennas

A typical test setup used to measure coupling between two dipole antennas is shown in Figure A.5. Each antenna is connected through a balun to a measurement port of the VNA, which is used to measure the S-parameters of the antenna pair. Note that, as discussed in Section A.1, short adapter cables are used to interface each balun with its corresponding dipole. The effects of the adapter cables are ignored initially in this development for simplicity, but will be addressed later in this section. A simple analytical model for the test setup in Figure A.5 is shown in Figure A.6. The baluns are modeled as two port devices with S-parameters $\mathbf{S_A}$ and $\mathbf{S_C}$, which are calculated from the measured three port S-parameters of each balun using Equation A.1. The combination of the two antennas and the propagation channel between

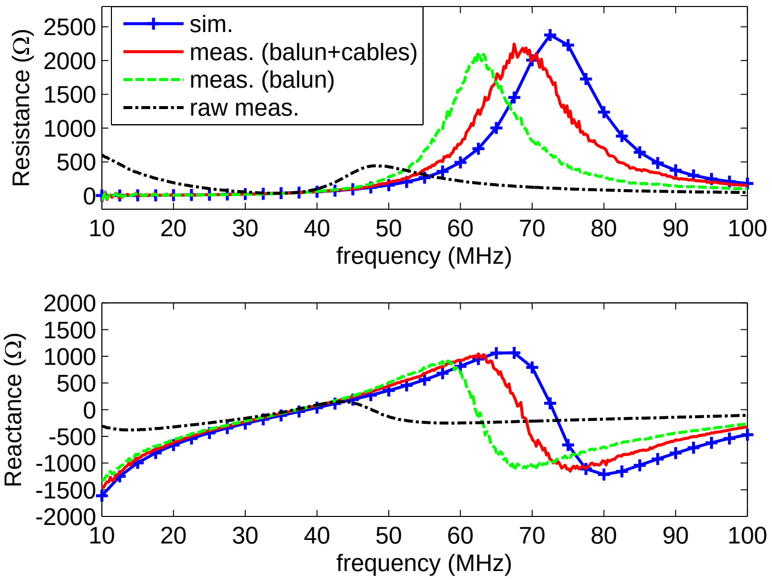

Figure A.4: Comparison of measurement and simulation of the input impedance of a wire inverted-V dipole antenna. ‘meas. (balun+cables)’ is the measurement result when the effects of both the balun and adapter cables are taken into account. ‘meas. (balun)’ is the measurement result when the effects of only the balun are taken into account. ‘raw meas.’ is the measurement result when the effects of neither the balun or adapter cables are taken into account.

them, here termed the antenna pair, is also modeled as a two port device with S-parameters, $\mathbf{S_B}$. The desired coupling between antennas is defined here as

$$C = |S_{B,21}|^2. \tag{A.6}$$

However, the S-parameters measured by the VNA, $\mathbf{S_m}$, are due to the cascade of the two baluns and the antenna pair.

To extract the desired coupling between antennas, it is first necessary to convert the S-parameters $\mathbf{S_m}$, $\mathbf{S_A}$, $\mathbf{S_B}$, and $\mathbf{S_C}$ to their corresponding T-parameters $\mathbf{T_m}$, $\mathbf{T_A}$, $\mathbf{T_B}$, and $\mathbf{T_C}$. The T-parameters are related by the following expression

$$\mathbf{T_m} = \mathbf{T_A}\mathbf{T_B}\mathbf{T_C} \tag{A.7}$$

which may be expressed explicitly in terms of matrix components as

$$\begin{bmatrix} T_{m,11} & T_{m,12} \\ T_{m,21} & T_{m,22} \end{bmatrix} = \begin{bmatrix} T_{A,11} & T_{A,12} \\ T_{A,21} & T_{A,22} \end{bmatrix} \begin{bmatrix} T_{B,11} & T_{B,12} \\ T_{B,21} & T_{B,22} \end{bmatrix} \begin{bmatrix} T_{C,11} & T_{C,12} \\ T_{C,21} & T_{C,22} \end{bmatrix}. \tag{A.8}$$

Equation A.8 can be rewritten as a system of equations of the form

$$\mathbf{Ax} = \mathbf{b} \tag{A.9}$$

where

$$\mathbf{A} = \begin{bmatrix} T_{A,11}T_{C,11} & T_{A,11}T_{C,21} & T_{A,12}T_{C,11} & T_{A,12}T_{C,21} \\ T_{A,11}T_{C,12} & T_{A,11}T_{C,22} & T_{A,12}T_{C,12} & T_{A,12}T_{C,22} \\ T_{A,21}T_{C,11} & T_{A,21}T_{C,21} & T_{A,22}T_{C,11} & T_{A,22}T_{C,21} \\ T_{A,21}T_{C,12} & T_{A,21}T_{C,22} & T_{A,22}T_{C,12} & T_{A,22}T_{C,22} \end{bmatrix}, \tag{A.10}$$

$$\mathbf{b} = \begin{bmatrix} T_{m,11} & T_{m,12} & T_{m,21} & T_{m,22} \end{bmatrix}^T, \tag{A.11}$$

$$\mathbf{x} = \begin{bmatrix} T_{B,11} & T_{B,12} & T_{B,21} & T_{B,22} \end{bmatrix}^T, \tag{A.12}$$

and the T superscript denotes a vector transpose. Note that the components of $\mathbf{x}$ are the T-parameters of the antenna pair, which are determined by solving the system of equations A.9 using

$$\mathbf{x} = \mathbf{A}^{-1}\mathbf{b} \tag{A.13}$$

where $^{-1}$ denotes matrix inversion. The T-parameters, $\mathbf{T_B}$, of the dipole pair are then converted back to the S-parameters, $\mathbf{S_B}$, and the coupling between dipoles is calculated using Equation A.6.

If the phase component of the antenna pair response is of interest, for instance, in order to determine the mutual impedance between the antennas, it may be necessary to include the effects of the adapter cables between the baluns and antennas in the above development. This can be done by simply inserting terms in Equation A.7 between $\mathbf{T_A}$ and $\mathbf{T_B}$ and between $\mathbf{T_B}$ and $\mathbf{T_C}$ corresponding to lossless transmission line models of the adapter cables, as discussed in Section A.1. Other than re-writing the matrix $\mathbf{A}$ in order to include these terms, the rest of the development follows as described above.

The above procedure is now applied to the reduction of coupling measurements between a pair of inverted-V wire dipole antennas. The antennas considered each have a total length of roughly 3.6 m, with elements made of wire 4 mm in diameter and which are drooped down by 45 °. The antennas are placed 4 m apart, and are oriented to be parallel with one another. The antennas are operated directly over an Earth ground. The characteristic impedance of all VNA measurements is Z_0

= 50Ω. The full three port S-parameters of the two baluns are first measured and converted to their two port equivalents, $\mathbf{S_A}$ and $\mathbf{S_C}$. Then the S-parameters of the antenna pair, $\mathbf{S_m}$, are measured. The antenna coupling determined by accounting for the baluns as described above, and by not accounting for the baluns (replacing $\mathbf{S_B}$ with $\mathbf{S_m}$ in Equation A.6) are compared in Figure A.7. The result from NEC2 simulation is also included for reference. As can be seen, when the baluns are not included in measurement data reduction, the measured coupling has a similar frequency response as simulation. However, the measured coupling is shifted down in amplitude as compared with simulation by up to 3 dB, which is due to not accounting for the mismatch and insertion losses of the baluns. When the effects of the baluns are taken into account, the measured and simulated coupling agree much better over the entire frequency range. The remaining discrepancies between the two results are believed to be due to scattering effects from near-by buildings in the measurement, and to simulation error.

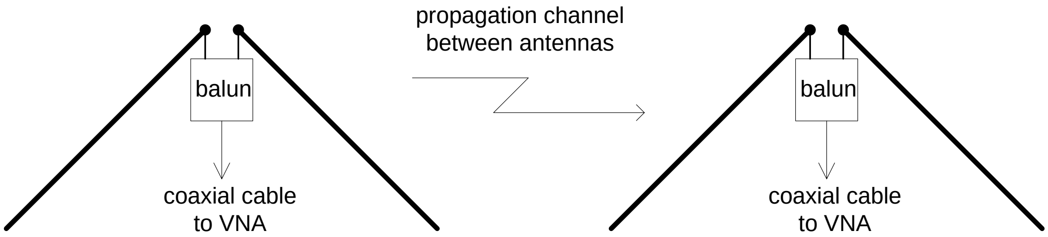

Figure A.5: Test setup for measurement of coupling between two dipole antennas.

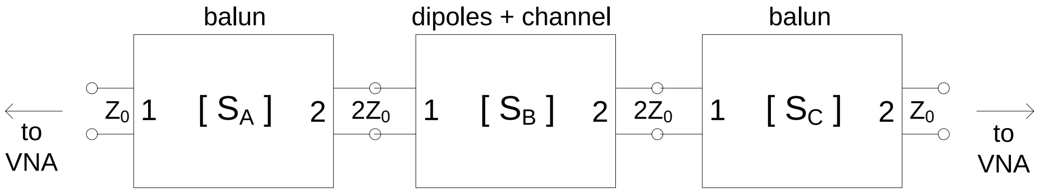

Figure A.6: S parameter model for dipole coupling test setup.

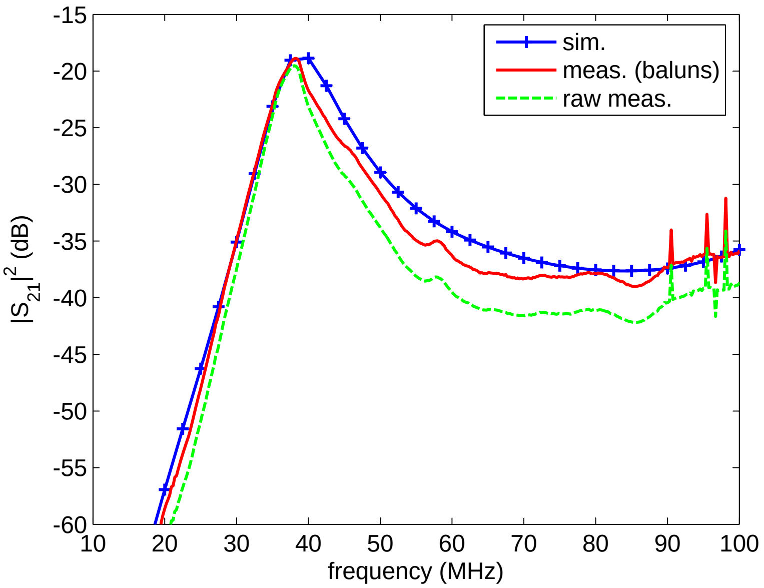

Figure A.7: Comparison of measurement and simulation of coupling between two wire inverted-V dipoles oriented parallel to one another. 'meas. (baluns)' is the measurement result when the effects of the baluns are taken into account. 'raw meas.' is the measurement result when the effects of the baluns are not taken into account.

Bibliography

[1] P.R. Foster, "Ultra-Wideband Antenna Technology, Part 2," *from Introduction to Ultra-Wideband Radar Systems, ed. J.D. Taylor*. Boca Raton, FL: CRC Press, 1995.

[2] R. Vickers, V. Gonzalez, R. Ficklin, "Results from a VHF impulse synthetic aperture radar," *in Proc. SPIE*, Vol. 1631, Los Angeles CA, Jan. 1992, p. 219-225.

[3] Anon., *Federal Communications Commission, First Report and Order, Revision of Part 15 of the Commissions Rules Regarding Ultra-Wideband Transmission Systems, FCC 02-48*, April 22, 2002.

[4] N. Leavitt, "For Wireless USB, the Future Starts Now," *Computer*, Vol. 40, pp. 14-16, July, 2007.

[5] G. Taylor, et al., "LWA Overview," *LWA Memo 56*, Sep. 22, 2006.

[6] A. Gunst, K. van der Schaaf and M.J. Bentum, "Core Station 1 - The first LOFAR station," *in SPS-DARTS 2006, The second annual IEEE BENELUX/DSP Valley Signal Processing Symposium*, Antwerp, Belgium, March 2006.

[7] T. Clarke, "Scientific Requirements for the Long Wavelength Array, Ver. 2.3," *LWA Memo 117*, Nov. 19, 2007.

[8] C.E. Baum, E.G. Farr, "Impulse radiating antennas", *in Ultra-Wideband, Short-Pulse Electromagnetics edited by H.L. Bertoni, L. Carin, L.B. Felsen.* New York: Plenum Press, 1993.

[9] R. Olsson, P-S. Kildal, S. Weinreb, "The eleven antenna: a compact low-profile decade bandwidth dual polarized feed for reflector antennas," *IEEE Trans. Antennas Propag.*, Vol. 54, pp. 368-375, Feb. 2006.

[10] K.M. Pasala, E.M. Friel, "Mutual coupling effects and their reduction in wideband direction of arrival estimation," *IEEE Trans. Aerospace and Electronics Sys.*, Vol. 30, pp. 1116-1122, Oct., 1994.

[11] H. Steyskal, J. Ramprecht, H. Holter, "Spiral element for wide-band phased arrays," *in IEEE AP/S Int. Symp. Dig.*, vol. 4, Monterey, CA, June 2004, pp. 3976-3979.

[12] Z. Chen, M. Ammann, X. Qinq, X. Wu, T. See, A. Cai, "Planar antennas," *IEEE Microwave Magazine*, Vol. 7, pp. 63-73, Dec. 2006.

[13] D. Uduwawala, M. Norgen, "An investigation of some geometrical shapes and selection of shielding and lumped resistors of planar dipole antennas for GPR applications using FDTD," *IEEE Trans. Geoscience and Remote Sensing*, Vol. 44, pp. 3555-3562, Dec. 2006.

[14] A. Kerkhoff and S. Ellingson, "A wideband planar dipole antenna for use in the Long Wavelength Demonstrator Array (LWDA)," *in IEEE AP/S Int. Symp. Dig.*, vol 1B, Washington D.C., July 2005, pp. 553-556.

[15] Information about the Murchison Widefield Array (MWA) is available at: http://www.haystack.mit.edu/ast/arrays/mwa/index.html .

[16] Y. Rahmat-Samii and E. Michielssen, *Electromagnetic Optimization by Genetic Algorithms*. New York: Wiley, 1999.

[17] E. Altshuler, D. Linden, "Wire-antenna designs using genetic algorithms," *IEEE Antennas Propag. Mag.*, Vol. 39, pp. 33-43, April, 1997.

[18] J. Johnson, Y. Rahmat-Samii, "Genetic algorithms and method of moments (GA/MOM) for the design of integrated antennas," *IEEE Trans. Antennas Propag.*, Vol. 47, pp. 1606-1614, Oct., 1999.

[19] E. Jones, W. Joines, "Design of Yagi-Uda antennas using genetic algorithms," *IEEE Trans. Antennas Propag.*, Vol. 45, pp. 1386-1392, Sept., 1997.

[20] R. Haupt, "Thinned arrays using genetic algorithms," *IEEE Trans. Antennas Propag.*, Vol. 42, pp. 993-999, July, 1994.

[21] E. Altshuler, "Design of a vehicular antenna for GPS/IRIDIUM using a genetic algorithm," *IEEE Antennas Propag. Mag.*, Vol. 48, pp. 968-972, June, 2000.

[22] D. Weile, E. Michielssen and D. Goldberg, "Genetic algorithm design of Pareto optimal broadband microwave absorbers," *IEEE Trans. Electromag. Compat.*, vol. 38, pp. 518-525, Aug. 1996.

[23] D. Weile, E. Michielssen, "Integer coded Pareto genetic algorithm design of constrained antenna arrays," *Electronics Letters*, vol. 32, pp. 1744-1745, Sept. 1996.

[24] H. Choo, R.L. Rogers and H. Ling, "Design of electrically small wire antennas using a Pareto genetic algorithm," *IEEE Trans. Antennas Propag.*, vol. 53, pp. 1038-1046, March 2005.

[25] M. Hammond, P. Poey, and F. Colombel, "Matching the input impedance of a broadband disc monopole," *Electronics Letters*, vol. 29, no. 4, pp. 406-407, 1993.

[26] N. Agrawall, G. Kumar, and K. Ray, “Wide-band planar monopole antennas,” *IEEE Trans. Antennas Propag.*, vol. 46, pp. 294-295, Feb. 1998.

[27] M. Ammann, “Square planar monopole antenna,” *in IEE National Conf. Antennas Propag.*, March 1999, pp. 37-40.

[28] A. Kerkhoff, and H. Ling.,“Design of a planar monopole antenna for use with ultra-wideband (UWB) having a band-notched characteristic,” *in IEEE AP/S Int. Symp. Dig.*, vol. 1, Columbus, OH, June 2003, pp. 830-833.

[29] H. Schantz, G.Wolenec, and E. Myszka, “Frequency notched uwb antennas,” *in Proc. IEEE Conf. Ultra Wideband Systems Technologies*, Nov. 2003, pp. 214-218.

[30] A. Kerkhoff and H. Ling, “A parametric study of band-notched UWB planar monopole antennas,” *in IEEE AP/S Int. Symp. Dig.*, vol. 2, Monterey, CA, June 2004, pp. 1768-1771.

[31] Y. Kim, D. Kwon, “CPW-fed planar ultra wideband antenna having a frequency band notch function,” *Electronics Letters*, vol. 40, no. 7, pp. 403-405, 2004.

[32] J. Qiu, Z. Du, J. Lu, K. Gong, “A band-notched UWB antenna,” *Microwave and Optical Tech. Letters*, vol. 45, no. 2, pp. 152-154, 2005.

[33] W.Lee, W. Lim, J. Yu, “Multiple band-notched planar monopole antenna for multiband wireless system,” *IEEE Microwave and Wireless Component Letters*, vol. 15, pp.576-578, Sept. 2005.

[34] A. Boag, E. Michielssen, R. Mittra, “Design of electrically loaded wire antennas using genetic algorithms,” *IEEE Trans. Antennas Propag.*, vol. 44, pp. 687-695, May 1996.

[35] S. Rogers, C. Butler, A. Martin, “Design and realization of GA-optimized wire monopoles and matching network with 20:1 bandwidth,” *IEEE Trans. Antennas Propag.*, vol. 51, pp. 493-502, March 2003.

[36] Y. Noh, Y. Kim and H. Ling, “A broadband on-glass antenna with a mesh-grid structure for automobiles,” *Electronics Letters*, vol. 41, pp. 1148-1149, Oct. 2005.

[37] A. Kerkhoff, R. Rogers, and H. Ling, “Design and analysis of planar monopole antennas using a genetic algorithm approach,” *IEEE Trans. Antennas Propag.*, vol. 52, pp. 2709-2718, Oct.2004.

[38] J. Kim, T. Yoon, J. Kim, J. Choi, “Design of an ultra wide-band printed monopole antenna using FDTD and genetic algorithm,” *IEEE Microwave Wireless Component Letters*, vol. 15, pp.395-397, June 2005.

[39] B. Kolundzija, J. Ognjanovic, T. Sarkar, *WIPL-D: Electromagnetic Modeling of Composite Metallic and Dielectric Structures, Software and Users Manual.* Boston: Artech House, 2000.

[40] *NEC-Win Pro Users Manual*, Nittany Scientific, Inc., Riverton, UT, 1997, p. 3-33.

[41] D. E. Goldberg, *Genetic Algorithms in Search, Optimization and Machine Learning.* Reading, MA: Addison-Wesley, 1989.

[42] N. Srinivas and K. Deb, “Multiobjective optimization using nondominated sorting in genetic algorithms,” *Evolutionary Computat.*, vol. 2, no.3, pp. 221-248, 1995.

[43] Y. Kuwahara, “Multiobjective optimization design of Yagi-Uda antenna,” *IEEE Trans. Antennas Propag.*, vol. 53, pp. 1984-1992, June 2005.

[44] S. Cui, A. Mohan and D. Weile, “Pareto optimal design of absorbers using a parallel elitist nondominated sorting genetic algorithm and the finite element-boundary integral method,” *IEEE Trans. Antennas Propag.*, vol. 53, pp. 2099-2107, June 2005.

[45] L. Trintinalia and H. Ling, “First order triangular patch basis functions for electromagnetic scattering,” *J. of Electromagn. Waves and Appl.*, vol. 15, pp. 1521-1537, Nov. 2001.

[46] G. Burke, A. Poggio, *Numerical Electromagnetic Code (NEC) - Method of Moments, Part I: Program Description - Theory*, Lawrence Livermore Laboratory, 1981.

[47] B. Niceno, Information about EasyMesh v1.4 available at http://www-dinma.univ.trieste.it/nirftc/research/easymesh/ .

[48] W.C. Erickson, H. Schmitt, E. Polisensky, “Report on Mutual Coupling and Impedance Measurements on Large Blade Dipoles,” *LWA memo 53*, August 28, 2006.

[49] S. Ellingson, “Antennas for the next generation of low-frequency radio telescopes,” *IEEE Trans. Antennas Propag.*, vol. 53, pp. 2480-2489, Aug. 2005.

[50] Cane, H.V., “Spectra of the non-thermal radio radiation from the Galactic polar regions,” *Mon. Not. R. Astr. Soc.*, vol. 189, pp. 465-478, 1979.

[51] W.C. Erickson, “Tests on Large Blade Dipoles,” *LWA memo 36*, May 22, 2006.

[52] D. M. Pozar, *Microwave Engineering.* Reading, MA: Addison-Wesley, 1990.

[53] G. Smith and J. Nordgard, “Measurement of the electrical constitutive parameters of materials using antennas,” *IEEE Trans. Antennas Propag.*, vol. 33, pp. 783-792, July 1985.

[54] R. Bradley, C.R. Parashare, “Evaluation of the NRL LWA active balun prototype,” *LWA memo 19*, Feb, 2005.

[55] A.E.E Rogers, P. Pratap and E. Kratzenberg, “Calibration of active antenna arrays using a sky brightness model,” *Radio Sci.*, vol. 39, RS2023, 2004.

[56] C.G.T Haslam, et al., “A 408 MHz all-sky continuum survey. II. The atlas of contour maps,” *Astron. Astrophys. Suppl. Ser.*, vol. 47, pp. 1-143, Jan. 1982.

[57] E. Polisensky, “LFmap: A low frequency sky map generating program,” *LWA memo 111*, Sept. 7, 2007.

[58] K. Lawson, C. Mayer, J. Osborne, M. Parkinson, “Variations in the spectral index of the galactic radio continuum emission in the northern hemisphere,” *Mon. Not. R. Astr. Soc.*, vol. 225, pp. 307-327, 1987.

[59] W. Stutzman, G. Thiele, *Antenna Theory and Design*, 2nd ed. New York: Wiley, 1997.

[60] S. Ellingson, “System parameters affecting LWA calibration,” *LWA memo 94*, July 20, 2007.

[61] E. Polisensky, “Station Configuration Studies III,” May 6, 2005.

[62] W. van Cappellen, S. Wijnholds, J. Bregman, “Sparse antenna array configurations in large aperture synthesis radio telescopes,” *in 3rd European Radar Conference*, Manchester, UK, Sept. 2006, pp. 76-79.

[63] S. Ellingson,“A design study comparing LWA station arrays consisting of thin inverted-V dipoles,” *LWA memo 75*, Jan. 28, 2007.

[64] V. Agrawal, Y.T. Lo, “Mutual coupling in phased arrays of randomly spaced antennas,” *IEEE Trans. Antennas Propag.*, Vol. 20, pp. 288-295, May 1972.

[65] R.C. Hansen, *Phased Array Antennas.* New York: Wiley, 1998.

[66] J. Daniel, “Mutual coupling between antennas for emission or reception - application to passive and active dipoles,” *IEEE Trans. Antennas Propag.*, Vol. 22, pp. 347-349, Mar. 1974.

[67] H. Hui, “A new definition of mutual impedance for application in dipole receiving antenna arrays,” *IEEE Antennas and Wireless Propag. Letters*, Vol. 3, No. 1, pp. 364-367, 2004.

[68] N. Paravastu, B. Hicks, P. Ray, W. Erickson, “A candidate active antenna design for a low frequency radio telescope array,” *in IEEE AP/S Int. Symp. Dig.*, Honolulu, HI, June 2007, pp. 4493-4496.

[69] A. Kerkhoff, “Comparison of dipole antenna designs for the LWA,” *LWA memo 102*, Aug. 25, 2007.

[70] H. Ishibuchi and T. Murata, “Multi-objective genetic local search algorithm,” *in IEEE Intl. Conf. Evolut. Computat. Dig.*, vol. 1, Nagoya, Japan, May 1996, pp. 119-124.

[71] M.J. Salter and M.J. Alexander, “EMC antenna calibration and the design of an open-field site,” *Measurement Science and Technology*, vol. 2, pp. 510-519, June 1991.

[72] P. A. Rizzi, *Microwave Engineering, Passive Circuits*. Englewood Cliffs, NJ: Prentice Hall, 1988.

[73] Anon., *Agilent AN 154, S Parameter Design*, Agilent Technologies application note, 2006.

Vita

Aaron Jon Kerkhoff was born in Omaha, NE on August 9, 1976. He graduated from the University of Missouri at Columbia in 1998 with Bachelor of Science degrees in Electrical Engineering and Computer Engineering. After graduation, he worked as an electrical engineer at Electronic Design and Manufacturing in Omaha, NE. He enrolled in the Graduate School at the University of Texas at Austin in 1999. While completing his graduate studies, he worked as a graduate research assistant at the Applied Research Laboratories, University of Texas at Austin. He received the Master of Science degree in Electrical Engineering in 2001. From 2001 to the present, he has continued work at the Applied Research Laboratories as a research engineer. In 2003, he re-enrolled at the University of Texas at Austin to pursue the Ph.D. degree in Electrical Engineering.

Permanent Address: 11900 Stonehollow Dr. #6302
Austin, TX 78758

This dissertation was typeset with LaTeX 2_ε[1] by the author.

---

[1] LaTeX 2_ε is an extension of LaTeX. LaTeX is a collection of macros for TeX. TeX is a trademark of the American Mathematical Society. The macros used in formatting this dissertation were written by Dinesh Das, Department of Computer Sciences, The University of Texas at Austin, and extended by Bert Kay, James A. Bednar, and Ayman El-Khashab.